SPIN-BASED THREE DIMENSIONAL MEMORY

by

Yemliha Bilal Kalyoncu

B.S., Physics, Boğaziçi University, 2011

Submitted to the Institute for Graduate Studies in
Science and Engineering in partial fulfillment of
the requirements for the degree of
Master of Science

Graduate Program in Physics

Boğaziçi University

2014

SPIN-BASED THREE DIMENSIONAL MEMORY

APPROVED BY:

Assoc.Prof.Özhan Özatay .....
(Thesis Supervisor)

Prof.Gülen Aktaş .....

Assist.Prof.Hamdi Torun .....

DATE OF APPROVAL: 04.04.2014

ACKNOWLEDGEMENTS

First and foremost, I would like to thank Özhan Özatay for leading me from nothing to a successful master thesis in experimental physics. Under his advisory I have managed such things that I could not even imagine that I would ever do. I feel lucky to have him guiding me, pushing my limits and disclosing every bit of potential in me. I am proud to have spent two years in his laboratory where I have taken a very important step in my academic career. I would also thank to former and current members of BUSPIN since it was a pleasure for me to work, to be friends and to share with them.

I am grateful to study in Boğaziçi University and learn physics from Gülen Aktaş, Teoman Turgut, Muhittin Mungan, Tonguç Rador, İbrahim Semiz, Enis Oğuz, Naci İnci and Alpar Sevgen. For every piece of knowledge I was taught, thank you for thousand times.

I would like to thank Hamdi Torun for being in my thesis defense jury, Okan Barut and Burcu Selen Çağlayan for their contribution in XPS analyses and Jordan Katine and Thomas Hauet from Hitachi for their collaboration in fabrication of the magnetic samples. I would also like to thank Murat Akman from Technology Transfer Office and Michael Boyman for the financial support they supply for the patent applications. I want to thank TUBITAK for its support under contract number 112T205, Boğaziçi University Research Fund Grant under contract number 13B03P6 and Sabancı University for allowing us use their cleanroom facilities in Nanotechnology Research and Application Center.

We were four students, me, Gizem Şengör, Mert Terzi and Cem Eröncel who sit around a brown table, surrounded by books in the quietness of library. Thanks to you for being together, learning together and sharing together.

I want to express my gratitude to my family for staying by my side and supporting

me with their love, trust and prayers. Nothing would be possible without them. I am proud to be their son and brother.

I am so lucky to have great friends, Allen Ohan Dülgar, Enver Yeşilşiraz, Sinan Şanlıer, Banuçiçek Gürcüoğlu, Aykut Ekizoğlu, Utku Barış, Hakan Tarhan and Mehmet Abi. Thank you all for spending your time with me for enjoying our youth. Those nights would never be better if any of you were missing. Among all, there is one, İrem Sezer for she was next to me, holding my hand, sharing everything in every moment during the best two years of my life.

ABSTRACT

SPIN-BASED THREE DIMENSIONAL MEMORY

Magnetic memory is the major information storage method for the last sixty years. Since its invention, this technology has undergone very rapid and vast improvements while being challenged by the requirement for higher data storage capacities, for lowering the cost of production and for less power consumption. To supply those demands, the industry constantly tries to develop new techniques. The ultimate goal of the information storage industry is to invent 3D memory systems such that the data are recorded in a three dimensional volume instead of a two dimensional thin film. In this work, two different 3D magnetic memory systems are introduced and experimented. Both of these devices utilize novel concepts of spintronics. First system makes use of a spin-laser and is based on optical magnetization reversal via circularly polarized light. The second system is a multilayer structure where domain walls are moved along ferromagnetic nanowires by the application of spin-polarized current and vertical data shift is achieved through heat assistance. In the first part of this thesis, the structure and the working principles of the former system, will be introduced and explained as an idea whereas the second part concerns with experiments for realizing the latter system. To fabricate the magnetic multilayer structure, sputter deposition and photolithography are employed. Experiments are carried out for electrical, thermal and magnetic characterization of fabricated thin films. EDS and XPS are done for stoichiometric analysis of samples. Surface properties are examined via stylus profiling and AFM. Finally, the distribution of magnetic domains is visualized with MFM. The experimental scope of this study is to establish the preliminary conditions for realizing a 3D magnetic memory structure and demonstrate how this spin-based system operates for the goal of boosting data storage capacity of future information storage devices.

ÖZET

SPIN TEMELLİ ÜÇ BOYUTLU HAFIZA

Manyetik hafızalar son altmış yıldır en yaygın kullanılan bilgi depolama yöntemidir. Bu teknoloji icat edildiğinden beri çok büyük ve hızlı gelişmeler yaşamış olmasına rağmen sürekli daha yüksek hafıza kapasitesi, daha ucuz üretim ve daha az güç tüketimi gibi sorunlara çözüm bulmak zorunda kalmıştır. Endüstri ise bu talepleri karşılayabil mek için sürekli yeni teknikler geliştirmeye çalışmaktadır. Bilgi depolama endüstrisinin nihai hedefi, ise uzun süreden beri kullanılmakta olan 2 boyutlu hafızaları geride bırakarak, verilerin iki boyutlu ince filmler yerine üç boyutlu hacimlere kaydedilmesini sağlayan üç boyutlu manyetik hafıza sistemlerini geliştirmektir. Bu çalışmada, iki farklı üç boyutlu manyetik hafıza sistemi sunulacak ve bu sistemlerin deneyleri yapılacaktır. Iki cihaz da spintronikteki yeni geliştirilmiş konseptleri kullanmaktadır. Sistemlerden bir tanesi spin-lazerin kullanılması ile dairesel polarizasyonlu ışık sayesinde manyetizasyon değişimi temeli üzerine dayanmaktadır. Çok katmanlı bir yapı olan ikinci sistemde ise, spin-polarizasyonlu akım uygulanmasıyla domen duvarlarının ferromanyetik nano boyutlu tellerde hareket ettirilmesi ve ısı yardımıyla dikey doğrultuda verilerin taşınması sağlanır. Bu tezin ilk bölümünde ilk sistemin yapısı ve çalışma prensipleri fikir olarak tanıtılacak ve açıklanacaktır. Ikinci bölümde ise diğer manyetik hafıza sisteminin gerçekleştirilme için yapılan deneyleri kapsamaktadır. Çok katmanlı yapıların üretimi sputter kaplama yöntemi ve fotolitografi ile yapılmıştır. Üretilen ince filmlerin elektriksel, ısısal ve manyetik karakterizasyonu için çeşitli yöntemler kullanılmış, örneklerin kimyasal karakterizasyonu EDS ve XPS ile yapılmıştır. İnce filmlerin yüzey özellikleri profilometre ve atomik kuvvet mikroskobu ile belirlenirken manyetik domenlerin dağılımları manyetik kuvvet mikroskopu ile görüntülenmiştir. Bu çalışmanın deneysel çerçevesini ve amacını geleceğin bilgi depolama aletlerinin hafıza kapasitelerinin arttırılması için öne sürülen spin-temelli üç boyutlu hafızaların gerçekleştirilmesi için yapılan deneyler oluşturmaktadır.

TABLE OF CONTENTS

ACKNOWLEDGEMENTS iii
ABSTRACT v
ÖZET vi
LIST OF FIGURES x
LIST OF SYMBOLS xvi
LIST OF ACRONYMS/ABBREVIATIONS xvii
1. INTRODUCTION 1
1.1. Current and Prospective Magnetic Memory Technology 3
1.2. Three Dimensional Magnetic Memory 7
2. 3D OPTO-MAGNETIC MEMORY DEVICE 11
2.1. Magnetic Recording via Circularly Polarized Light 11
2.2. Vertical Cavity Surface Emitting Lasers 13
2.3. Spin-torque Induced Domain Wall Motion 16
2.4. 3D Opto-magnetic Memory Device Structure 18
2.5. Recording and Reading Process 19
2.6. The Second Structure with Bidirectional Vertical Data Transfer 21
2.7. Conclusions 23
3. THIN FILM APPLICATIONS 24
3.1. Magnetron Sputtering 24
3.2. Calibration Procedure 26
3.2.1. Photolithography 26
3.2.2. Photomask 28
3.2.3. Deposition and Lift-Off 28
3.2.4. Surface Profilometry 31
3.3. Thin Film Experiments 32
3.3.1. Aluminium Deposition and Calibration 33
3.3.2. Copper Deposition and Calibration 34
3.3.3. Silicon Nitride Deposition and Calibration 36
3.4. CoNi/Pd Thin Film Deposition 38

3.4.1. Photomask for bow-tie shaped patterns 38
3.4.2. CoNi/Pd Deposition 40
3.5. Electrical, Thermal and Magnetic Characterization of Samples 41
3.5.1. Vibrating Sample Magnetometry Measurements 42
3.5.2. Four Point Probe Electrical Resistivity Measurements 45
3.5.3. Thermal Resistivity Measurements 48
4. STOICHIOMETRY OF FABRICATED THIN FILMS 49
4.1. Energy Dispersive X-Ray Spectroscopy 49
4.2. X-Ray Photoelectron Spectroscopy 53
4.3. EDS Experiments 56
4.4. XPS Experiments 56
5. ATOMIC AND MAGNETIC FORCE MICROSCOPY 62
5.1. Atomic Force Microscopy 62
5.2. Magnetic Force Microscopy 66
5.3. AFM Artifacts 67
5.3.1. Probe Artifacts 67
5.3.2. Scanner Artifacts 68
5.3.3. Vibrations 69
5.4. Experiments 70
5.4.1. CoNi/Pd AFM/MFM Measurements 70
5.4.2. Si_3N_4 AFM Measurements 73
6. CONCLUSIONS AND FUTURE WORK 76
APPENDIX A: SPUTTER SYSTEM 81
A.1. Sputter system 81
A.2. Operation Manual 81
A.2.1. Step 1 turning the system on 82
A.2.2. Step 2 Sputtering Procedure 83
A.2.2.1. DC Sputtering 83
A.2.2.2. RF Sputtering 84
A.2.3. Step 3 Turning the system off 85
A.2.3.1. Venting the system 85
A.2.3.2. Opening the chamber 86

A.2.3.3. Cleaning Procedure 86
A.2.3.4. Target Change 87
APPENDIX B: PHOTOLITHOGRAPHY 88
APPENDIX C: SURFACE PROFILER 90
APPENDIX D: ATOMIC FORCE MICROSCOPY 92
APPENDIX E: ION MILLING ETCH RATE CALIBRATION 95
REFERENCES 97

LIST OF FIGURES

Figure 1.1. Trilemma of magnetic recording. 3

Figure 1.2. The increase in areal density and the decrease in cost of devices over the years. 4

Figure 1.3. Heat assisted magnetic recording. 6

Figure 1.4. Coercivity versus temperature. 6

Figure 1.5. The roadmap of information storage industry. 7

Figure 1.6. IBM's race track memory. (a)Vertical racetrack. (b)Horizontal racetrack. (c)Reading. (d)Writing. (e)Storage array. 8

Figure 1.7. Perspective (left) and top (right) view of three dimensional magnetic multilayer stack. 9

Figure 2.1. Schematic illustration of right-handed (A) and left-handed (B) circularly polarized light. Electric field vector traces a helix(shown red). 12

Figure 2.2. Magnetization reversal via circularly polarized light. 13

Figure 2.3. Illustration of induced absorption. 14

Figure 2.4. Illustration of stimulated emission. 14

Figure 2.5. Illustration of population inversion. 14

Figure 2.6. Three main parts of a basic laser. 15

Figure 2.7. Basic structure of a VCSEL. 16

Figure 2.8. Transfer of spin angular momentum from spin polarized electrons causes local spins to rotate. The overall motion results in the movement of the domain wall. 17

Figure 2.9. Side view of three dimensional opto-magnetic memory device structure. 19

Figure 2.10. Top view of three dimensional opto-magnetic memory device structure. 20

Figure 2.11. Side view of three dimensional opto-magnetic memory device structure with bidirectional vertical data transfer. 22

Figure 3.1. A basic schematic of sputtering process. 25

Figure 3.2. Description of photolithography and lift-off steps with positive and negative photoresist. 27

Figure 3.3. Schematic drawing of our mask design for calibration procedure. . 29

Figure 3.4. Optic microscopy of the photomask showing length,width and intervals of calibration gratings. 30

Figure 3.5. Schematic description of a surface profiler. 31

Figure 3.6. Comparison between the measurements with(B) and without (A) vibration isolation table. 32

Figure 3.7. Surface line profile of photoresist coated patterned wafer. 33

Figure 3.8. Optic microscopy of a photoresist coated wafer, showing the dimensions of calibration gratings. 33

Figure 3.9. Optic microscopy photos of aluminum deposited wafer. Figure A shows the dimensions of the calibration gratings and figure B shows that the edges are sufficiently clear and straight. 34

Figure 3.10. Stylus profiler line profile showing the thickness of aluminium gratings on silicon wafer. 34

Figure 3.11. Stylus profiler line profile showing the thickness of copper gratings on silicon wafer for the first sample. 35

Figure 3.12. Stylus profiler line profile showing the thickness of copper gratings on silicon wafer for the second sample. 35

Figure 3.13. Stylus profiler line profile showing the thickness of copper gratings on silicon wafer for the third sample. 36

Figure 3.14. Stylus profiler line profile showing the thickness of silicon nitride gratings on silicon wafer for the first sample. 36

Figure 3.15. Stylus profiler line profile showing the thickness of silicon nitride gratings on silicon wafer for the second sample. 37

Figure 3.16. Stylus profiler line profile showing the thickness of silicon nitride gratings on silicon wafer for the third sample. 37

Figure 3.17. Design of the mask. 38

Figure 3.18. Picture of the mask showing the dimensions of the alignment marks. 39

Figure 3.19. Picture of the mask showing the dimensions of the bow-tie shaped patterns. 40

Figure 3.20. Optic microscopy image of the mask showing a bow-tie shaped pattern. 40

Figure 3.21. Optic microscopy image of the mask showing gold contact patterns. 41

Figure 3.22. Optic microscopy image of a deposited bow-tie shaped pattern. . . 41

Figure 3.23. A basic schematic of vibrating sample magnetometer. 43

Figure 3.24. Perpendicular magnetic anisotropy hysteresis loop at room temperature. 44

Figure 3.25. In-plane magnetic anisotropy hysteresis at 70°C. 44

Figure 3.26. Saturation magnetization with respect to temperature at zero external field. 45

Figure 3.27. Saturation magnetization with respect to temperature at 1 kOe external field. 45

Figure 3.28. Coercive field with respect to temperature. 46

Figure 3.29. Four Point Probe Method. 46

Figure 3.30. Electrical resistivity of CoNi/Pd multilayer with respect to temperature. 47

Figure 4.1. Basic working principle of EDS. 50

Figure 4.2. Nomenclature for characteristic X-ray lines with Sieghban notation. 51

Figure 4.3. Representation of photoelectric effect under X-ray radiation. . . . 54

Figure 4.4. Schematic drawing of a basic XPS apparatus. 55

Figure 4.5. The result of EDX analysis on silicon nitride samples. 57

Figure 4.6. XPS survey scan on the surface(A) and at around 10nm below the surface(B)of silicon nitride sample deposited at 200W. 58

Figure 4.7. XPS survey scan on the surface(A) and at 25nm below the surface(B) of silicon nitride sample deposited at 100W. 58

Figure 4.8. XPS high resolution scan of nitrogen in untreated and annealed silicon nitride sample. 59

Figure 4.9. XPS high resolution scan of oxygen in annealed silicon nitride sample. 60

Figure 4.10. XPS high resolution scan of silicon in annealed silicon nitride sample. 60

Figure 5.1. The atomic interaction forces in close proximity of a surface. . . . 62

Figure 5.2. A basic schema representing the working principle of AFM. 63

Figure 5.3. The motion of AFM tip when operating in contact mode. 64

Figure 5.4. The motion of AFM tip when operating in tapping mode. 65

Figure 5.5. The motion of AFM tip when operating in lift mode. 67

Figure 5.6. Examples of artifacts due to the AFM probe. 68

Figure 5.7. Examples of artifacts due to the AFM scanner 69

Figure 5.8. Examples of artifacts due to the piezoelectric scanner. 69

Figure 5.9. MFM image of CoNi/Pd magnetic sample in AC demagnetized state. 71

Figure 5.10. MFM image of CoNi/Pd magnetic sample in perpendicularly saturated state. 72

Figure 5.11. MFM image of CoNi/Pd magnetic sample in thermally demagnetized state. 72

Figure 5.12. Topography images of CoNi/Pd magnetic sample. 74

Figure 5.13. Topography image of silicon nitride sample. 75

Figure A.1. Vaksis Sputter System in our lab. 81

Figure E.1. Ion milling etch rate calibration steps. 96

LIST OF SYMBOLS

b	bit
emu	Electromagnetic Unit
eV	electronVolt
k_B	Boltzman's Constant
$sccm$	standard cubic centimetres per minute
E_b	Binding Energy
E_k	Kinetic Energy
E_{x-ray}	Energy of X-ray Radiation
Hz	Hertz
K_U	Magnetic Anisotropy Energy Density
NA	Numerical Aperture
R	Resolution
T	Temperature
V	Volume
W	Watt
Z	Atomic Number
λ	Wavelength
ϕ	Work Function

LIST OF ACRONYMS/ABBREVIATIONS

4pp	Four Point Probe
2D	Two Dimensional
3D	Three Dimensional
AFM	Atomic Force Microscopy
BPM	Bit Patterned Media
CAE	Constant Analyser Energy
DBR	Distributed Bragg Reflectors
DC	Direct Current
DTM	Discrete Track Media
EDS	Energy Dispersive X-ray Spectroscopy
ESCA	Electron Spectroscopy for Chemical Analysis
GDS	Graphic Data System
GL	Gaussian Lorentzian
GMR	Giant Magnetoresistance
HAMR	Heat Assisted Magnetic Recording
HDD	Hard Disk Drive
LASER	Light Amplification by Stimulated Emission of Radiation
LMR	Longitudinal Magnetic Recording
MFM	Magnetic Force Microscopy
MTJ	Magnetic Tunnel Junction
NIST	National Institute of Standard and Technology
PMR	Perpendicular Magnetic Recording
PPMS	Physical Property Measurement System
PR	Photoresist
PSDS	Position Sensitive Photo Detector
RF	Radio Frequency
SEM	Scanning Electron Microscopy
TMR	Tunneling Magnetoresistance
UV	Ultravilolet

VSM	Vibrating Sample Magnetometry
XPS	X-ray Photoelectron Spectroscopy

1. INTRODUCTION

It is irrefutable that computers have a key role in science, technology, industry and also daily life. Most of the devices in research laboratories are operated via computers; while the technology tries to develop more powerful computers, computers boost technological advances further and not only we have personal computers at home, we have laptops in our bags and we have smartphones in our pockets. So since we are surrounded by and dependent on computers, it is a must for science and technology to improve the computer technology.

One of the main components of computers and similar technological tools is information storage device where all the information and data are processed and saved for short or long periods of time. For instance, enormous amount of data (such as petabytes or terabytes of data which are impossible to store in a single conventional storage device) is created at scientific research centres, flows through internet and most of the people have their own movie and music archives. Due to all that usages, there is a huge demand for higher storage capacities, faster processing of data, cheaper devices etc. This drives scientists and engineers to constantly develop novel methods to supply that demand in information storage industry.

Although there are solid state and optical memory solutions, magnetic devices still have a major part in information storage industry. Since the first magnetic disk drive was introduced in 50's, they are the primary solution for data storage. Even though they were improved vastly throughout the years, thanks to latest advances in physics, nanofabrication and material science, magnetism is still promising for further improvements in data storage applications.

In a conventional magnetic disk drive, namely Hard-Disk Drive(HDD), there are three main components; read and write head for reading and recording the data, a magnetic thin film coated on a glass or aluminium disk where data is stored and electronic components to run the device. In such a magnetic medium, information

is recorded in binary language as 0s and 1s corresponding to magnetic orientation of magnetic domains. Each of those nanoscale domains consists of some number of magnetic grains. In other words, a predefined number of magnetic grains constitute a bit which is either 0 or 1 depending on the overall orientation of magnetization of that specific domain (or bit). For example, if the magnetization of a domain is upwards with respect to the plane of the disk, we can say that it is a 1 bit and if the magnetization is downwards it is a 0 bit.

One of the ultimate goals of information storage industry is to increase the data storage capacity. The number of magnetic domains or bits on a magnetic thin film determines the amount of information that can be recorded. In order to increase the capacity, there must be more number of bits in a unit area on that magnetic medium. For denser magnetic thin films, the volume of magnetic domains and grains should be smaller. However, there is a limit for scaling the volume of magnetic grains. Magnetic energy per particle is defined as $K_U V$ (where K_U is magnetic anisotropy energy density and V is the volume of the bit). Decreasing V will result in low magnetic energy such that magnetic domains will be subject to thermal instabilities at room temperature. Because the magnetic energy becomes comparable to thickness of the energy barrier in between two equally-likely magnetic states so that magnetic particle can randomly move from one state to another. This in turn results in reversal of magnetization of magnetic grains and eventually the loss of data. This is called superparamagnetic effect. As an industrial standard, this $K_U V$ value should be greater than $45 k_B T$ (k_B is the Boltzman's constant and T is the temperature) for 10 year stability of the HDD. One way to evade this problem is to increase $K_U V$ value, namely using different kind of a magnetic material that has higher magnetic anisotropy energy density. Nevertheless, high K_U materials will require stronger magnetic field for magnetization reversal. The strong magnetic field requirement may not be addressable with a conventional recording head. This situation is called the writability problem. In the end, in case of increasing data storage capacity, the industry hits a road block called trilemma of magnetic recording [1] as illustrated in Figure 1.1. That's why scientists and engineers come up with different ideas and techniques in designing recording media to push forward storage capacities.

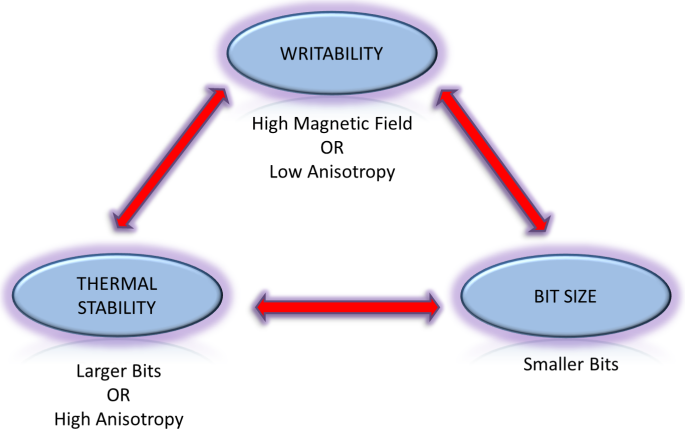


Figure 1.1. Trilemma of magnetic recording.

1.1. Current and Prospective Magnetic Memory Technology

In 1956, IBM introduced the first magnetic disk drive with a capacity of 4.4 Mb. That magnetic drive was as big as a large bookcase. Today, the magnetic storage density of a typical HDD is about 400Gb per inch square and it is as small as one can hold it on his palm. The vast increase in the storage density throughout this 60 years is due to the tremendous improvements in science and technology such as thin film growth and the possibility of more sensitive and smaller read/write sensors. In early magnetic memory systems, the most common method for recording on a medium was Longitudinal Magnetic Recording(LMR) [2]. In this method, magnetization of the magnetic grains defining the bits was oriented along the disk plane. In other words, the magnetic domains were in-plane magnetized. The way to increase the storage capacity depended on scaling down the size of the magnetic domains. Today, LMR is replaced by Perpendicular Magnetic Recording(PMR) [2]. In this technique, the magnetic domains are magnetized out-of-plane with respect to thin film plane. The change from LMR to PMR resulted in a huge increase in the areal storage density, since PMR permits smaller magnetic domains to define bits without running into the superparamagnetic limit. On the other hand, industry started to make use of magnetoresistive effects for read-write heads. The emerging read sensors are based on the Magnetic Tunnel Junction (MTJ) [3] which utilizes Tunneling Magnetoresistance (TMR) effect [4]. An MTJ is a combination of three thin stacks, a non-magnetic insulating layer sandwiched in

between two magnetic layers. This device operates in the following way, the field coming from the bit orients the magnetization of the magnetic probe layer. The magnetization of the magnetic layer which is placed at the opposite side of the MTJ is kept fixed. During the reading process an electric current flows through the device, tunneling through the insulator layer. Depending on the relative orientation of magnetizations of those two magnetic layers, the tunneling ratio differs so when the resistance is read, one high and one low resistance value is measured corresponding to anti-parallel and parallel situations, respectively. The advantage of this magnetoresistive element relies on its sensitivity that it successfully senses low amount magnetic fields coming from the magnetic medium. This in turn allows smaller magnetic domains to define bits.

Combination of advances in both magnetic media and read sensors lead the industry to storage densities of 600Gb/in^2. As illustrated in Figure 1.2 [5], the last fifty years witnessed about 8 orders of magnitude increase in areal density and almost equal amount of reduction of the costs. Moreover, the experts state that the current technology will lead to densities of 750Gb/in^2 with appropriate engineering of magnetic media and read-write heads. However, the trilemma of magnetic recording is still an obstacle to be overcome for further increase in areal density.

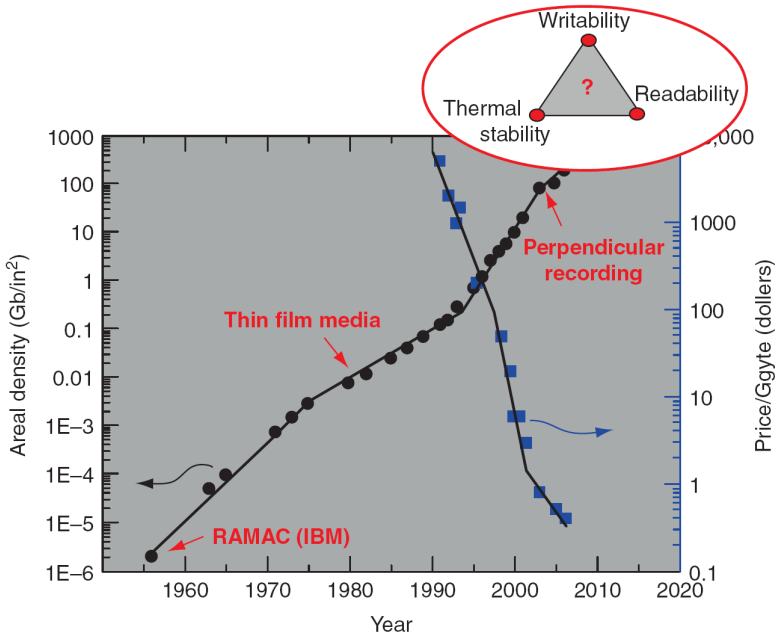


Figure 1.2. The increase in areal density and the decrease in cost of devices over the years.

Yet, the requirement for much higher storage densities beyond terabits per inch square stands still and pushes scientists for further developments. The first step in the nearest future seems like patterning magnetic domains on the magnetic medium instead of continuous granular structure as in PMR. There are two methods in patterned media. First one is called Discrete Track Media (DTM) [6] and it is based on defining data tracks separated from each other on the magnetic medium. In conventional HDD technology, a data track cannot be thinner than the size of the read/write head. Otherwise, the field from the adjacent tracks would interfere the reading process of a specific track or the magnetic domains would be affected by the write field coming from the write head while registering information on a specific track. Alternatively, one can lithographically introduce data tracks with a separation on the recording medium such that adjacent tracks are not affected during reading and writing processes. Track widths less than 60nm, which is required for Tb/in^2 areal densities, are possible with DTM but not with conventional PMR. Second method is called Bit Patterned Media (BPM) [7, 8]. This method proposes forming magnetic islands (or dots) on the recording medium corresponding to a single bit. For instance, to reach $1Tb/in^2$ areal density, in conventional PMR one bit needs 30 grains with a diameter of 4nm. On the other hand, in BPM a magnetic dot with a diameter of 12.5nm is sufficient to record same amount of information. Besides, thermal stability of 12.5nm magnetic dots is higher than the 30 grain bits of PMR. Thus, bit patterned media has a strong advantage compared to perpendicular magnetic recording in case of thermal stability and areal density. Research on DTM and BPM have been made and is still going on for realizing such a structure as near future's information storage devices. It is expected that areal densities up to $10Tb/in^2$ is possible as a result of intense research on patterned media [5].

To go beyond $10Tb/in^2$, energy assisted magnetic recording is proposed and expected to reach $20Tb/in^2$ areal density. As explained above, reducing grain sizes results in loss of data due to superparamagnetic effect. To overcome this problem, magnetic materials with higher magneto-crystalline anisotropy (K_U) must be used. This in turn leads to problem of writability such that one needs higher magnetic fields to be applied for magnetization reversal. At this point, an external agent can help to allow applica-

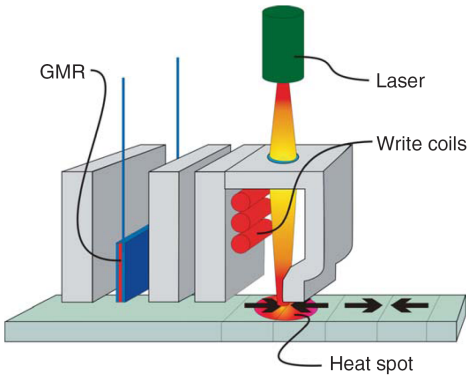


Figure 1.3. Heat assisted magnetic recording.

tion of less magnetic field. Heat Assisted Magnetic Recording (HAMR) suggests that [9] before applying magnetic field for magnetization reversal, a laser can be focused on the recording medium, so that coercivity of the medium will be reduced momentarily due to local heating. This way, magnetization reversal can be realized with application of less magnetic field as depicted in Figure 1.3 and Figure 1.4. Thus, HAMR permits utilizing high K_U materials, evading trilemma of magnetic recording and allowing much higher areal densities.

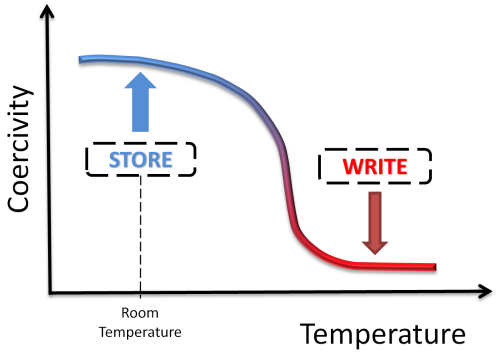


Figure 1.4. Coercivity versus temperature.

Figure 1.5 [1] summarizes the density capabilities of previously mentioned technologies. Whichever technique is used, there is always a limit in the areal density increase due to the trilemma of magnetic recording. Apart from those current technologies, there is still one ingenious alternative among all that which pushes data storage density further. It is to go beyond two dimensions(2D) and invent three dimensional(3D) devices such that information is recorded not on an area but in a volume. Utilizing the vertical direction has the potential to be the ultimate information storage device, capable of having storage densities many orders of magnitude greater than

today's devices.

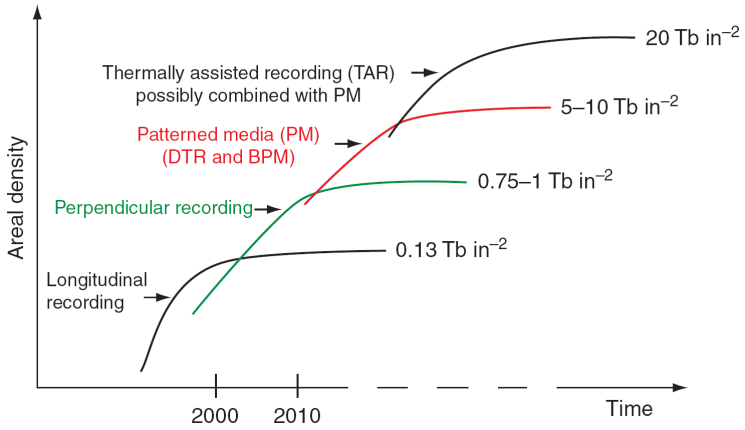


Figure 1.5. The roadmap of information storage industry.

1.2. Three Dimensional Magnetic Memory

The first example of a 3D magnetic memory is proposed by IBM and called Race Track Memory [10]. In this device, illustrated in Figure 1.6, the information is recorded not in magnetic thin films but in ferromagnetic nanowires, and again a bit is defined not as a magnetic domain formed by magnetic grains but rather the presence or absence of magnetic domain walls. These nanowires are u-shaped and when an array of them is constructed, a three dimensional structure is formed.

This system operates in the following way. At the bottom of these u-shaped nanowires there are write and read lines. The Oersted field from a current carrying wire is utilized for recording data and reading is done by a Magnetic Tunnel Junction element by sensing the stray field coming from the nanowire and these operations are only done at the bottom of the wire. For that reason, the bits at the upper parts of the nanowire must be moved along the wire and brought to the bottom. This procedure is done by exploiting spin torque induced domain wall motion [11]. It is that when a spin polarized current is applied along this ferromagnetic nanowire, domain walls in between the bits move along the direction of electron flow. This movement is due to spin-torque transfer [12]. So by applying spin polarized current, the whole bit pattern is shifted along the wire and so the interested bit can be brought to bottom of the u-shaped wire. Whereas this three dimensional structure has the capacity to

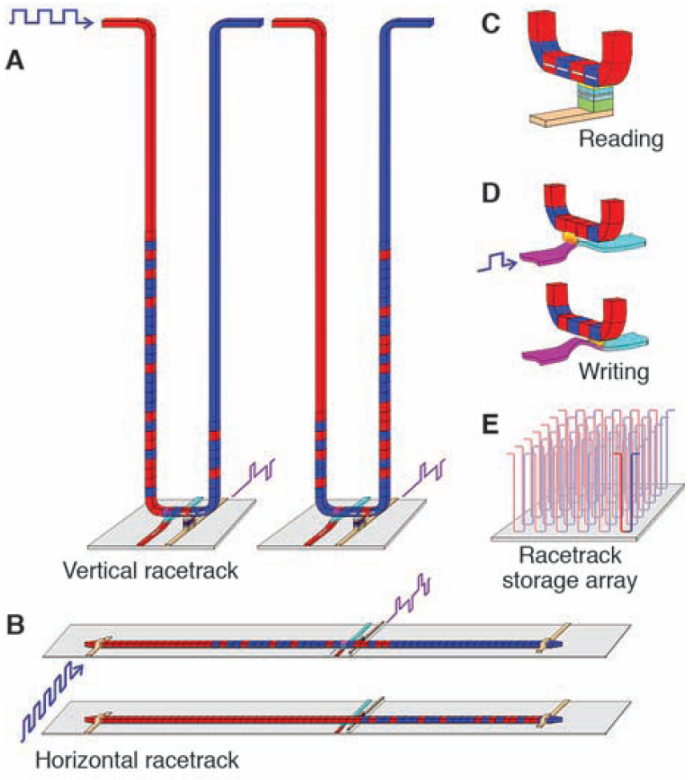


Figure 1.6. IBM's race track memory. (a)Vertical racetrack. (b)Horizontal racetrack. (c)Reading. (d)Writing. (e)Storage array.

increase information density by two orders of magnitude, it is still a great challenge for nanofabrication techniques to realize such a 3D structure.

Another example of a three dimensional system, magnetic page memory is suggested by Ozatay and Terris in [13]. This device makes use of both ideas of three dimensional magnetic memory structure and energy assisted magnetic recording. As illustrated in Figure 1.7, the three dimensional structure is a multilayer stack where each layer consists of ferromagnetic nanowires with hexagonal constrictions oriented parallel. Alternating layers are oriented such that ferromagnetic nanowires of a layer are perpendicular to adjacent layers' nanowires. This cross-wire architecture is built in order to reduce errors during vertical shift. Operation of this structure is as follows. An external write head applies Oersted field to register information on the top layer. When the top layer is full, an electric pulse is applied along the wires of bottom layer and the one underneath, reducing the coercivity of the material via Joule Heating. As a result, the stray field coming from the top layer will be enough for magnetization

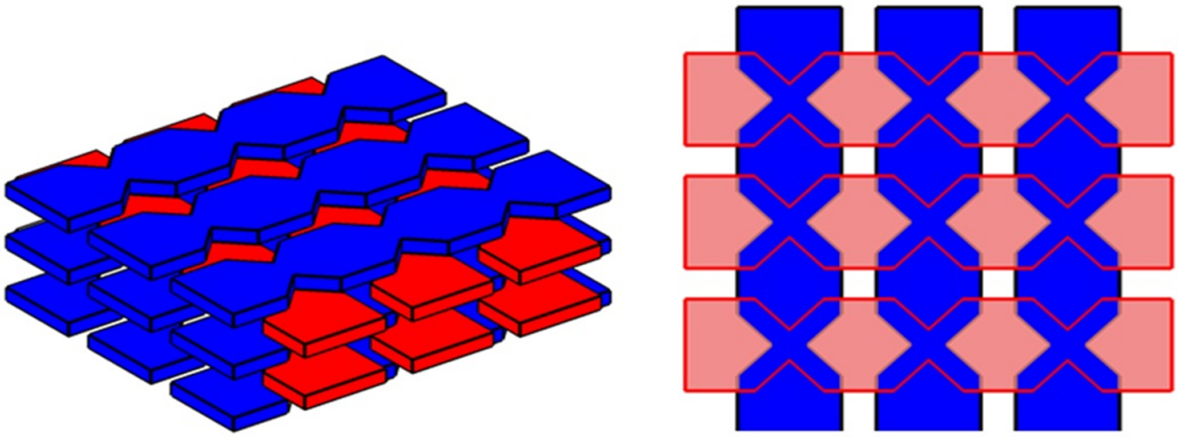


Figure 1.7. Perspective (left) and top (right) view of three dimensional magnetic multilayer stack.

reversal in the bottom layer. Thus, a vertical shift will occur from the top layer to bottom layer at once and the top layer will have space for recording new information. Moreover, application of spin polarized current along ferromagnetic nanowires allows horizontal movement of bits via spin-torque induced domain wall motion [12]. Since there is no physical limit for the number of magnetic layers constituting the multilayer stack, it is rather an engineering problem to find the most efficient solution when deciding the number of layers and the dimensions of the device.

The aim of this thesis is hypothetical and experimental studies regarding such three dimensional magnetic memory structures. Throughout the thesis, two different 3D magnetic memory systems are introduced. In Chapter 2, a three dimensional opto-magnetic memory device will be proposed. This device constitutes magnetic multilayers and vertical cavity surface emitting lasers (VCSELs) utilized for vertical shift register of bits from one magnetic layer to another. This system will be presented only as a preliminary idea which possesses advantages of third dimension and low power consumption due to its structure and operation. Fabrication and demonstration of this system have not been studied yet and are beyond the scope of this thesis. Following chapters will explain in detail the experiments conducted for realizing magnetic page memory system. Chapter 3 is about the fabrication of the materials constituting the magnetic multilayer structure and thin film applications for deposition of magnetic and

insulating thin film layers via magnetron sputtering are given. In Chapter 4, stoichiometry of fabricated thin films will be given for chemical characterization of fabricated thin films and discussed whether their chemical properties satisfy the necessary magnetic, electrical and thermal conditions for the device to operate accurately. Then, in order to study the surface and magnetic properties of the mentioned thin films, atomic and magnetic force microscopy are the subject matter of Chapter 5. Finally, concluding remarks on both these systems are expressed in Chapter 6.

2. 3D OPTO-MAGNETIC MEMORY DEVICE

Apart from the experiments and the subjects in this thesis, here another three dimensional magnetic memory device is proposed. This device is published as a patent from Turkish Patent Institute and titled "A Three Dimensional Opto-Magnetic Data Storage System and Method" [14, 15]. The system with bidirectional vertical data transfer which is explained in Section 2.6 is also in the application process for an international patent [16]. The device uses optical methods to register information on a magnetic medium. Since it is a three dimensional structure it also possesses advantages of third dimension that which explained in the first chapter.

2.1. Magnetic Recording via Circularly Polarized Light

The conventional way to record a bit is to orient the magnetization of the domain by applying an external magnetic field. Alternatively it is experimentally demonstrated that circularly polarized light can be utilized to change the magnetic orientation of a magnetic medium via inverse Faraday effect [17]. In the work of Stanciu [18], ultrashort circularly polarized light pulses are acted upon a magnetic thin film for magnetization reversal. Inverse Faraday Effect is a magneto-optical effect and based on Coherent Raman-like Scattering. It is commonly accepted that spin-orbit coupling is necessary for magneto-optical effects. In the process of Raman Scattering a laser pulse stimulates an optical transition from the ground state to a virtual excited state when the energy of the incident photon is smaller than the energy gap between ground and excited electronic state. Due to some interaction, such as spin-orbit coupling, that virtual state is split. When the electron turns back to ground state, its magnetic state is changed. The materials with the high value of Faraday rotation such as rare-earth ferrimagnetic metals [19] are expected to be most efficient for optical control of magnetization. Whether the spin-flip will occur or not is defined by the direction of the rotation of stimulating circularly polarized light. Right and left circularly polarized waves act as an effective magnetic field of opposite direction. This phenomenon can be utilized as a recording mechanism in the following way. If the data is to be stored on a magnetic thin film

in perpendicular magnetic recording scheme, then the magnetizations of magnetic domains (bits) are perpendicular to the film plane, either up or down. For magnetization reversal from an up state to down state, an external magnetic field should be applied to change the magnetizations of bits. However, a right-handed circularly polarized light pulse does the same job as the external magnetic field does. It flips the spins of electrons constituting that particular magnetic domain. When the direction of the electric field vector of that electromagnetic wave rotates counter clockwise, it is said that the wave is right-circularly polarized and acts as a magnetic field, direction of which is parallel to the propagation vector of that electromagnetic wave. On the other hand, when the direction of the electric field vector rotates clockwise, it is said that the wave is left-circularly polarized and acts as a magnetic field oriented in the opposite direction of propagation vector as illustrated in Figure 2.1.

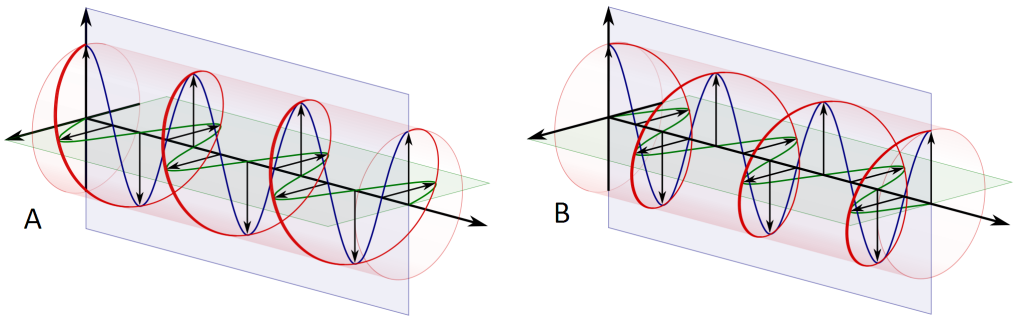


Figure 2.1. Schematic illustration of right-handed (A) and left-handed (B) circularly polarized light. Electric field vector traces a helix(shown red).

In Figure 2.2, demonstration of magnetization reversal via circularly polarized light pulses is shown [18]. There is a ferrimagnetic thin film of $Gd_{22}Fe_{74.6}Co_{3.4}$ which is known to have strong magneto-optical effects and strong perpendicular magnetic anisotropy. The thin film has magnetic domains, initial magnetic orientations of which are opposite to each other, shown as dark coloured area corresponding to down magnetic domain(M^-) and light colored area corresponding to up magnetic domain(M^+) in Figure 2.2a. Linear and right and left circularly polarized light beams are swept across the surface at a speed of 30 μm/s and the final magnetic state is seen on Figure 2.2b. The wavelength of the exposed light is 800nm. As seen in the figure, right handed circularly polarized light ($\sigma+$) orients the magnetic moments up and left handed circularly polarized light ($\sigma-$) orients the magnetic moments down. Besides, linearly polarized

light (L) leaves the medium in a demagnetized state due to heating.

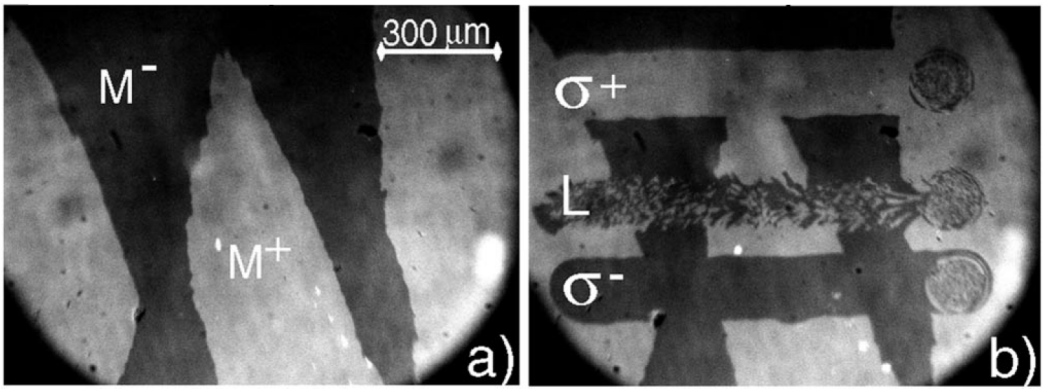


Figure 2.2. Magnetization reversal via circularly polarized light.

2.2. Vertical Cavity Surface Emitting Lasers

In the process of magnetization reversal via light action, the light must be very intense, collimated, monochromatic and coherent. Namely, it must be a LASER which is the acronym for Light Amplification of Stimulated Emission of Radiation [20]. Random absorption and emission of photons in a material result in incoherent light. On the other hand, laser light is uniform in frequency, amplitude, continuity and phase. This kind of light output can be obtained via stimulated emission of photons from a material. There are three basic photon matter interaction mechanisms in the case of laser action. First one is called induced absorption. When photons of suitable energy are supplied to the atoms in the ground state, those atoms absorb the supplied energy and get excited and move to a higher energy state as illustrated in Figure 2.3. The energy of the photon required for this process must be equal to the energy difference between the ground state and the excited state. The second process is called spontaneous emission. An excited atom can stay in higher energy state for no more than 10ns. After that time the atom returns back to the ground state by giving off the previously absorbed energy in the form of photons. If a photon of suitable energy is sent to the excited atom, the atom falls back to the ground state by emitting a photon which is in phase with the triggering photon. This process is called stimulated emission and depicted in Figure 2.4 For the laser action to happen, induced absorption and stimulated emission processes must be repeated many times with large number of photons. Thus, the number of atoms in higher energy state must be greater than that

in the ground state. The process of making the higher energy state more populated is known as population inversion and the method to achieve this is called pumping. In this action, atoms are raised to an excited state by injecting photon of frequency different than the stimulating frequency into the system. In a basic laser system, there are three main parts. They are the active medium where the laser action takes place, pumping mechanism to achieve population inversion and the mirrors for the light to oscillate in between to provide output of continuous coherent radiation with increased intensity. A laser with its fundamental parts is depicted in Figure 2.6.



Figure 2.3. Illustration of induced absorption.



Figure 2.4. Illustration of stimulated emission.

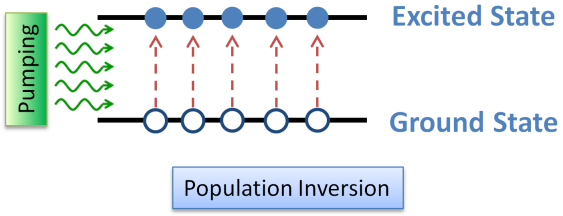


Figure 2.5. Illustration of population inversion.

There are different kinds of lasers depending on state of the laser medium (solid, liquid, gas) , type of pumping (flash light, chemical action, electrical discharge), type of output (pulsed, continuous) and spectral region of output (UV, infra-red, visible etc.) and some other types of lasers such as solid-state lasers etc. There are also semiconductor lasers which are pumped electrically and the radiation of light results due to recombination of electrons and holes in the material.

Circularly polarized light can be generated with spin-polarized vertical cavity surface emitting lasers [21]. A Vertical Cavity Surface Emitting Laser (VCSEL) is a recent

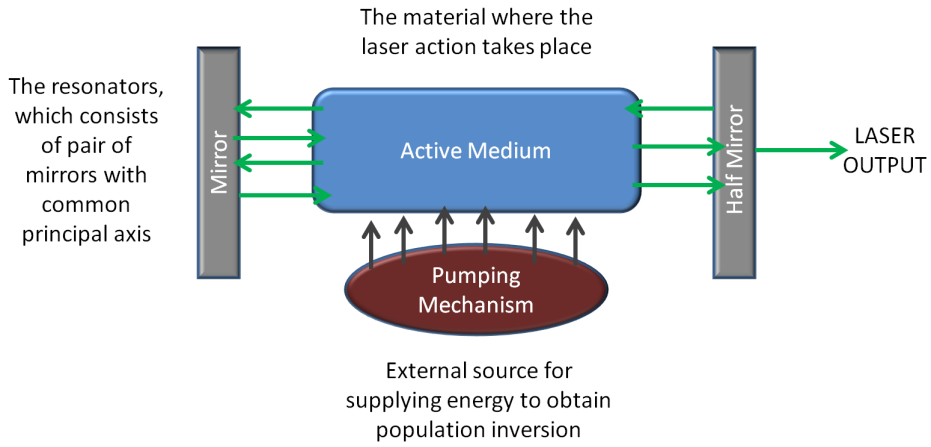


Figure 2.6. Three main parts of a basic laser.

type of semiconductor laser. They are made up of semiconductor layers grown on top of each other via molecular beam epitaxy or vapor deposition techniques. The main advantage of VCSELs is the scalability of such devices and the ability to be further processed in order to be implemented in any other device where needed. Even tough there are many different VCSEL structures, fundamental structure of a VCSEL is always the same and it is illustrated in Figure 2.7. There is an active layer sandwiched between multiple layers of highly reflective mirrors. The generation of light occurs in the active layer due to annihilation of electron-hole pairs. The generated light then oscillates in between the mirrors which are called Distributed Bragg Reflectors(DBR) [22]. These semiconductor reflector layers have a thickness of the quarter of the wavelength of the light generated in the active region and they have alternating high and low refractive index. This multilayer structure is always deposited on an appropriate substrate and the total structure is again sandwiched with electrical contacts which supply electrical current for generation of light. Depending on the choice of usage, the emission of light may be realized through the top or bottom of the device by leaving a suitable hole at the most outer layer. As it is understood, a regular VCSEL has dimensions of microns and hundreds of them can be fabricated on a silicon wafer at once.

For our purposes, a particular VCSEL structure [23] is employed. In this type of VCSEL the transparent substrate is wafer bonded to the core of the VCSEL. The importance of that specific structure comes from the fact that it allows fabrication of multiple VCSELs on top of each other with a magnetic thin film spacing. Figure 2.7

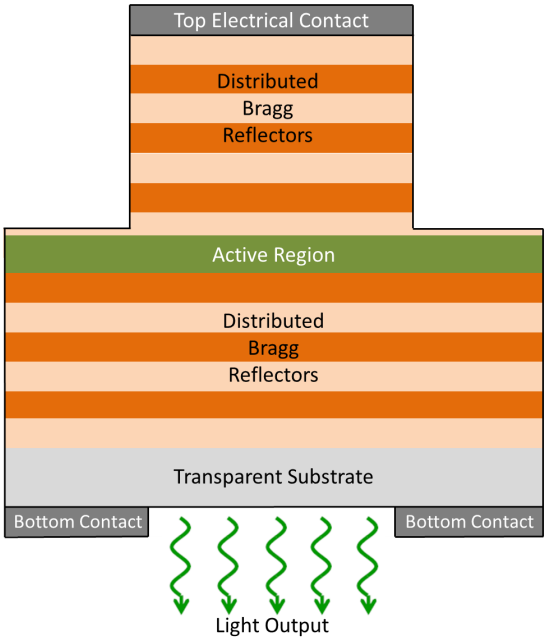


Figure 2.7. Basic structure of a VCSEL.

shows a simple drawing of the mentioned VCSEL. Regular operation of this device does not generate circularly polarized light. For this to happen, one must use a spin-VCSEL [21]. In these devices, spin polarized electrons (or holes) recombines with unpolarized holes (or electrons) in the active region and emission of right or left circularly polarized light occurs. Spin polarized carriers can be generated in semiconductors through electrical pumping of a spin polarized current. When electrical current passes from a ferromagnetic material to a non-magnetic semiconductor, the overall magnetization of the carriers (electrons or holes) are determined by majority or minority spins and the current is said to be spin polarized. This phenomenon is called electrical spin injection [24]. The asymmetry in the spins of electrons is a consequence of the difference in the density of states of the spin subbands of the ferromagnet.

2.3. Spin-torque Induced Domain Wall Motion

In an ordinary conductor, the spins of the current carrying electrons do not possess the same orientation. On the other hand, if this conductor is also a ferromagnetic material, the current becomes spin-polarized due spin-dependent diffusive scattering and carries spin angular momentum [25]. When this spin-polarized current encounters

a domain wall, it applies a torque to the moments of the local spins. As shown in Figure 2.8, that transfer of spin angular momentum causes individual local spins to rotate and so the overall motion of electrons results in movement of the domain wall. The movement of the domain wall is directed in the opposite direction of the current flow and is independent of the magnetization direction of the domain wall.

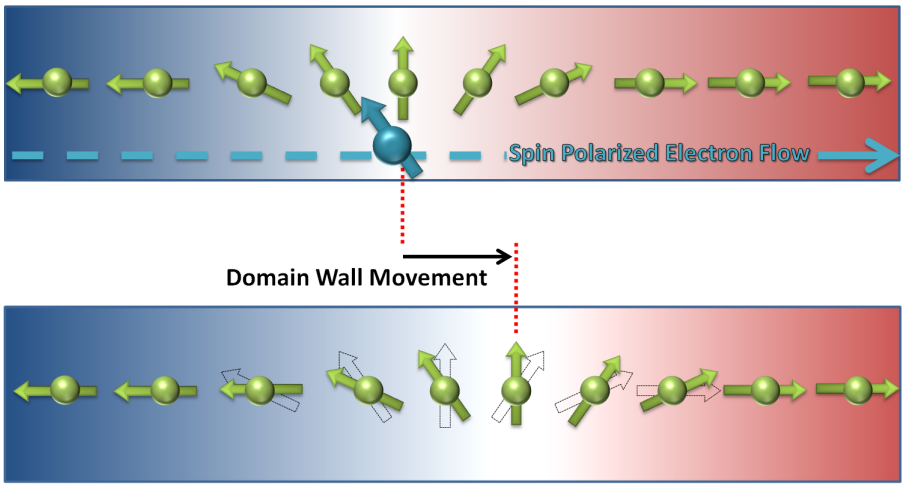


Figure 2.8. Transfer of spin angular momentum from spin polarized electrons causes local spins to rotate. The overall motion results in the movement of the domain wall.

If we want to examine this phenomenon in detail, there are three effects that the current induces sequentially while flowing through the domain wall. First one is the increase in the local temperature due to Joule Heating. Thermal activation makes propagation mechanisms more effective. Secondly, linear momentum transfer to the local spins from the current carrying electrons causes a pressure on the wall. The final effect is the dragging of the domain wall via spin-torque. The transverse spin component of the current carrying electrons apply torque on the local spins which results in the dragging of the domain wall in the direction of electron drift.

The importance of spin-torque induced domain wall motion for our purposes is that it will be utilized for horizontal movement of bits (domains). Along a ferromagnetic nanowire, sequentially recorded magnetic domains will be separated by each other with domain walls. So, the movement of every domain wall simultaneously along the nanowire will in turn result in the movement of the domains in the direction of electron flow. In this way, one can manage to shift the bits horizontally.

2.4. 3D Opto-magnetic Memory Device Structure

Figure 2.9 shows side view of the recording medium which basically consists of ferromagnetic thin film multilayers (blue) and VCSELs (orange) in between the magnetic layers. The space between two VCSEL cells is filled with a thermal insulator material(violet). On top and bottom of each VCSEL cell there are top and bottom electrical contacts(green) that are micron sized wires. A similar structure is patterned on multiple wafers and aligned on top of each other as shown in the figure and wafer bonded through the conducting transparent substrate(grey). As a result, it is a three dimensional structure consisting of alternating multiple layers of magnetic thin films,VCSELs and transparent layers. It must be noted that the figure is not drawn to scale but it is only to show the periodic structure and the components of the system clearly. In Figure 2.10, the structure of top, bottom and side electrical contacts along a layer is explicitly shown. On each layer, top and bottom electrical contacts of every VCSEL are linked to the same contact pad. This means that, when a current pulse is applied, every VCSEL on that layer operates simultaneously. As can be seen in the figure, the contact wires are straight and parallel to each other, covering the whole layer. Besides, in order to trigger domain wall motion by application of spin polarized current, the magnetic layer is connected to side electrical contacts. It must be noted here that, even tough we consider it as a magnetic layer, indeed, the magnetic material where the bits are recorded are straight nanowires along the layer with hexagonal constrictions and the wires are placed parallel to each other thus covering a two dimensional area. These hexagonal constrictions are needed to create pinning sites at well-defined points. The domains (bits) are located in between those hexagonal constrictions by pinning the domain walls at the edges of those hexagonal shapes.

There are two kinds of bits in the structure named according to their functionalities. Bit-B (Buffer bit) is defined as the bits recorded directly by circularly polarized light acting upon it and Bit-A (Active Bit) onto which the information is transferred from the adjacent bit-B by spin-torque-induced domain-wall motion. Each VCSEL cell has bit-A on top and bit-B on the bottom. Bit-A and Bit-B are shown with different colours to express the position of bits along the layer even though the magnetic layer

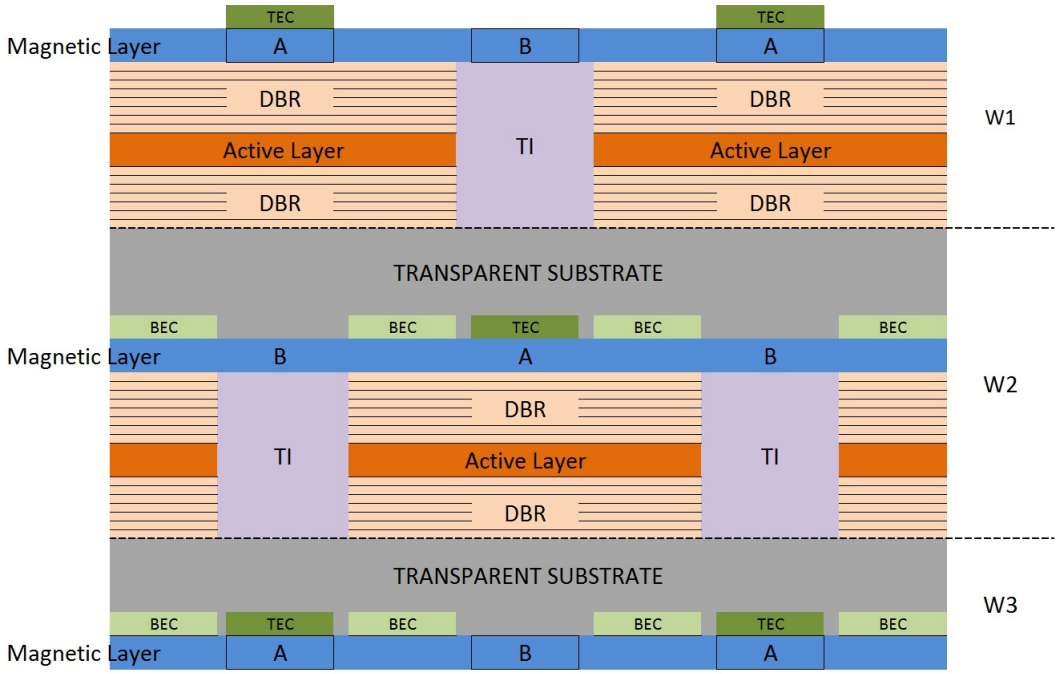


Figure 2.9. Side view of three dimensional opto-magnetic memory device structure.

is actually homogeneous and uniform.

It should be noted that, there is no limit to the number of layers. The described structure can extend to any number of magnetic layers depending on the choice of storage capacity and engineering.

2.5. Recording and Reading Process

First of all, the information is registered on the top magnetic layer by means of opto-magnetic recording. After that, the system works in a way that the recorded bits on the top magnetic layer are copied to the bottom magnetic layers. On the other hand, any recorded bit is read on the very bottom magnetic layer by means of a GMR or TMR sensor (read head in hard drives) [1, 4].

The copying of the recorded bits to the bottom layers is as follows. On the top layer any Bit-B is recorded by opto-magnetic recording. Then, a current pulse ($10^8 A/cm^2$, 1ns duration [25]; can be engineered through materials optimization) is

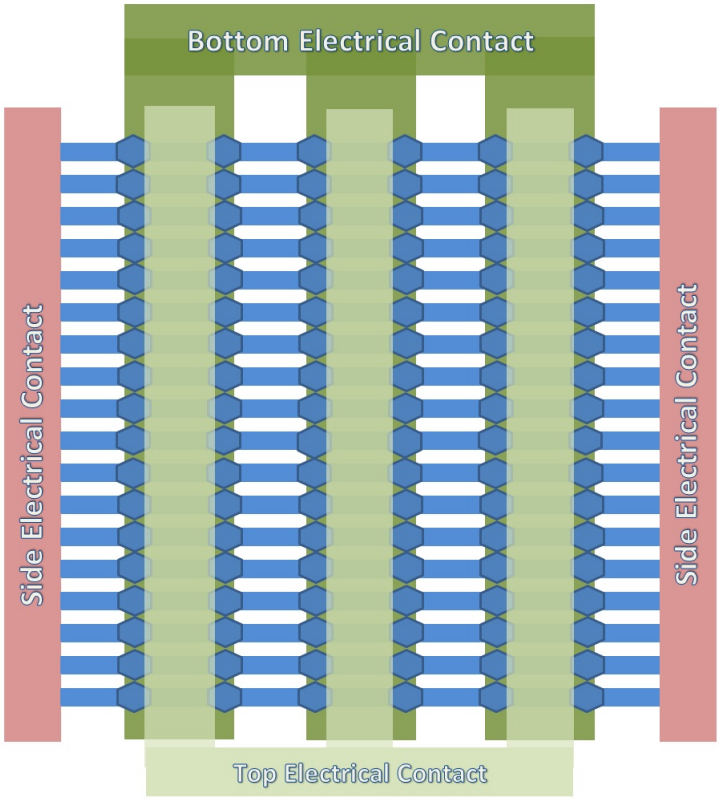


Figure 2.10. Top view of three dimensional opto-magnetic memory device structure.

applied on this magnetic field in order to transfer these recorded Bit-B's to the adjacent Bit-A's that are just under the top electrical contacts through spin-torque induced domain-wall motion. Then another current pulse (few μA's, ns duration) is applied in between top and bottom electrical contacts of each VCSEL. Since this current passes through the magnetized layer (Bit-A), it is spin-polarized. This spin-polarized current pulse activates VCSEL, resulting in the emission of right or left circularly polarized light, whose orientation is determined by the spin polarization direction. This emitted light, then acts upon the Bit-B just under the VCSEL on the second magnetic layer. As a result, we copy the bit on the top layer to the bottom layer. If these bits are to be copied to further bottom magnetic layers, the same procedure must be applied. This procedure of interlayer data transfer is executed all in parallel (parallel vertical shift).

In order to access data stored in any intermediate layer, the read procedure is as follows. To avoid loss of information during the vertical shift, some buffer is needed to store the previously recorded bits. For instance, consider that the recording system

consists of four magnetic layers and three VCSEL layers in between them and every bit-A is recorded. If a bit-A on the second layer is wanted to be read, a current pulse is applied between top and bottom electrical contacts of that VCSEL layer, this will shift the second layer's bit-A's to the third layer's bit-B's. Then the third layer is wanted to be copied to the fourth layer while keeping the information on the third layer. When a current pulse is applied on the third magnetic layer, every bit-A are transferred to adjacent bit-B and every bit-B to the adjacent bit-A. This brings the required bits on top of the VCSEL cells in between the third and the fourth layer. By again applying a current pulse on top and bottom electrical contacts of that VCSEL layer, the information is again shifted down to the fourth layer. After copying, a current pulse has to be applied on the third magnetic layer again but this time in the opposite direction in order to move back the kept bits of the third layer from bit-B's to bit-A's. Finally, a read head can read the bit from the bottom magnetic layer.

2.6. The Second Structure with Bidirectional Vertical Data Transfer

Different than the first structure which can only perform vertical data transfer in one direction, the second structure can perform vertical data transfer in both directions, up and down. To accomplish this, the multilayer stack is modified accordingly. The main difference in this structure is that there are VCSELs which are capable of emitting light from the top surface. While the operation principle and the core structure of a VCSEL is the same, it can simply be expressed as top and bottom electrical contacts replaced their places such that top electrical contact is now just under the bottom magnetic layer and bottom magnetic contacts are in between upper magnetic layer and DBRs, leaving a hole on the top surface of the VCSEL such that the light generated in the active region is emitted from the top surface and falls on the upper magnetic layer. Besides, instead of only A and B, here there three kinds of bits named as D, S and U. Again, this differentiation of bits is not due to their intrinsic features but to their functionalities. The vertical data transfer procedure is exactly the same as it is explained for the first structure, in a staircase scheme. Plus, now bits can be transferred along both vertical directions.

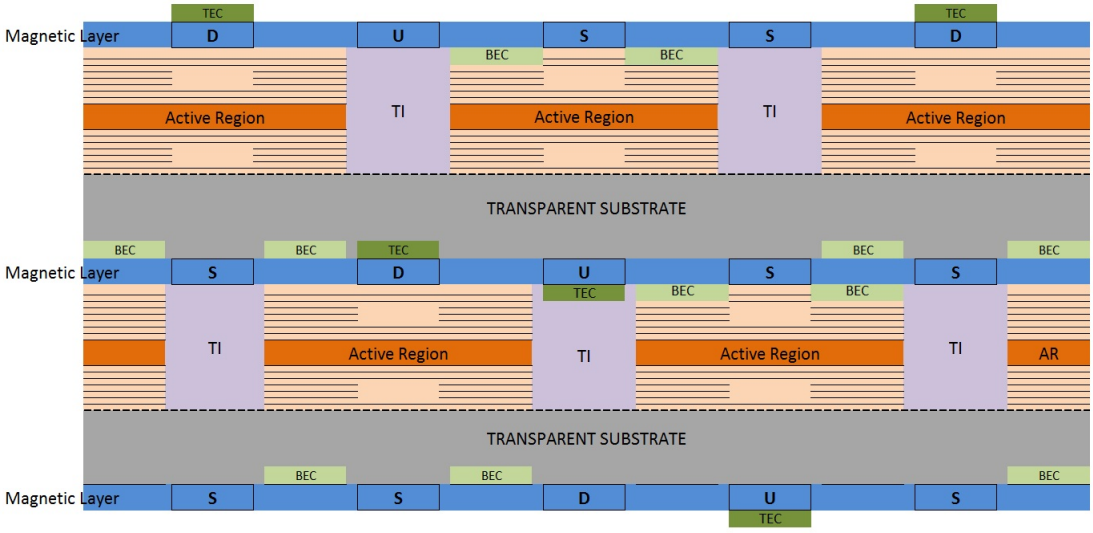


Figure 2.11. Side view of three dimensional opto-magnetic memory device structure with bidirectional vertical data transfer.

If the information stored on S-bits (S stands for Storing) of a magnetic layer is wanted to be transferred to the bottom layer, then an electric current is applied on that magnetic layer to move the interested S-bits to the position of D-bits (D stands for Down copying) via spin-torque induced domain wall motion. When the VCSEL is activated with application of current through the electrical contacts, the light generated in the active layer falls on the bottom magnetic layer, copying the information of the above layer to below. If the bits are wanted to be copied to the upper magnetic layer, then the bits are moved to U-bits (U stands for Up copying) by an electric pulse and with the activation of appropriate VCSELs, the data will be copied to upper magnetic layer. If the bits are to be transferred further, this procedure is applied again in staircase scheme.

As it is in the first structure, after each vertical data transfer operation, and electrical current which is in the opposite direction of the current applied before VCSEL activation must be applied to the layer where the information is previously registered in order to move the bits back to their original position. Moreover, in both of the structures there has to be at least three buffer bits at the end of each magnetic layer in order not to lose any information during horizontal domain all motion. These buffer bits at the end must not be copied vertically by VCSELs during vertical register operation. This could be done by displacing VCSELs above or below these bits.

2.7. Conclusions

As explained in the introduction chapter, information storage industry constantly looks for novel methods to increase data storage capacity of devices and the frontier of magnetic recording is expected to be a three dimensional magnetic memory device. In this chapter, a novel three dimensional opto-magnetic memory device, which combines recent optical techniques, spintronics and magnetic materials all together, is proposed. These two patented structures have a high potential to solve the problems that the industry faces such as production cost, power consumption, limited storage capacity etc. However it should never be forgotten that, the proposed structure is only a premature idea. Even though every part that made up this device has been experimentally demonstrated piece by piece by other scientists and proved to be practical, the total structure has not been fabricated and demonstrated yet. There is still a long path that must be taken before the proposed device can become commercialized. All of the ideas explained above must be engineered very well for this device to work properly in the most efficient way. All in all, the way that those devices operate is unique compared to other three dimensional magnetic memory alternatives in nowadays technology and also they are open to innovations and engineering. Therefore these structures hold a very good position among all three dimensional magnetic systems put forward before.

3. THIN FILM APPLICATIONS

As explained in the first chapter, our three dimensional system is a multilayer stack. In order to fabricate this stack, the two dimensional layers must be deposited on top of each other with appropriate methods. There are several techniques for depositing two dimensional thin films such as thermal evaporation, chemical vapour deposition, sputtering, molecular beam epitaxy etc [26]. One of the most common methods and the one we used is sputter deposition, which is a physical vapour deposition technique. In this method, one can deposit thin films of magnetic and nonmagnetic metals and it also allows deposition of insulating materials in a vacuum chamber. The thickness of thin films ranges from nanometres to micrometres depending on the need and purpose. The system we operate is a magnetron sputtering system with both Direct Current (DC) and Radio Frequency(RF) power supplies.

3.1. Magnetron Sputtering

Sputtering uses energetic ions to eject atoms from a target(source) material and deposit them on a substrate [26, 27]. Both the target and substrate are placed in vacuum chamber. Even tough there are different designs of vacuum chambers; the fundamental parts and operation are the same for all systems. The target acts as cathode and the substrate acts as anode. Once the air in the chamber is evacuated, the chamber is filled with an inert gas, typically Argon, with a pressure ranging from few to hundreds of millitorrs. When a DC voltage is applied to the electrodes, a glow discharge occurs hence accelerates free electrons with sufficient energy to ionize Argon atoms. As a result, plasma of Argon gas can be observed in the chamber. The Ar gas density and applied voltage must be adjusted properly to initiate plasma. It should be noted that only a small fraction of Argon atoms (around one percent) is ionized. The resulting Ar^+ ions strike the target material and cause ejection of neutral atoms from the source through momentum transfer. Then the ejected atoms ballistically fly in straight lines and fall on the substrate. As this process continues, thin film grows on the substrate, usually in an amorphous state. Magnetron sputtering is to implement

strong magnets around the target electrode in order to confine ionized gas closer to target surface. This results in higher sputtering rate and allows deposition at lower gas pressures. Since the sputtered atoms are neutral, they are not affected by the magnetic field. Moreover, in order to deposit thin films of insulating materials and some metals, instead of DC power, an alternating electric field with a frequency of around 15 MHz is applied to target material. This method is called RF sputtering. The details of the sputtering system that we used in our lab are given in Appendix A.

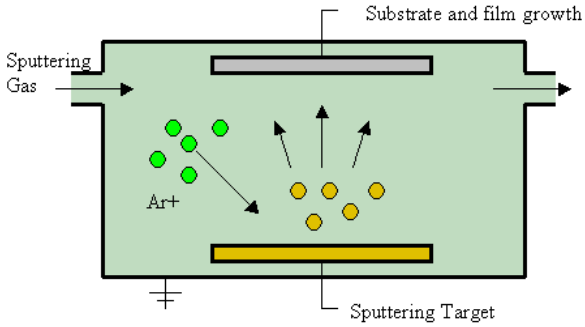


Figure 3.1. A basic schematic of sputtering process.

During deposition of materials, the atoms sputtered from the target not only falls on the substrate but also on every surface inside the vacuum chamber. After several depositions, the walls of the chamber and pieces inside the chamber are all coated with the target material. This residual material inside the vacuum chamber makes it harder to obtain vacuum conditions and affects the purity of the deposition. That's why, every piece inside the vacuum chamber must frequently go through a cleaning procedure. In this procedure, first, each piece inside the chamber is demounted and sandblasted. Sandblasting is to send very fine particles (mostly sand) unto a surface at high speeds to etch the coated thin film from the surface. A sandblaster consists of a container where the process occurs inside, an air compressor which helps sending particles at high speed and a nozzle which repels particles and is controlled by the user. After sandblasting, the cleaned pieces must be kept clear of any dust particle or any chemical such as oil. For this, pieces are immersed first in acetone and then in isopropanol in ultrasonic bath for about 15 minutes. After that the particles must be dried with N_2 gun and with heatgun to remove moisture. When the pieces are cleaned like this, it is easier to obtain higher vacuum conditions in the vacuum chamber. It must be noted that, any piece inside the vacuum chamber should not be touched with

bare hands since human skin leaves oil on the pieces.

3.2. Calibration Procedure

In order to calibrate the sputtering rate of each target depending on the parameters, one has to run through a specific procedure. This calibration procedure gives information about the final deposited thickness on a substrate of a specific target (material) depending on the parameters such as sputtering duration, substrate heating, applied power, Argon gas flow rate, base vacuum pressure and sputtering pressure.

For this purpose, one has to deposit the material on pre-patterned substrates on which one can measure the thickness of the deposited material after sputtering. That's why one needs to deposit steps on a substrate. A profiler then can be used to obtain the two 2D height profile and determine the thickness of the deposition.

To calibrate our targets, we used our pre-patterned calibration grating wafers that were fabricated with photolithography. These wafers are coated with photoresist partly. After sputtering, the whole area of the wafer is coated with the target material. This coated wafer then goes through the lift-off process. After lift-off, photoresist leaves the wafer with the coated atoms on it. As a result, the wafer is left with steps on it.

3.2.1. Photolithography

Photolithography is a microfabrication process used to fabricate geometrical patterns on a thin film or on a substrate. In this process, a photomask is used to transfer the patterns onto the substrate which is coated with a chemical called photoresist [1, 26].

The substrate, on which the patterns will be fabricated, is first spin-coated with photoresist with a thickness around one micron. This photoresist is a radiation sensitive polymer. Light exposure on that chemical causes changes in the polymer chains, they are either broken or become cross-linked. When the substrate is ready, it is exposed

to light (typically in UV regime) through the photomask. Since the mask has the patterns, only specific regions of the substrate is illuminated. After that, the substrate is immersed in a solvent liquid called developer. This chemical dissolves either exposed or unexposed parts of the resist, depending on the resist type. As a result you have the image of the mask on the substrate. At this step fabrication can be done by dry etching or post-deposition by lift-off.

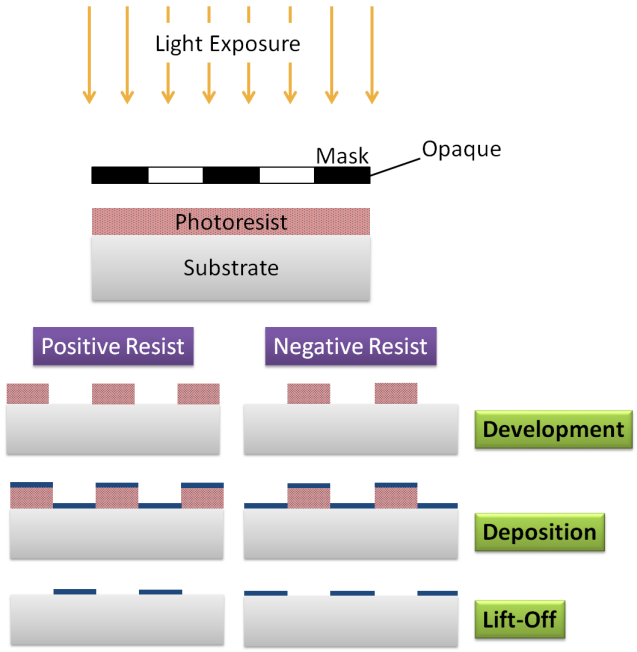


Figure 3.2. Description of photolithography and lift-off steps with positive and negative photoresist.

There are 3 fundamental elements for photolithography. First, one uses an illumination system which uniformly shines light on the substrate through the mask. The wavelengths of light usually used are 300-450nm (mercury lamb), 436nm(g-line), 365nm(i-line) or in the deep-UV regime 248nm KrF and 193nm ArF. In optical lithography, smallest feature size that can be patterned namely the resolution, R, depends on

$$\frac{K_1 \lambda}{NA} \tag{3.1}$$

where, K_1 is the process dependent parameter ($\sim$0.6), λ is the wavelength of exposure and NA is the numerical aperture. Second is a photomask. It is typically chrome-on-

glass. A dark field mask is when the inside of the patters are transparent(glass) and outside is chrome. A light field mask is when the inside of the patterns are chrome and outside is transparent. Third is an exposure system (Mask Aligner) where one inserts substrate and mask. This device generates light and shines it on the workpiece through the photomask. Depending on the work, one can perform contact lithography or proximity lithography. In contact lithography the mask and the substrate remains in hard contact during exposure. This offers high resolution but may damage the sample or the mask. In proximity lithography, the mask is kept few microns away from the substrate, however this method reduces resolution. The details of our photolithography process is explained in detail in Appendix B.

3.2.2. Photomask

To design our mask, we used L-Edit (Layout Editor) computer software. Aim of this software is to design circuits and layouts for various purposes. We only used it to draw geometrical patterns for the mask. Then we export our design as a Graphic Database System(GDS) file and send it to National Nanotechnology Research Center at Bilkent University where they have mask writer to produce our mask.

Our mask is 5" $\times$ 5" and the features are inside a 3.5" wafer sized circle in the middle of the mask as illustrated in Figure 3.3. Optic microscopy photos showing the dimensions of the patterns on the mask are also shown in the following Figure 3.4.

3.2.3. Deposition and Lift-Off

Once photolithography is completed, we are left with patterned silicon wafers coated with photoresist. In our process, we used dark field mask. This means that the outside of rectangular shaped patterns are coated with photoresist(PR) and the inside is hollow as illustrated in the previous section. The next step in the calibration procedure is to deposit thin films onto these pre-patterned substrates. The resulting substrate will be successive layers of silicon wafer, photoresist and deposited material as can be seen in Figure 3.2. Not only the hollow areas but everywhere on the silicon

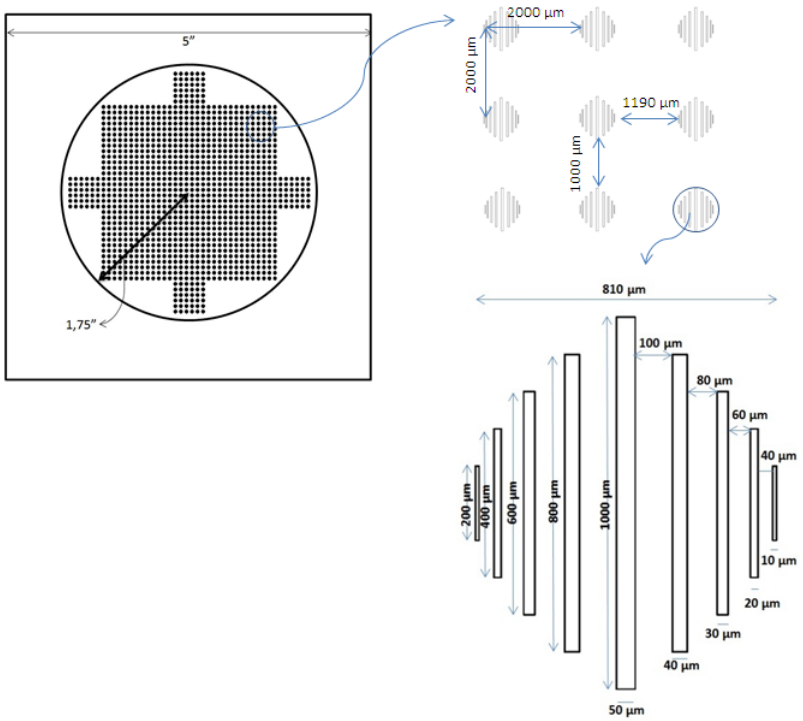


Figure 3.3. Schematic drawing of our mask design for calibration procedure.

wafer is coated with the target material. The essential point in here is to sputter with different conditions. One must sputter with different values of Argon gas pressure and applied power to observe how the sputter deposition rate changes according to these parameters. Other than two, the calibration experiments can also be performed to see how substrate spin rate, temperature of substrate and the distance between substrate and target affect the deposition rate. While the former two parameters are directly related to thickness of deposition, the latter three parameters are mostly in charge of crystal structure of deposited thin film and the uniformity in thickness along the thin film. Note that depositions are always done at room temperature unless otherwise stated. One intermediate step before depositing materials is that when the sputtering begins the target materials must be conditioned for about 10 minutes. Since the target material is exposed to open air and sometimes demounted,kept in some place and mounted back, it is probable that the surface of the target is oxidized or become dirty. Conditioning is to sputter while the shutters (the metal plate in between the target material and the substrate) are kept closed so that the ejected atoms do not fall on the substrate. After conditioning, the target material will be cleaned from oxygen and dirt and pure target atoms will fall on the substrate when the shutters are open.

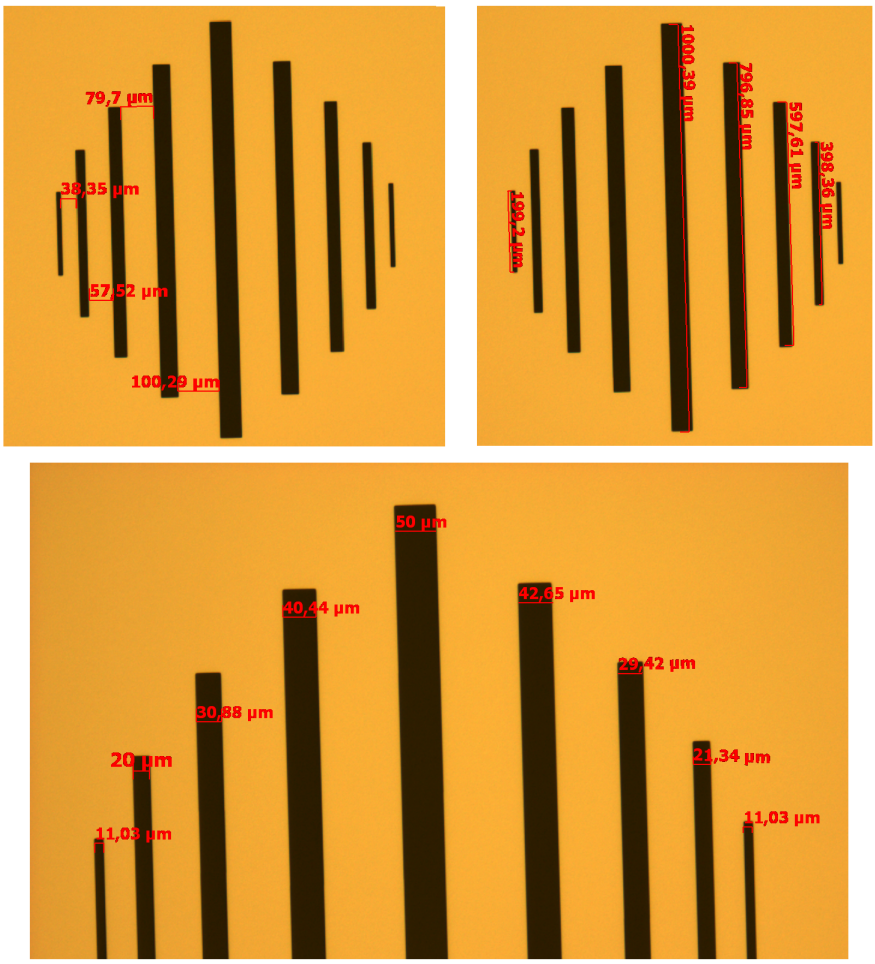


Figure 3.4. Optic microscopy of the photomask showing length,width and intervals of calibration gratings.

After deposition, the thin films go through a chemical process called lift-off. This is the step where the photoresist is removed from the wafer. Acetone is a very effective solvent for photoresist. The deposited wafers are immersed in acetone in an ultrasonic bath and then in isopropanol (to clean acetone on the wafer). In this process as the photoresist is solved in the acetone and removed from the wafer, the thin film which is deposited on top of photoresist is also removed from the wafer. As a result, there are only sputtered material on the wafer which were deposited on hollow parts of the geometric pattern. For our mask design, the wafer is coated with rectangular bars, forming steps next to each other in order to measure the thickness of deposition.

3.2.4. Surface Profilometry

A stylus profiler [28, 29] can be used to measure step heights on a wafer. Stylus profilers are extensively used for 2D or 3D surface topography measurements. Their primary function is to scan a line over a thin film and measure the step heights or trench depths. The main part of a stylus profiler is a very sharp diamond stylus moving along a thin film, or a thin film moving under the sharp tip. A true stylus profiler scans linearly and moves vertically when it faces with surface features such as step, any irregularity or a trench. These machines are so sensitive that one can obtain sub-nanometre accuracy in a 2D graph. Some devices are also capable of scanning adjacent lines next to each other to obtain a 3D surface topography, hence can calculate surface roughness and stress.

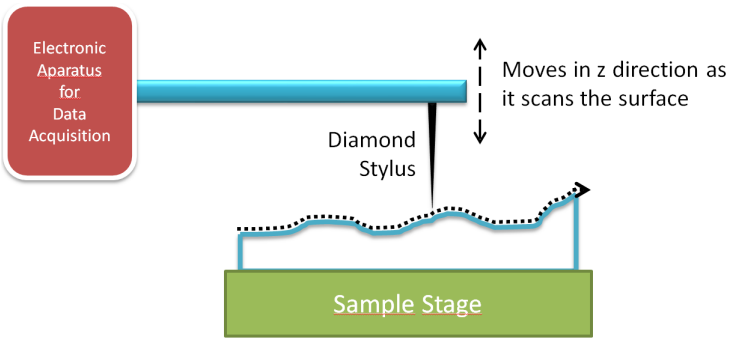


Figure 3.5. Schematic description of a surface profiler.

Profilers consist of three main parts; the stylus, which makes physical contact with the surface while scanning and produces vertical height data, an electronic system which gathers height information from the stylus tip and creates electrical signals and a computer to visualize a two dimensional graph from those electrical signals. Depending on the brand and model, different kind of sensor mechanisms are developed. The system that we have used in our lab is KLA Tencor Alpha-Step D100 surface profiler. The details about the instrument can be found in Appendix C.

Since a profiler is very sensitive, it is also vulnerable to any mechanical vibrations caused by the environment of the device. Any vibrations on the table, on the floor where the device is placed cause disturbances throughout the measurement. That is why it is better to place the profiler on a vibration isolation table. These tables

absorb every mechanical vibration due to building and the floor and hence prevent the measurements be affected by those mechanical noises. In order to show the difference in accuracy and noise reduction, two measurements obtained with our profiler with and without vibration isolation table is shown in Figure 3.6. As it can easily be seen, the graph obtained when the profiler is placed on an ordinary table is much noisier than the one taken when it is set up on a vibration isolation table.

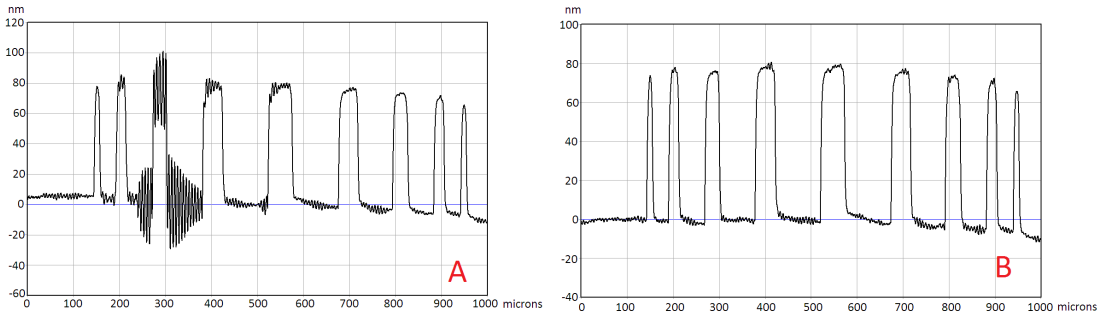


Figure 3.6. Comparison between the measurements with(B) and without (A) vibration isolation table.

3.3. Thin Film Experiments

In this section, thin film deposition of different materials will be explained. Details of sputtering parameters, optical microscopy images and profiler measurements will be given. For all of the samples, the materials are deposited on Si wafers which are patterned with calibration gratings beforehand via photolithography as explained in section 3.1. Below is a line scan of a photoresist coated wafer. PR coated wafer is scanned with stylus profiler. As can be seen in Figure 3.7, the thickness of the photo resist is about 1.2 microns. Figure 3.8 is an optic microscopy photo of a wafer after lithography, showing the dimensions of the calibrations gratings. Unless otherwise situated, stylus profiler scan parameters are 0.1 mm/s scan speed, 1mg stylus force and around 10k-20k data points. The thicknesses measured with stylus profiler are given with $\pm$ sign. This kind of representation does not mean uncertainty but related to uniformity of deposited thin film. Over a full 4" Si wafer, thickness of deposition differs within few nanometres as stated with the $\pm$ sign.

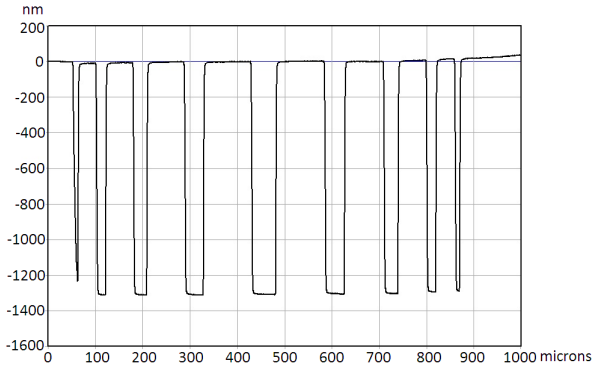


Figure 3.7. Surface line profile of photoresist coated patterned wafer.



Figure 3.8. Optic microscopy of a photoresist coated wafer, showing the dimensions of calibration gratings.

3.3.1. Aluminium Deposition and Calibration

Sputtering parameters are 20sccm argon flow rate, 5×10^{-6}Torr argon pressure, 150Watt DC applied power and 50 minutes sputtering duration. After deposition, two Al coated wafers are processed to remove PR as explained in the lift-off section. First, they are immersed in acetone for about 5 minutes and then in isopropanol for again 5 minutes in ultrasonic bath (without heating, 53 kHz). Immediately after that, we washed wafers with distilled water and dry with N_2 gun. Optic microscopy photo after lift-off is given in Figure 3.9. The features are aluminium and the rest is silicon wafer surface.

Aluminium deposited wafers are scanned with stylus profiler (2mg stylus force).

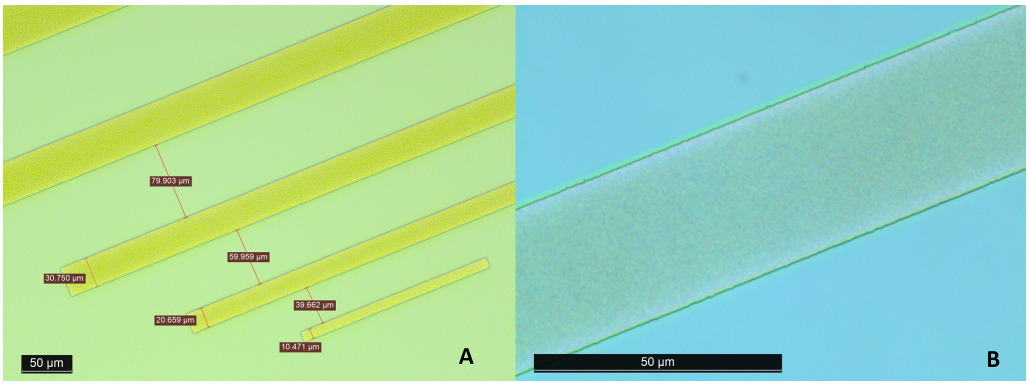


Figure 3.9. Optic microscopy photos of aluminum deposited wafer. Figure A shows the dimensions of the calibration gratings and figure B shows that the edges are sufficiently clear and straight.

A line profile over a feature is shown in Figure 3.10. As the line profile shows, the thickness of aluminium film with these sputter conditions is 280±10 nm.

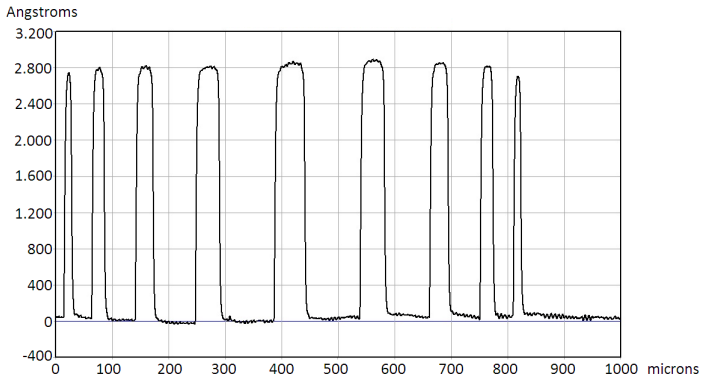


Figure 3.10. Stylus profiler line profile showing the thickness of aluminium gratings on silicon wafer.

3.3.2. Copper Deposition and Calibration

Sputtering parameters for the first sample is 6.8×10^{-6}Torr base pressure, 80Watt DC applied power, 5sccm argon flow rate, 7mTorr argon pressure and 30 minutes of sputtering duration. After deposition, the sample is immersed first in acetone and then in isopropanol, five minutes for each, in ultrasonic bath. The thickness measured with the profiler(0.8 mg stylus force) is 655±15 nm. The line profile is given in Figure 3.11.

For the second sample, the sputtering parameters are 1.3×10^{-5}Torr base pres-

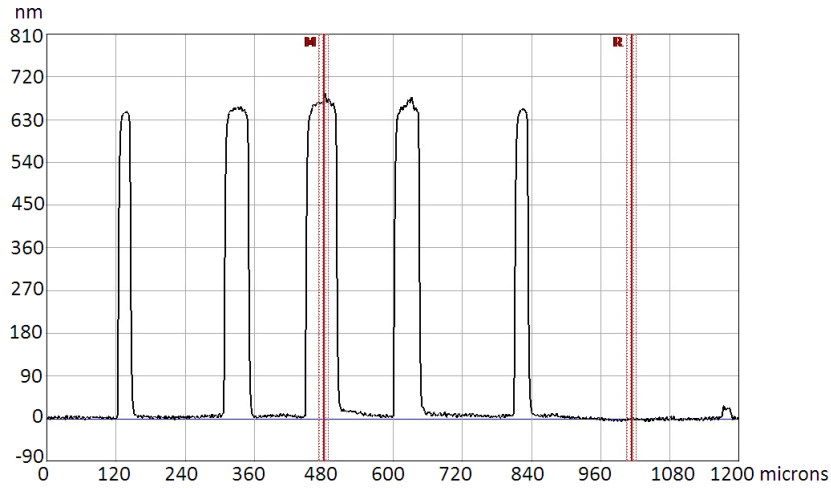


Figure 3.11. Stylus profiler line profile showing the thickness of copper gratings on silicon wafer for the first sample.

sure, 50Watt DC applied power, 6mTorr argon pressure, 5sccm argon flow rate and 10 minutes sputtering duration. The sample is immersed first in acetone and then in isopropanol, one minute for each, in ultrasonic bath after deposition. Step profile taken with stylus profiler is given in 3.12. The measured thickness is 120±10 nm.

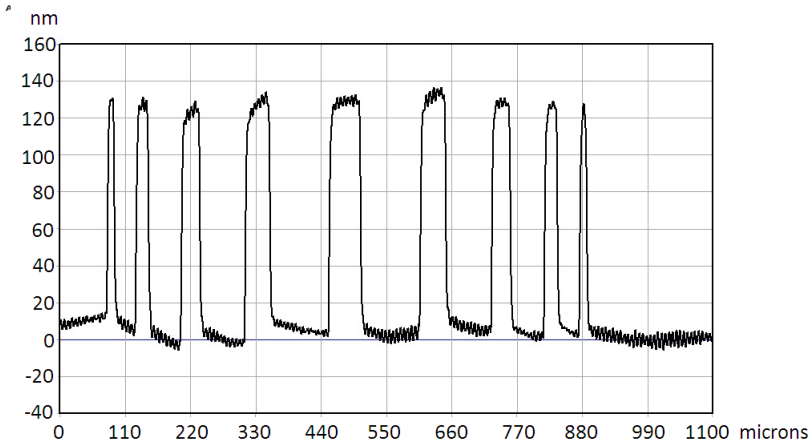


Figure 3.12. Stylus profiler line profile showing the thickness of copper gratings on silicon wafer for the second sample.

Finally, the third sample is sputtered under conditions of 2.7×10^{-5}Torr base pressure, 50Watt DC applied power, 5sccm argon flow rate, 6mTorr argon pressure and 20 minutes of sputtering duration. Again the sample is immersed first in acetone and then in isopropanol, one minute for each, in ultrasonic bath for the lift-of process. The measured thickness is 275±10 nm, as given in Figure 3.13 taken with stylus profiler.

Here we can see that the thickness of the coating is linear with the sputtering duration. It should be noted that for we kept the substrate in the ultrasonic bath only for 1 minute, we see photoresist residues on the unpatterned parts.

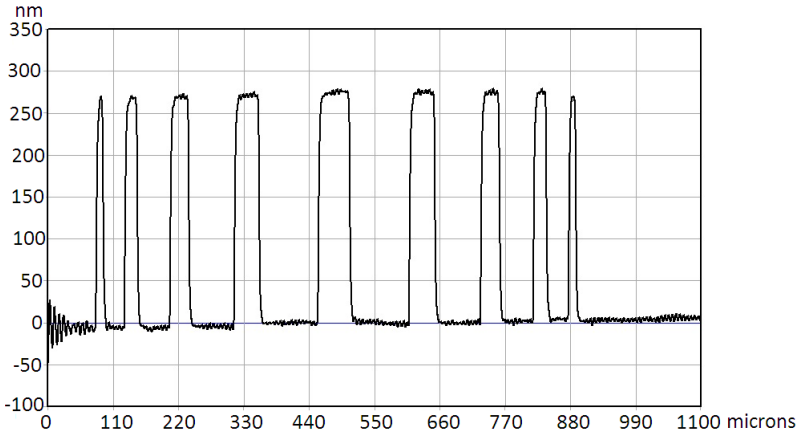


Figure 3.13. Stylus profiler line profile showing the thickness of copper gratings on silicon wafer for the third sample.

3.3.3. Silicon Nitride Deposition and Calibration

Sputtering parameters for the first silicon nitride deposition are 3.7×10^{-6}Torr base pressure, 5sccm argon flow rate, 10 mTorr argon pressure, 200Watt RF applied power and 15 minutes of sputtering duration. Under these conditions the deposition was successful and the line profile is given in Figure 3.14. As shown in the graph, the thickness is found to be 35±5 nm.

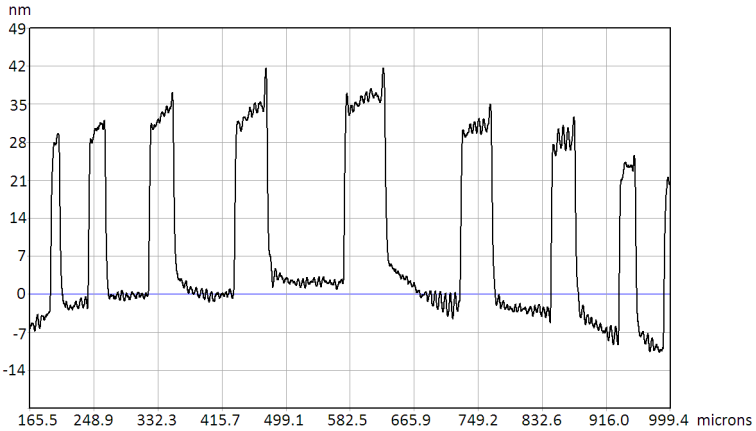


Figure 3.14. Stylus profiler line profile showing the thickness of silicon nitride gratings on silicon wafer for the first sample.

For the second sample the deposition is done under conditions of 2.2×10^{-5}Torr base pressure, 5sccm argon flow rate 10 mTorr argon pressure, 200Watt RF applied power and 30 minutes of sputtering duration. The thickness of the film is found to be 80±7nm and line profile is given in Figure 3.15.

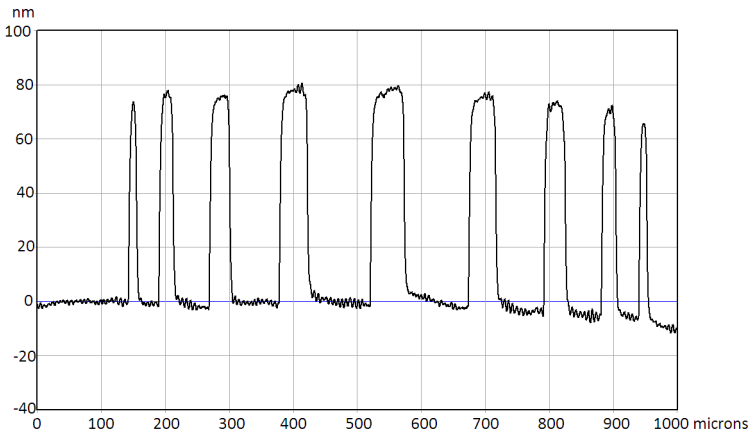


Figure 3.15. Stylus profiler line profile showing the thickness of silicon nitride gratings on silicon wafer for the second sample.

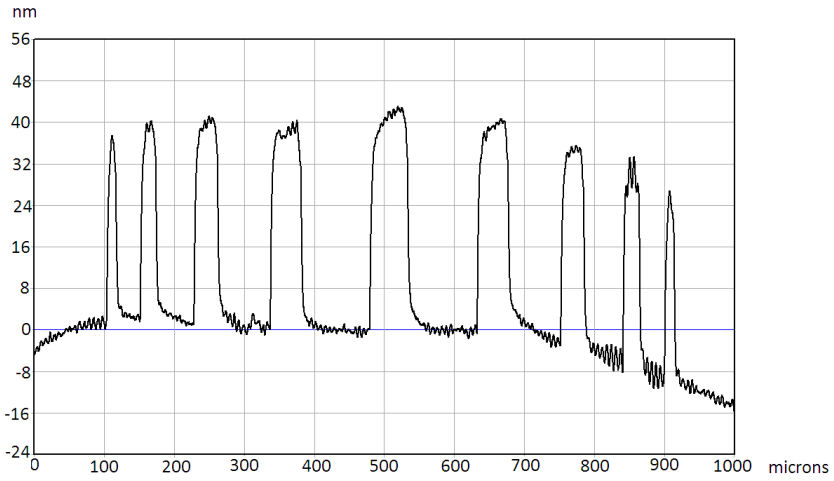


Figure 3.16. Stylus profiler line profile showing the thickness of silicon nitride gratings on silicon wafer for the third sample.

As it is explained in Chapter 4, the silicon nitride thin films deposited with 200Watt applied power are not rich in stoichiometric silicon nitride. That's why it is decided to deposit films with less power. The sputtering conditions for the new sample are 1.6×10^{-5}Torr base pressure, 5sccm argon flow rate, 10 mTorr argon pressure, 100Watt RF applied power and 30 minutes of sputtering duration. The thickness is found to be 42±5nm and the profiler scan is given in Figure 3.16.

3.4. CoNi/Pd Thin Film Deposition

To realize 3D magnetic memory structure, we have to facricate CoNi/Pd magnetic multilayers. As it is explained in the introduction, the magnetic layers are ferromagnetic nanowires with hexagonal constrictions. These hexagonal constrictions must be patterned via photolithography. For this purpose, it is needed to design a photomask which has bow-tie shaped patterns. In this section, the photomask design, sputter deposition and magnetic characterization of the samples with Vibrating Sample Magnetometry(VSM) method will be explained.

3.4.1. Photomask for bow-tie shaped patterns

First of all, by using computer software L-Edit, we designed our photomask. After that, GDS file is exported and sent to Bilkent University for the fabrication of the mask. Different than before, this time we are going to have two masks to pattern our nanowires. As it is seen in the figures, on the sides of bow-tie shaped magnetic patterns, there are conducting electrical contacts. Since these two layers must be fabricated separately, We have to use two different photomasks, one of which has the bow-tie pattern and the other only has electical contacts' pattern. It should be noted that, we have to put alignment marks on both of the masks. Because we are going to fabricate two different materials on the same silicon wafer, we will need a method to match the patterns of both masks.

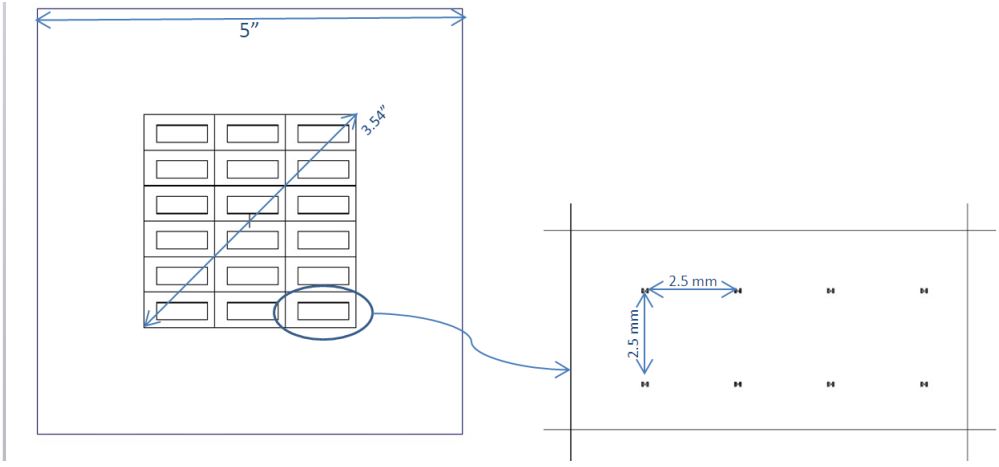


Figure 3.17. Design of the mask.

Figure 3.17 shows a picture of the 5" mask. The patterns are placed at the center, inside a circle of diameter 4". Each small rectangle contains 8 patterns. Since there are 18 rectangles, 144 bow-tie shaped patterns will be fabricated at each photolithography process.

There are 4 big alignment marks (cross) placed at the middle of each side of the square. This is for coarse alignment of the two masks. Also, in order to do the fine alignment, we put small alignment marks (cross). As it is seen in Figure 3.18 these small marks are placed around the patterns. The patterns which are at the very corners of the mask have these small alignment marks.

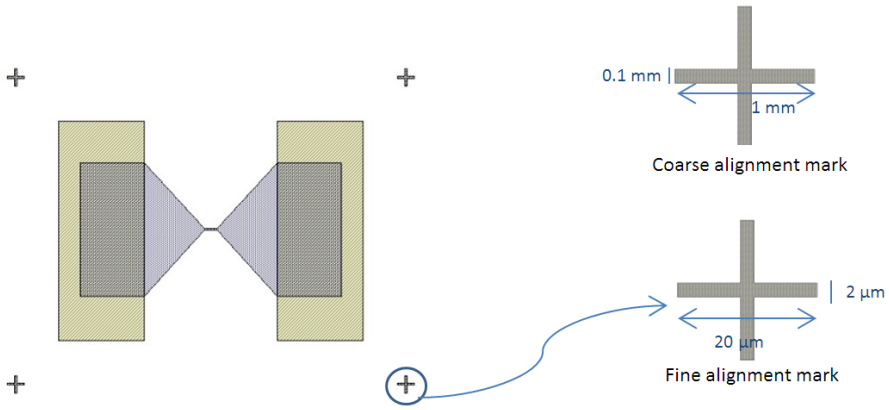


Figure 3.18. Picture of the mask showing the dimensions of the alignment marks.

Figure 3.19 shows the bow-tie shaped pattern. The blue areas represent magnetic material and the yellow areas represent the gold contacts. So, different coloured areas are on different masks. For our purposes, we need microwires with different dimensions. Dimensions of microwires corresponding to each rectangular area are 2×10, 2×8, 2×6, 2×4, 2×20, 2×15, 2×16, 4×20, 4×16, 5×15, 5×10, 3×30, 4×30, 5×25, 5×20, 7×21, 10×20 and 4×40 (all in microns). Secondly, we have two different samples in the case of the dimensions of gold contacts. One of them has contacts with dimensions of 100×250 microns and the other one has dimensions of 75×150 microns.

Figure 3.20 and Figure 3.21 shows optic microscopy images of patterns on the photomask. Yellow areas are chrome which reflects light and inside of the shapes are transparent(glass).

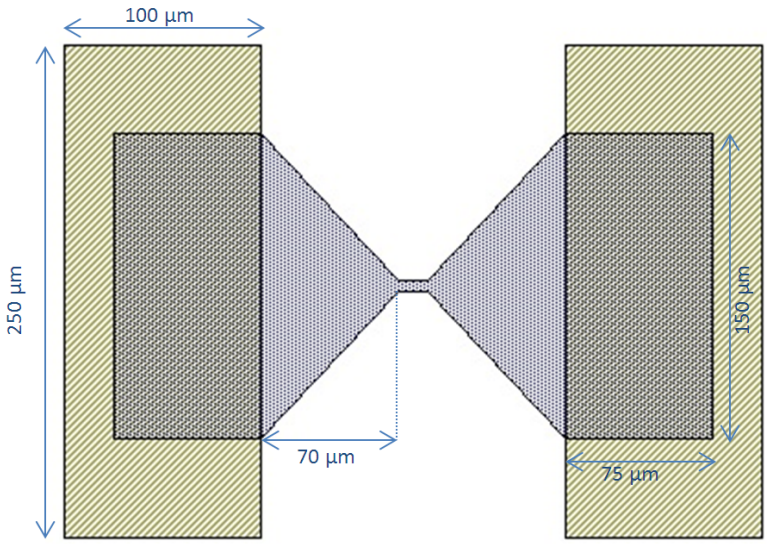


Figure 3.19. Picture of the mask showing the dimensions of the bow-tie shaped patterns.

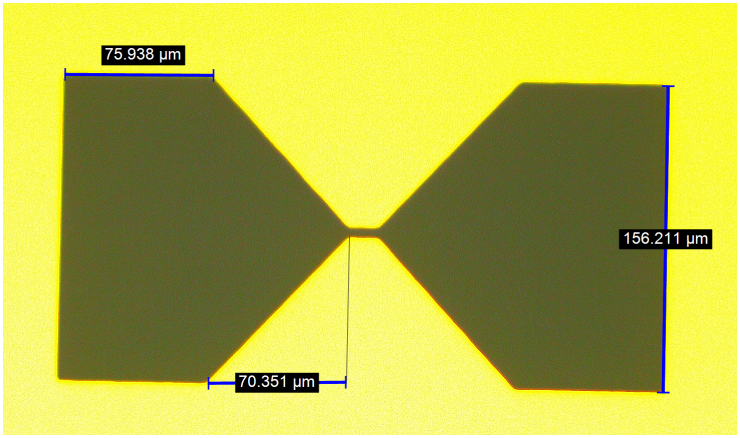


Figure 3.20. Optic microscopy image of the mask showing a bow-tie shaped pattern.

3.4.2. CoNi/Pd Deposition

In order to deposit CoNi/Pd multilayers, two different sputtering targets, CO_5Ni_5 and Pd targets, are used. Sputtering parameters for deposition are 5×10^{-7}Torr base pressure, 5sccm argon flow rate, 5mTorr argon pressure and 30Watt DC applied power. Under these conditions the deposition rate is found to be 0.01 nm/s for CoNi and 0.02 nm/s for Pd. The magnetic multilayer stack consists of Pd(3nm) / [CoNi(0.22nm) / Pd(1.2nm)] x22 / Pd(2nm). Figure 3.22 shows optic microscopy images of deposited CoNi/Pd magnetic multilayer structures.

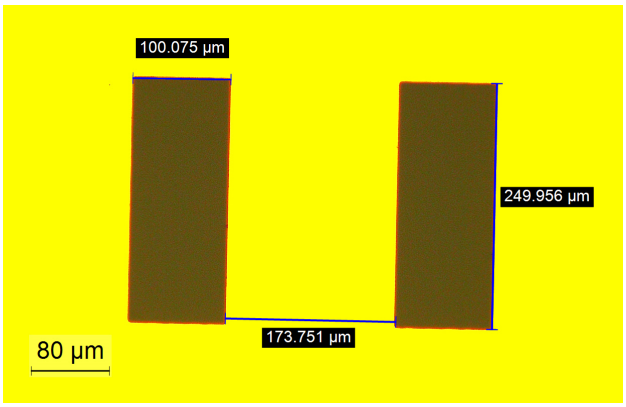


Figure 3.21. Optic microscopy image of the mask showing gold contact patterns.

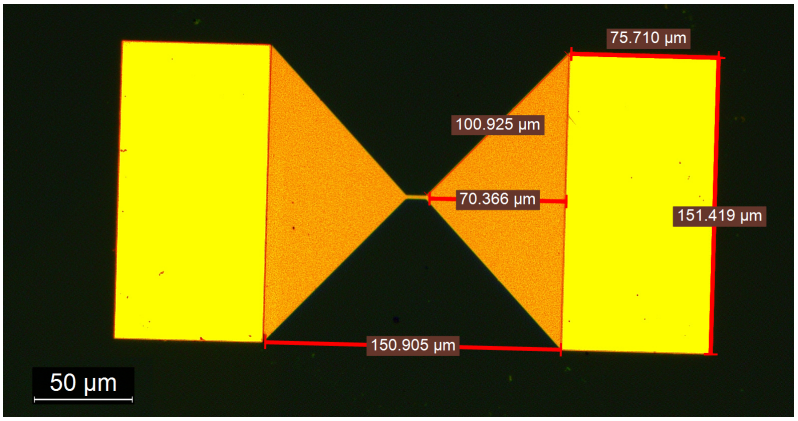


Figure 3.22. Optic microscopy image of a deposited bow-tie shaped pattern.

3.5. Electrical, Thermal and Magnetic Characterization of Samples

For our device applications, properties of the fabricated thin films are highly important. As it is explained before, silicon nitride is used as a spacer in three dimensional magnetic memory device, so it must be good at electrical and thermal resistivity. Thermal resistivity is important in the sense that the magnetic properties such as coercivity and saturation magnetization is highly affected by the temperature of the sample. Silicon nitride is used as a thermal barrier such that thermal instabilities within the device is reduced. On the other hand, since our magnetic memory system is operated via current application along magnetic nanowires, a highly resistive material must be used as a electrical barrier to prevent device malfunctioning. Finally, there is no need to mention that the magnetic properties are extremely important because our device is magnetic and based on the magnetic domains in the material. In this section several methods for electrical, thermal and magnetic characterization will be introduced and

the corresponding experiments will be reported.

3.5.1. Vibrating Sample Magnetometry Measurements

Vibrating Sample Magnetometry(VSM) [30] is a method to measure magnetization of the samples with respect to external magnetic field. It is based on measuring induced current in a coil when magnetic flux changes [31]. In the basic schema as illustrated in Figure 3.23, a small magnetic sample is attached to the end of a nonmagnetic rod and vibrated via some kind of mechanical vibrator. When the sample is vibrated, the change of magnetic flux causes electrical current in the pickup coils which are placed near to the vibrating sample. The magnitude of emf induced in the coils is proportional to the magnetization of the sample. The emf signal, then, is amplified with a lock-in amplifier and sent to electronics system that operates the device and data is taken with a computer software. The device that we used in our lab is VSM module of Quantum Design Dynacool Physical Property Measurement System(PPMS). This system uses a compact gradiometer pickup coil, a relatively large oscillating amplitude (1-3 mm peak) and frequency of 49 Hertz. Under these conditions the machine has resolution of 10^{-6}emu at a data rate of 1 Hz. It is possible to apply external magnetic field during the measurement and so obtain hysteresis loops of different kind of samples. Since the machine can go to very high and very low temperatures, hysteresis loops can be obtained at different temperatures.

The time dependent induced voltage in pickup coils is expressed by:

$$V_{coil} = \left(\frac{d\Phi}{dz}\right)\left(\frac{dz}{dt}\right) \tag{3.2}$$

where Φ is magnetic flux enclosed by pickup coils, z is the vertical position of the sample and t is the time. When the sample is oscillated sinusoidally, the final equation representing the voltage is:

$$V_{coil} = 2\pi f C m A \sin(2\pi f t) \tag{3.3}$$

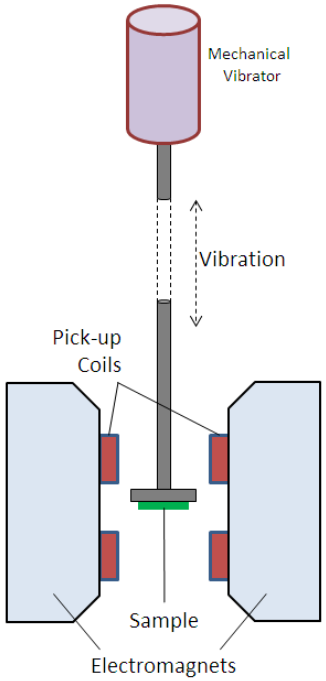


Figure 3.23. A basic schematic of vibrating sample magnetometer.

where C is the coupling constant, m is the magnetic moment of the sample, A is the amplitude of oscillation and f is oscillation frequency.

For the magnetic characterization of CoNi/Pd samples, VSM measurements are carried out. In Figure 3.24, perpendicular magnetic anisotropy hysteresis loop at room temperature is shown. To understand the existence of perpendicular magnetic anisotropy at high temperatures, in-plane (hard plane) magnetic measurements have been taken at 70°C and found that anisotropy field is 10kOe (Figure 3.25).

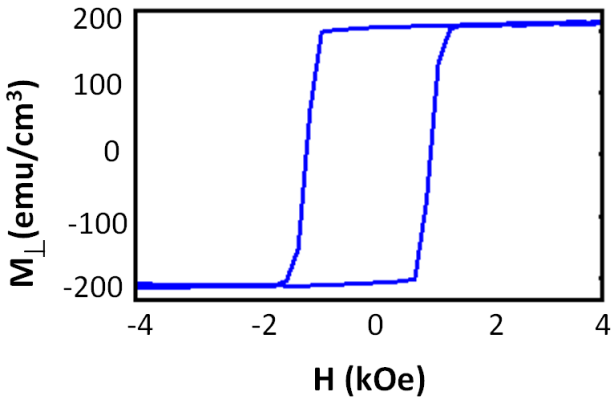


Figure 3.24. Perpendicular magnetic anisotropy hysteresis loop at room temperature.

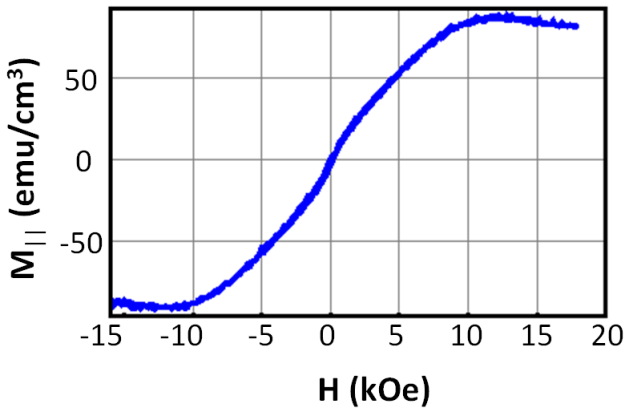


Figure 3.25. In-plane magnetic anisotropy hysteresis at 70°C.

In order to characterize saturation magnetization and the coercivity of fabricated magnetic samples, VSM measurements have been carried out with respect to temperature. Figure 3.26 and Figure 3.27 show saturation magnetization of thin films with respect to temperature under absence and presence of external magnetic field. These measurements show that, above 100°C, under absence of external magnetic field, magnetic domains form but the presence of external field does not allow domain formation. Also, Curie temperature under presence of 1 kOe external field is $165 - 175$°C as shown in Figure 3.26.

Coercivity measurement reveals that superparamagnetic region is just above 100°C as depicted in Figure 3.28. This means that it is enough to heat the samples up around 100°C when writing experiments will be done (for information on writing experiments, refer to first chapter).

Magnetic characteristics around superparamagnetic region, where magnetization reversal takes place, is highly important. Experiments show that magnetic anisotropy is 18 kOe at room temperature, 10 kOe at 70°C and 8 kOE at 100°C which means that magnetic anisotropy is still present in superparamagnetic region. But due to that coercive field is close to zero at that temperature range, magnetic anisotropy energy is comparable to thermal energy.

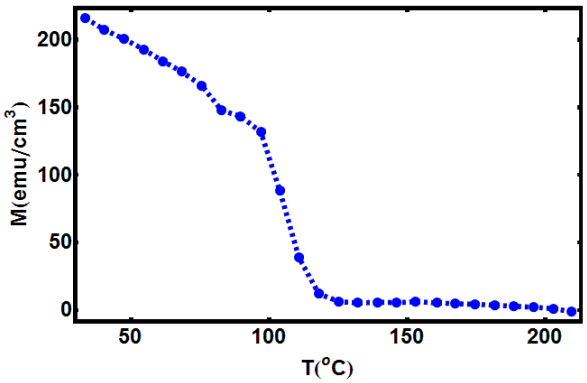


Figure 3.26. Saturation magnetization with respect to temperature at zero external field.

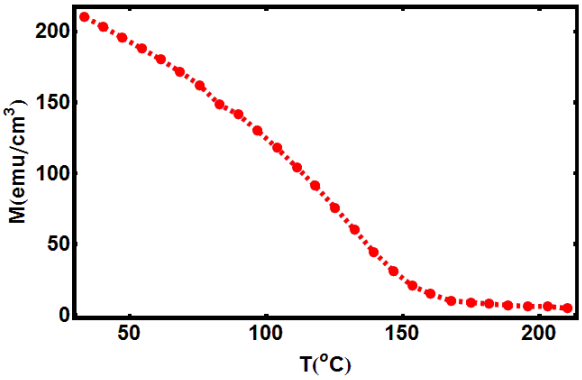


Figure 3.27. Saturation magnetization with respect to temperature at 1 kOe external field.

3.5.2. Four Point Probe Electrical Resistivity Measurements

Four point probe(4pp) is a method to measure resistivity especially for thin films [32]. In this method, four collinear connections are contacted to the surface of a thin film with equal intervals in between the contacts (approximately 1μm). While a current is applied through the outer probes along the film, the inner probes measures voltage drop. The key advantage of four point probe is that due to the separation of current carrying wires and sensing contacts, the voltage drop due to resistance of the probes is eliminated.

As illustrated in Figure 3.29, the current is applied through the first and the forth probes and voltage is measured in between the second and the third probes. Assuming

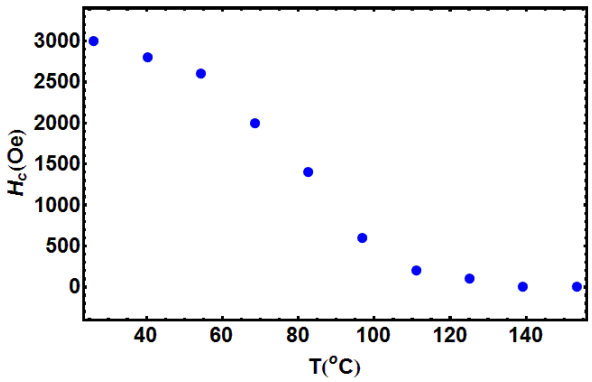


Figure 3.28. Coercive field with respect to temperature.

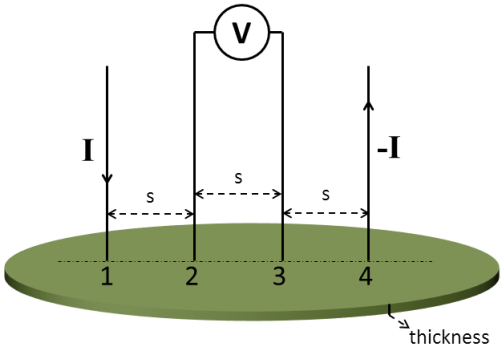


Figure 3.29. Four Point Probe Method.

an infinite sheet thinner than the probe spacing and no current flow in vertical direction the current density and ohm's law are given by

$$J = \frac{I}{2\pi r t} \tag{3.4}$$

$$E = -\nabla V = \rho J \tag{3.5}$$

where, J is the current density, I is the current, t is thickness, r is distance between probes, E is the electric field, V is the potential and ρ is resistivity and . By integrating the equation with appropriate limits, the voltage as a function of distance,r, is found to be

$$V(r) = -\frac{\rho I}{2\pi t} \ln(r) \tag{3.6}$$

Considering equal distances, s, in between the contacts, the voltage drop between the second and the third probes is found to be

$$V = \frac{\rho I}{\pi t} \ln(2) \tag{3.7}$$

From this the sheet resistivity, R_s is found to be:

$$\frac{\rho}{t} = R_s = \frac{V\pi}{I \ln(2)} \tag{3.8}$$

with 4pp method, electrical resistivity of silicon nitride and magnetic samples are measured. The electrical resistivity of stoichiometric nitride is given to be around 10^{14} ohmcm in the literature [27]. For the untreated samples fabricated with sputter system, electrical resistivity is measured to be 1.5×10^{10} ohm cm which is lower than the expected value. This result is considered to be due to our silicon rich samples. After annealing our samples in nitrogen atmosphere, which helps enrichment of stoichiometric silicon nitride, the electrical resistivity is found to be 2.5×10^{12} ohm cm. It is concluded that this resistivity value is high enough for our device applications.

Electrical resistivity of CoNi/Pd multilayer at room temperature is measured with four point probe method and found to be 30μ ohm cm. The change of electrical resistivity with respect to temperature (from 4.2K to 400K) is measured with PPMS system and the result is given in Figure 3.30.

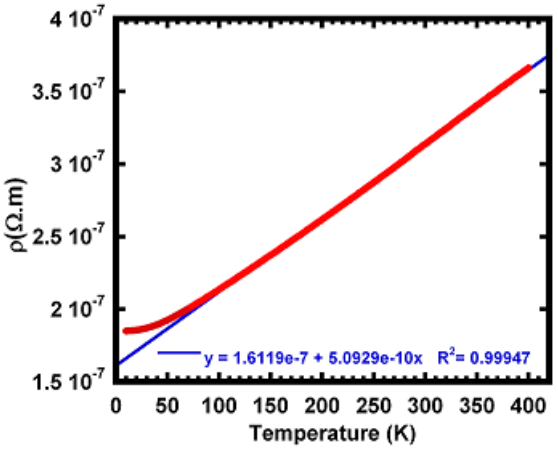


Figure 3.30. Electrical resistivity of CoNi/Pd multilayer with respect to temperature.

3.5.3. Thermal Resistivity Measurements

Thermal conductivity of fabricated thin films are measured with Hotdisk TPS 2500S thermal conductivity measurement system. For Si_3N_4 thin films, the thermal conductivity is found to be 3.2 W/mK and a significant change in this value is not observed when the sample is heated up to 100°C. Thermal conductivity of CoNi/Pd multilayers is found to be 20W/mK at room temperature. In order to understand whether the results are correct or not, thermal and electrical conductivity values are multiplied and divided by the room temperature

$$\frac{\kappa\rho}{T} = \frac{20 \times 30 \times 10^{-8}}{298} = 2.013 \times 10^{-8} W\Omega/K^2 \tag{3.9}$$

Since it is expected for the metallic structure to obey Wiedemann-Franz Law [33], it can be concluded that the results are correct within 10percent error due to that the resulting value in the equation is very close to Lorenz number, which is $2.44 \times 10^{-8}\mathrm{W\Omega K^{-2}}$. It must also be noted that the Lorenz number is a theoretical value and the real value for different type of metals varies within 10percent of the theoretical value [34]. By Wiedemann-Franz Law, the thermal resistivity at 100°C can be calculated to be 21.5 W/mK.

4. STOICHIOMETRY OF FABRICATED THIN FILMS

Electrical, magnetic and thermal properties of the materials that we use for our purposes are significantly important. For the memory device explained in the introduction to work properly, the spacer layer must be good in terms of thermal and electrical resistivity. The material chosen for this aim is Si_3N_4 which is called stoichiometric silicon nitride. We deposited thin films of Si_3N_4 as described in the previous chapter. However, it must be justified whether the samples produced are exactly Si_3N_4 or any other amorphous composition of these two elements, because the chemical structure of the samples directly affects electrical, thermal and magnetic properties. In order to understand the chemical composition of our fabricated samples, we performed stoichiometric analysis using two different methods, Energy dispersive X-ray Analysis (EDS), X-ray Photoelectron Spectroscopy (XPS) and the experiments are the subject matter of this chapter.

4.1. Energy Dispersive X-Ray Spectroscopy

A chemical analysis of a solid sample can be obtained by examining the spectrum of X-rays emitted by the sample under the bombardment of focused beam of electrons [35, 36]. The atoms ranging from atomic number 4 to 92 can be identified within a specific volume of a sample and their relative ratios of amount or weights of elements can be deduced. Since the emission of X-rays comes not only from the surface but also deeper regions of the sample (few microns), EDS is not a surface analysis technique. A simple qualitative analysis of the peak lines in the X-ray spectra helps identification of elements, whereas the proper quantitative analysis of the intensities of those peaks results in the determination of concentration of elements. The simplicity of this technique lies in the fact that every electronic transition in between energy levels of atoms has a characteristic wavelength in the X-ray spectrum such that it is easy to identify elements by looking at the energy of the emitted radiation.

Prior to emission of X-rays, a sufficient amount of electron bombardment on the

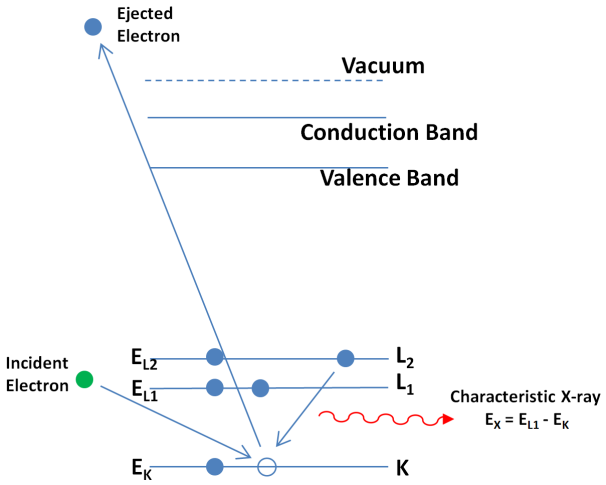


Figure 4.1. Basic working principle of EDS.

sample is necessary. That is why EDS instruments are mostly installed in scanning electron microscopy (SEM) [35] systems because they generate focused electron beams to obtain images of sample on nanoscale. If an X-ray detector and corresponding analysers are also installed in it, then the same tool can be used for chemical analysis.

Under bombardment of electrons, a solid sample generates two kinds of X-rays. One is the characteristic X-ray which results from ejection of inner shell electron by the bombarding electrons and the other is continuum X-rays which result due to the deceleration of electrons in the coulomb field of the nucleus.

When an incident beam of electrons with sufficient energy hits the atom, an electron from the inner shell of the atom is ejected, leaving a hole behind. This hole in the inner shell is immediately filled by another electron from the outer shells of the same atom. The transition from an upper (high energy state) level to a lower (low energy state) level results in emission of radiation with a wavelength equivalent to X-rays in the full electromagnetic spectrum as illustrated in Figure 4.1. The energy of the X-ray is directly related to the atomic number of the atom from which it is emitted. The minimum energy for the bombarding electrons to ionize an atom is called critical ionization energy. The magnitude of this energy is directly related to atomic number Z and increases with increasing Z. In practice, in order to have efficient excitations for probing atomic concentrations, the energy of the incoming electrons must be at least

twice of the critical ionization energy.

The characteristic X-ray lines are named with a Latin letter (K,L,M,...), a Greek letter (α, β, γ) and a number (1,2,3...).This nomenclature is known as Siegbahn notation [37]. As depicted in Figure 4.2, starting from the one closest to the nucleus, the electronic shells are named as K (the energy level corresponding to quantum number n=1), L (n=2), M (n=3) etc. as illustrated in the figure. So, if the initial vacancy occurs in the first level (or in the second level), the X-ray is named as K (or L). Also, if the transition from the outer layer comes from one level (or two level) away, the X-ray is named as α (or β) together with the Latin letter. For instance, if the electron makes a transition from M shell to K shell, it is named as K_β, or if the transition occurs from M shell to L shell, the produced X-ray is named as L_α. The final number describes to which subshell of a specific shell the transition occurs such as $L_{\alpha 2}$ or $K_{\beta 2}$. However, these numbers can be ignored because the energy difference in between subshells is so small that they cannot be differentiated within a peak line.

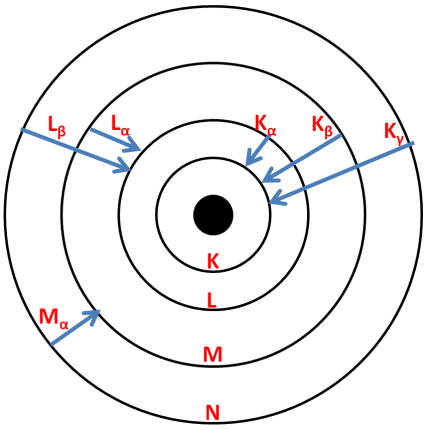


Figure 4.2. Nomenclature for characteristic X-ray lines with Sieghban notation.

The relation between the energy of X-ray radiation and the atomic number Z is given by Moseley's law [38] :

$$E = C_1(Z - C_2)^2 \tag{4.1}$$

Where E is the energy of the radiation, Z is the atomic number and C_1 and C_2 are the constants depending on the type of line. If the energy of a specific line is known, it is

straightforward to find atomic number of the element from which the X-ray radiation is originated.

The second most important result of the interaction between the sample and the incoming electron beam is the continuous X-ray radiation, the so-called Bremsstrahlung [39]. The incoming electrons can be inelastically scattered by the coulomb field of the nucleus, decelerate and give some of its initial energy off as X-ray radiation. Since the amount of energy that the electron can lose is not quantized but arbitrary, the resulting energy distribution of the radiation is continuous. The counts due to bremsstrahlung can be observed in experimental data as a background radiation over all energy values but the signal is too low compared to peak lines such that it does not affect the result of the experiment significantly.

Another important result is the emission of Auger electrons [36, 40]. If the radiation as a result of transition of an electron from an outer layer to fill a hole in the inner layer is absorbed by another outer shell electron, that electron may be ejected from the sample and named as Auger electron. The energy of an Auger electron is also specific to element it is ejected. They can be detected and contribute the X-ray spectrum. However, since only a few Auger electrons ejected from the surface of the sample can reach the detector, the contribution of Auger electrons in the line spectra can easily be neglected regarding the high intensity of X-rays coming from a thicker region of the sample.

Once the X-ray spectrum is obtained, the raw data must go through a rigorous analysis. The final data of EDS analysis are represented as a graph showing the number of counts versus energy. That graph mainly consists of a background radiation and peak lines. At first step, one must identify the position of those peak lines in order to figure out what elements are in the unknown specimen. This procedure is very easy by the help of tables of energies. It is very unlikely to misidentify an element since the ambiguities are very rare and peak lines are significantly separated from each other most of the time. After identification of elements, a rigorous quantitative analysis is needed to reveal the concentration of elements in the sample. Since each peak line

actually has a Gaussian shape, one needs to calculate the area under each peak after background subtraction is completed. Due to the parameters of measurement and the specifications of the measuring device, the very final result can be acquired after proper corrections to the raw data are done. Thanks to the state of the technology, all those analysis can be processed by computer software which also operates the device during the measurements.

4.2. X-Ray Photoelectron Spectroscopy

X-ray Photoelectron Spectroscopy (XPS) or Electron Spectroscopy for Chemical Analysis (ESCA) is a well-known surface analysis technique capable of determining the elemental and chemical state information of a surface of a sample [35, 41]. This method makes use of photoelectric effect that is the emission of an electron when a photon of specific energy falls on a material(Figure 4.3). Most commonly, monochromatic, low-energy X-ray radiation of K_α at 1486.7 eV or Mg K_α at 1253.6 eV is used to eject core level electrons from the surface of a material which is placed in ultrahigh vacuum. One can deduce the core level binding energy of the electron by measuring the kinetic energy of the emitted electron and using the following equation:

$$E_b = E_{X-ray} - E_k - \Phi \tag{4.2}$$

where Φ is the work function, E_b is the binding energy of the electron, E_{X-ray} is the energy of X-ray radiation and E_k is the kinetic energy of the electron. The energy of the photo-emitted electron is characteristic of the element from which it was ejected and also since it is sensitive to the chemical environment of that atom one can obtain the chemical state information of the sample. After a core-level electron is removed, an electron from the outer levels of the atom fills this hole, resulting in the emission of an Auger electron which is also detected by the equipment. Since these photoelectrons have relatively low kinetic energies, only those electrons which are closer to the surface can escape from the sample and hit the detector. That is why XPS is only sensitive to the chemical sate of the surface, tough, one can etch the sample surface with appropriate techniques and obtain chemical information of deeper regions. In most cases, XPS

machines are also equipped with ion guns for ion milling. After scanning the surface of the sample, the same spot can be etched with ions and scan can be repeated at the same spot but in a deeper region. Ion milling is to send beam of energetic ions (Argon) to etch the surface of the sample due to ballistic interactions. How deep the etching is performed can be calculated from the etch rate which depends on the sample, ion beam current and energy [42]. Successive etching and scanning can be performed many times on the same spot to obtain a full three dimensional stoichiometry of the sample.

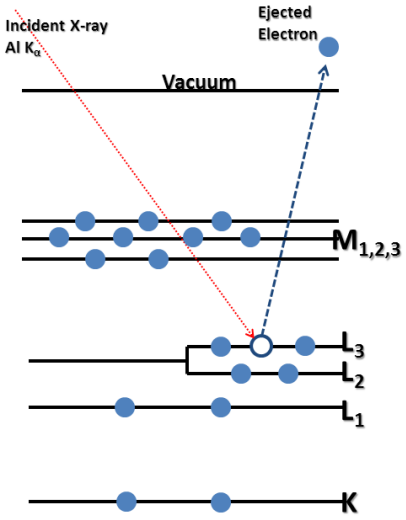


Figure 4.3. Representation of photoelectric effect under X-ray radiation.

The electrons emitted by radiation of X-rays and Auger electrons are detected by an electron energy analyser. By counting the number of electrons corresponding to the kinetic energy of electrons, appropriate computer software generates an intensity spectrum as a function of energy. Analyzing this spectrum gives elements which are present in the sample, the chemical composition of those elements and by calculating the area under the curves the relative amount of each element can be obtained.

Once the intensity versus energy graph is obtained, it must be followed with a very thorough analysis. After a successful experiment, the user is provided with two different data sets. One is a survey scan of the sample, which is scanning the sample with X-rays over full energy scale. This survey helps to understand what elements are present in the sample. After that, the second kind of data is high resolution scan, which is scanning the sample with X-rays over a narrower energy scale at and around

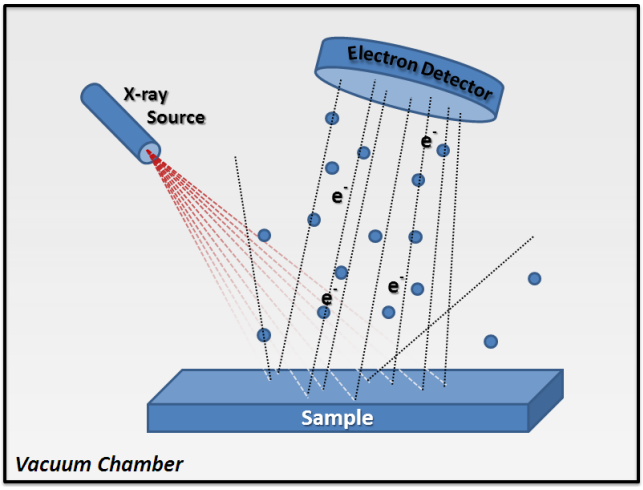


Figure 4.4. Schematic drawing of a basic XPS apparatus.

the peak positions. The second scan must be in high resolution such as 0.1 eV since peaks for different chemical compositions of each element varies on the order of 0.1 eV; whereas the survey scan can be in low resolution because it is just to identify elements in the sample.

The first step in qualitative analysis is the Carbon correction of the whole spectrum survey scan. Carbon 1s photoelectron energy corresponds to 285.1 eV and the position of the Carbon peak is taken as reference as a convention. If your C1s peak is not at 285.1 eV, the whole spectrum is shifted until the peak is exactly positioned at 285.1 eV. The identification of elements is accomplished with the help of National Institute of Standards and Technology (NIST) XPS database [43]. In that database, photoelectron energy values of every element including the values for element's different chemical compositions are listed. Secondly, proper background subtraction must be applied on every graph. There are different background removal methods in the literature such as linear, horizontal, Shirley's and Tougaard's [44]. As it is the most preferred and conventional method, we chose to apply Shirley background removal procedure in our quantitative analysis. The third stage in the analysis is treated on the high resolution scans of vicinity of each peak. The main task is to fit Gaussian and Lorentzian (GL) curves under each peak. The peak of each element is actually the sum of some number of different GL curves, each of which corresponds to different chemical compounds of that element. The reason behind is that even though the ele-

ment is the same, the electronic energy levels of that element differs depending on the bonds it makes. This property of the photoelectron spectrum gives the information not only about the abundance of elements but also abundances of different chemical compounds of each element. This comprehensive data analysis can be carried out with computer software easily. The examples of such software are XPSpeak, which is the most common and acceptable one, CasaXPS and some others specific to devices of different brands.

4.3. EDS Experiments

EDS experiments are done with The Philips XL30 ESEM-FEG/EDAX Scanning Electron Microscopy System which is situated in Boğaziçi University Advanced Technologies Research and Development Center. The result of EDS analysis on fabricated silicon nitride samples are shown in Figure 4.5. The atomic percentages are calculated as 83.3 per cent Si, 7.3 per cent O and 9.4 per cent N. It is obvious that the amount of silicon element is too high. The reason behind this is that due to device's conditions, in order to obtain X-ray signal, incident electron beam energy was adjusted to a high value (20kiloVolts) which in turn lead to detect signals not only from the deposited silicon nitride thin film but also from silicon substrate. The thickness of the thin film was about 120nm, however the penetration depth of incoming electrons were about 300nm. It can easily be concluded that, the EDS analysis is not successful. Therefore, stoichiometric analysis has to be done with XPS.

4.4. XPS Experiments

In this section, the results of XPS chemical composition analysis will be explained. Stoichiometric analyses are carried on sputtered silicon nitride samples. The analyses are done with Thermo Scientific K-Alpha Surface Analysis tool. The machine is controlled via computer software called Thermo Avantage. The machine runs in Constant Analyzer Energy (CAE) mode (also known as Fixed Analyzer Transmission) with pass energy 30 eV and Al K-alpha X-ray lines are used for the emission of photoelectrons. Peak identifications are always done according to NISTXPS database. Graphs in this

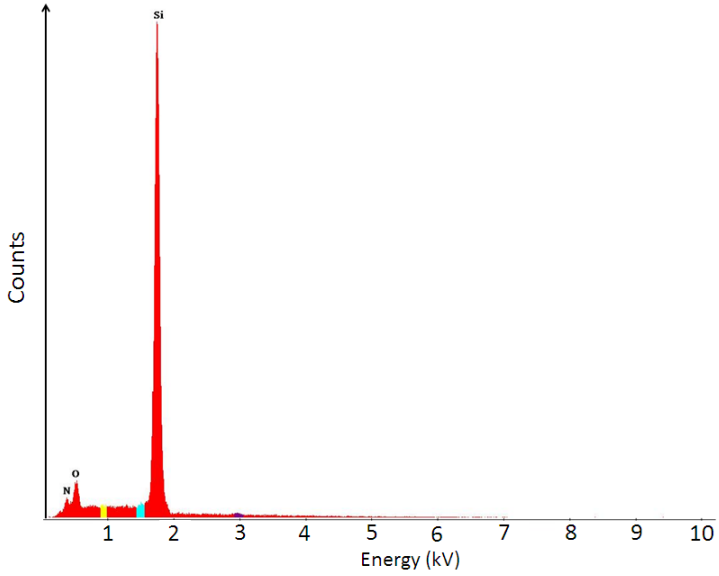


Figure 4.5. The result of EDX analysis on silicon nitride samples.

section show the number of counts per second with respect to binding energy values.

In Figure 4.6, the survey scan graphs of SiN thin films sputtered at 200W RF power are shown. The full energy scale (survey) scan graphs basically display what elements are present in the sample and give a rough estimate of their abundances. The figure on the left shows the surface scan whereas the figure on the right shows the scan taken from a deeper level after etching the surface with ion-milling. One can easily notice that amount of Oxygen in the thin films are too high not only at the surface but also in the interior parts. The level of oxygen on the surface can easily be caused by oxidization since the samples are exposed to atmosphere. On the other hand, the amount of oxygen in deeper level can be attributed to that which the power applied during the deposition of thin films are too high. The high power during sputtering energizes oxygen atoms in silicon wafer and allows them to contribute to the deposition. That is why we sputtered new SiN thin films at 100W RF power and apply XPS analysis again to see the difference. The results can be seen in Figure 4.7. As it can be seen, the amount of oxygen in the latter sample is less than the former samples. Moreover, the amount of oxygen in interior parts of the thin film is less than the value at the surface. Nevertheless, the total amount of oxygen is still too much in

the samples such that the sputtering deposition should be done in an ultrahigh vacuum environment.

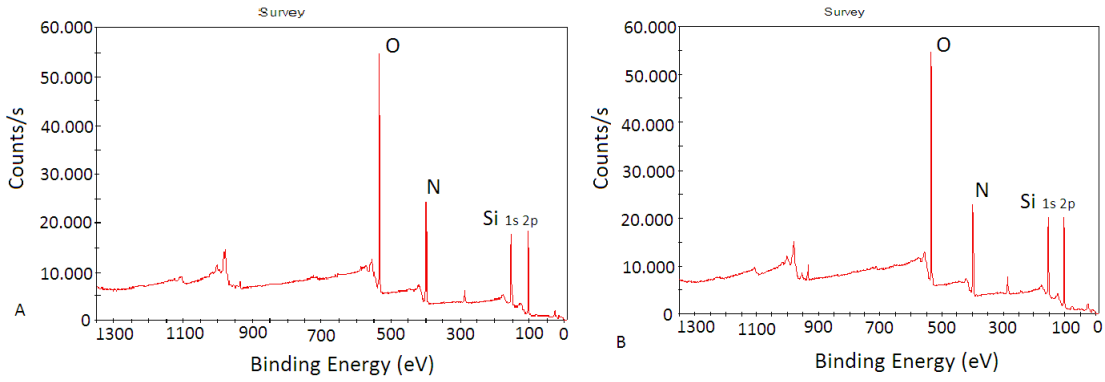


Figure 4.6. XPS survey scan on the surface(A) and at around 10nm below the surface(B)of silicon nitride sample deposited at 200W.

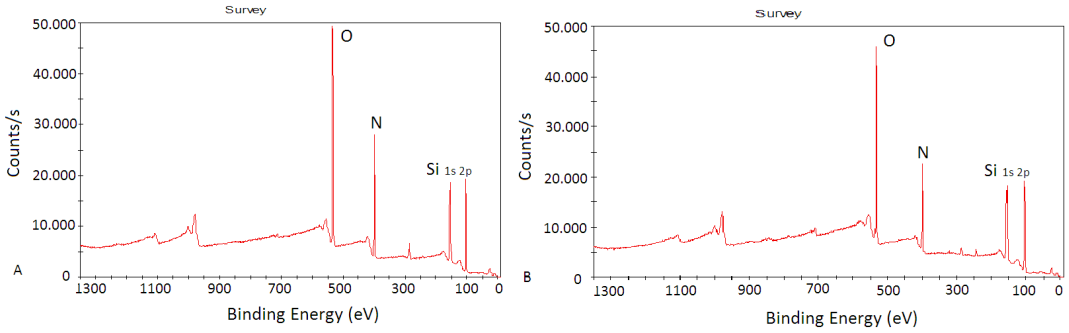


Figure 4.7. XPS survey scan on the surface(A) and at 25nm below the surface(B) of silicon nitride sample deposited at 100W.

It should be noted that, for the first sample how deep the sample is etched is unknown. Eventough the machine has a standard etch rate depending on the energy of the ions, etch rates differ from sample to sample. Therefore, we calibrated the ion-milling etch rate of the device on silicon nitride (Details of the calibration is explained in Appendix E). We figured out that for 1000 Volts ion energy, low current and 1mm raster size, the etch rate is 0.34 nm/s. Since the etching is done for 74 seconds in the second sample, we can for sure state that the scan was taken at a level which is 25nm under the surface.

Once the elements in the sample are identified, the sample is scanned with high resolution over a narrower energy range at and around each specific element. As it is explained in the previous sections, a very comprehensive data analysis procedure is

implemented on these high resolution data. By using computer software XPSPeak, the chemical compositions of each element are identified by fitting 90 per cent Gaussian-10 per cent Lorentzian curves under each high resolution curve. Before the fitting, Shirley background removal and carbon peak correction is also applied.

In the literature Si_3N_4 compound is called stoichiometric silicon nitride. During deposition, eventough the target material we used is stoichiometric silicon nitride, the deposited film is not always Si_3N_4 but mainly an amorphous composition of silicon and nitrogen. Therefore we decided to anneal our samples in nitrogen atmosphere at 200°C for 1 week. This procedure helps nitrogen atoms make bonds with silicon and produce more stoichiometric silicon nitride molecules. Figure 4.8 is the high resolution scan of nitrogen and shows the comparison between the annealed and untreated sample. The blue curve in the graphs is the raw data after background removal. As explained, the curves under the blue curve explicitly show which compositions nitrogen atoms make. There is a significant difference in between the minor curves of Si_3N_4 for the annealed and untreated sample.

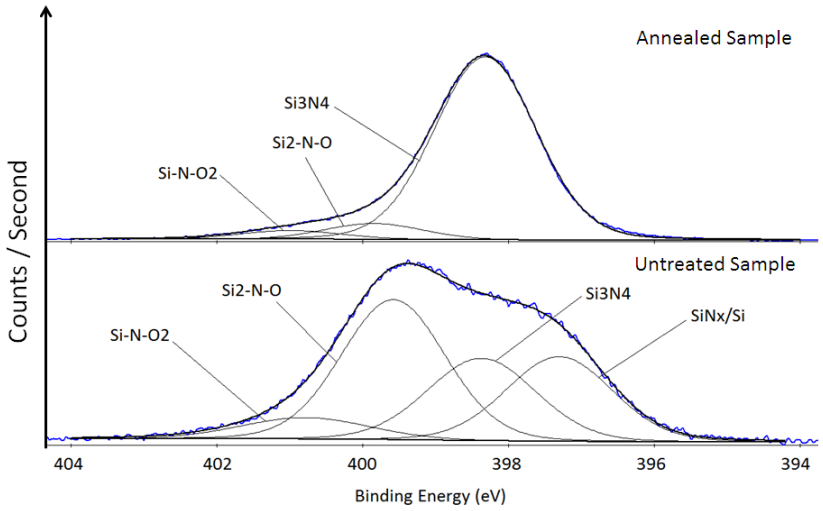


Figure 4.8. XPS high resolution scan of nitrogen in untreated and annealed silicon nitride sample.

The vertical axis corresponds to number of electron counts per second throughout the high resolution scans in arbitrary units. When one needs to quantitatively calculate the concentrations of elements in the sample, the areas under the curves must be calculated with the help of computer software XPSpeak. After finding areas, atomic

concentrations can be calculated via the formula:

$$C_i = \frac{\frac{I_i}{S_i}}{\sum \frac{I_i}{S_i}} \tag{4.3}$$

Where I_i's correspond to area under the curve of ith element, S_i's are the sensitivity factor for the ith element and C_i is the concentration of ith element. It should be noted that the sensitivity factors are chosen according to analyser mode. Our device works in Constant Analyzer Energy mode which is Hemispherical Sector Analyzer Detector. So the sensitivity factors are chosen according to this type of Analyzer mode in the NISTXPS database. The sensitivity factors are 0.27 for Si2p peak, 0.42 for N1s peak and 0.66 for O1s peak. The areas are in eVcount/s and valued as 32115.98 for Si2p peak, 47580.533 for N1s peak and 78653.876 for O1s peak. The high resolution scans for Oxygen and Silicon are given in Figure 4.9 and Figure 4.10, respectively.

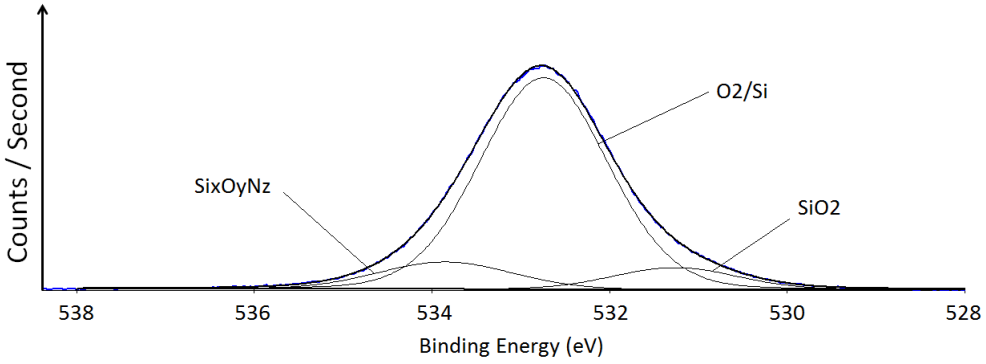


Figure 4.9. XPS high resolution scan of oxygen in annealed silicon nitride sample.

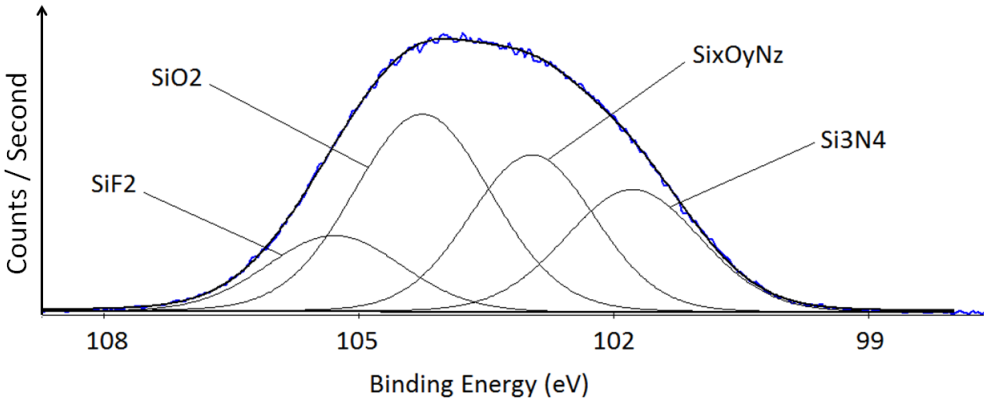


Figure 4.10. XPS high resolution scan of silicon in annealed silicon nitride sample.

As a result of this analysis, for a thin film of silicon nitride sputtered with 100W

RF power at 10mtorr argon pressure, annealed at 200°C for 1 week, the atomic concentration for Si is 33.85 per cent, for N is 33.92 per cent and for O 32.33 per cent. Finally, ratio of Si to N is found to be 0.998 whereas the ideal value is 0.75. It can be concluded that, even tough the ratio is close to the ideal value, it is still needed to deposit new samples with better ratio. For a purer silicon nitride sample, deposition should be performed under ultra high vacuum. This way the amount of oxygen in the samples will definitely be reduced. Also, the sputtering and annealing parameters can be fine tuned to obtain samples which are rich in stoichiometric silicon nitride. As it is explained in the introduction, the electrical and thermal properties of the materials are directly related to the chemical composition. Since for our purposes we need a material which is highly resistive, stoichiometric silicon nitride deposition should be optimized and taken carefully.

5. ATOMIC AND MAGNETIC FORCE MICROSCOPY

5.1. Atomic Force Microscopy

The Atomic Force Microscopy (AFM) [45] is a commonly used technique to generate surface topography of materials on nanoscale. It scans the surface of a sample with a sharp tip. This tip, which is few microns long and less than 10nm in diameter, is positioned at the end of a 100 to 200 μ long cantilever and the cantilever is mounted to an aperture which moves it over the sample. While the tip scans over the sample at a very close distance, the atomic interactions cause deflection of the cantilever. A detector measures these deflections via optical means and sends the data to a computer. After the data is processed by the computer, a surface map can be generated.

The atomic interaction between surface and tip is the interatomic forces. As it can be seen in Figure 5.1, the force depends on the distance between the tip and the sample. If this distance is tens to hundreds angstroms, then the force is attractive and this region is called van der Waals regime where the tip is run in non-contact mode. When the tip is held closer to sample, only few angstroms apart, then the force is repulsive and the region is called contact regime.

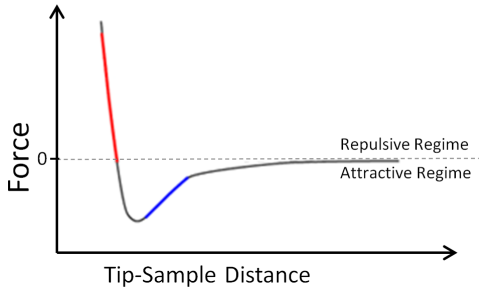


Figure 5.1. The atomic interaction forces in close proximity of a surface.

Most of the time the cantilever deflections are measured with a photo detector called quadrature detector. A laser beam is sent to the back of the cantilever, bounces back and falls on the photo detector. The bending of the cantilever shifts the position of the laser beam on quadrature detector. The detector measures these displacements and gives information about the vertical movements of the cantilever with nanometer

accuracy.

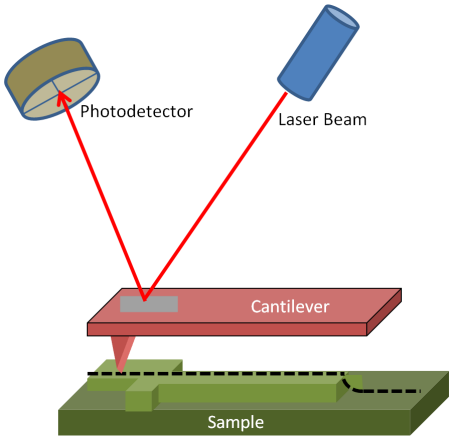


Figure 5.2. A basic schema representing the working principle of AFM.

Depending on which regime the AFM works, there are three different modes of operation. The first one is called contact mode. In this mode of operation there is a soft physical contact between the tip and the sample. As the tip comes closer to the surface of a sample, they first attract each other. While the separation decreases the repulsive force in between tip and the sample increases because the electron clouds of atoms begin to repel each other more and more. When the distance is couple of angstroms, the repulsive force wins over the attractive force and it is said that the atoms are in contact. In contact mode, the force between the tip and sample is given by Hooke's law:

$$F = -k \times D \tag{5.1}$$

where F is force (N), k is spring constant of cantilever and D is the deflection distance (m).

Since the van der Waals curve is highly steep in the contact regime, any force which attracts sample and tip to each other is balanced and canceled out. So, when the cantilever is pushed onto the sample, the cantilever bends rather than approaching more and more to the sample. If pushed hard, the sample or the tip is very likely to be deformed.

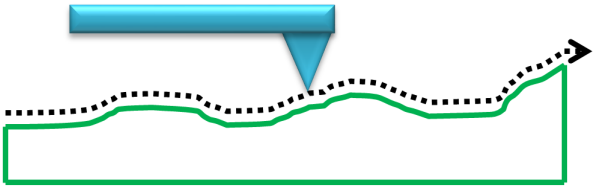


Figure 5.3. The motion of AFM tip when operating in contact mode.

There are two ways of operating AFM in contact regime. One of them is the constant height mode where the deflection of the cantilever is used directly to obtain the topographic information since the scanner height is fixed. Other is called constant force mode. In this mode, the force between the tip and the sample is constant by using a feedback circuit. By this way, the cantilever deflection is also kept constant and cantilever is moved up and down along vertical direction as it scans over the sample. The topographic data is read from scanner's motion along z direction.

The second mode of operation is called non-contact mode. In this mode, the cantilever is vibrated near its resonant frequency (typically from 100 to 400 kHz) with an amplitude of few tens to hundreds of angstroms. The changes in the resonant frequency is used to provide topography information. The resonant frequency of the cantilever, ω_0 , is given by

$$\omega_0 = \sqrt{\frac{k}{m_{eff}}} \tag{5.2}$$

where m_{eff} is the effective mass of the cantilever and k is the spring constant. When the cantilever comes closer to the surface, due to the forces exerted by the sample, resonant frequency of the cantilever changes accordingly and new frequency, ω, is expressed by:

$$\omega = c\sqrt{k - f'} \tag{5.3}$$

where f' is the derivative of the force normal to the surface [46].

The spring constant of a cantilever is proportional to the square of the resonant frequency and also to the force gradient experienced by the cantilever. Since the

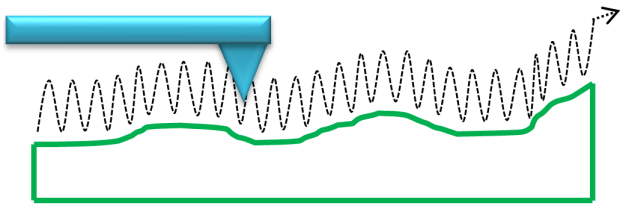


Figure 5.4. The motion of AFM tip when operating in tapping mode.

force gradient changes with the tip-to-sample separation (derivative of the force versus distance curve), the changes in the resonant frequency would in turn reflect information about the distance between tip and sample.

When the cantilever is oscillated near its resonant frequency, if the oscillation amplitude is as high as 100 to 200nm, then it is said that AFM is operated in tapping mode. In this mode, since the oscillation amplitude is high, when the tip comes close to sample the amplitude decreases. An electronic feedback system is again used to monitor these changes in oscillation amplitude and move the scanner along vertical direction to adjust the height of the tip and to keep oscillation amplitude constant. The equation which describes the amplitude of the cantilever oscillation with respect to oscillation frequency is given by a Lorentzian :

$$A = \frac{A_0 \frac{\omega_0}{\omega}}{\sqrt{1 + Q^2(\frac{\omega}{\omega_0} - \frac{\omega_0}{\omega})^2}} \tag{5.4}$$

where A is the oscillation amplitude, A_0 is the amplitude at resonant and Q is the quality factor which is always greater than 1 and can simply be expressed as:

$$Q \simeq \frac{\omega_0}{\omega} \tag{5.5}$$

Eventually, the topography image is produced by recording the height of cantilever as it scans over the sample surface.

Like most of the tools used in nanoscience, AFM systems consist of three basic components; the probe which scans the sample surface, an electronic system which

gathers electrical data from the detectors and a computer which visualizes electrical signals as graphs or images. Not only one can obtain a topography image but images regarding the oscillation amplitude, frequency and changes in forces can also be taken. Among them, one of the most important is the phase image. Phase imaging refers to recording the phase shift in the cantilever deflection due to force derivate as the tip scans the sample surface. The phase shift data can be obtained from oscillation frequency with the following equation:

$$\Theta = \arctan[\frac{\omega_0 \omega}{Q(\omega_0^2 - \omega^2)}] \tag{5.6}$$

5.2. Magnetic Force Microscopy

The most significant consequence of phase imaging property is the capability of measuring local changes in the orientations of the magnetic moments of sample, the so called Magnetic Force Microscopy(MFM) [47]. When a magnetic probe scans a magnetic surface in close proximity, the magnetic interaction between the tip and the sample will cause deflections of the cantilever. Since magnetic forces decay very quickly with the increasing distance, force derivative measurements can be used to obtain a magnetic image of the sample. The interaction force between the tip and sample is expressed as:

$$F \sim (m_{tip} \cdot \nabla) H_{sample} \tag{5.7}$$

where m_{tip} is the magnetic moment of the tip and H_{sample} is the stray field originated from the magnetic sample. This magnetic force will directly cause changes in the resonant frequency of the cantilever such that

$$\frac{\Delta\omega_0}{\omega_0} = -\frac{\nabla F}{2k} \tag{5.8}$$

Hence, a phase image reflects the variations of magnetic moments over a sample surface.

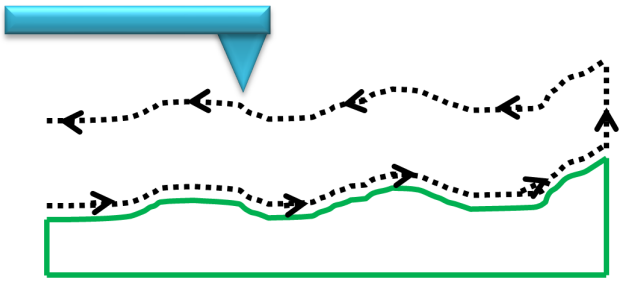


Figure 5.5. The motion of AFM tip when operating in lift mode.

In order to obtain a magnetic image, the AFM must be run in tapping mode. For a regular tapping mode scan of a magnetic sample, both the magnetic and electrostatic forces contribute to the deviations in the oscillation frequency. That's why, MFM runs in lift mode. When the tip scans a surface, it always scans straight lines along the sample and each line is scanned twice, both forward and backward. In the lift mode, first the tip scans a line in regular tapping mode and when scanning backwards over the same line, the tip is lifted above around 40nm in order to avoid contributions from electrostatic forces and allow the tip to be deflected only by the magnetic forces. Finally, the resulting backward phase image reveals magnetic distribution of the sample.

5.3. AFM Artifacts

As all measurement instrumentation used by scientists for research and quality control generates results that may have artifacts, Atomic/Magnetic Force Microscopy may also have some common artifacts which results in misinterpretation of the images taken. Here common artifacts are stated, categorized by the source of the artifact. AFM/MFM artifacts are due to probe, scanner and vibrations (environmental effects).

5.3.1. Probe Artifacts

The resulting images after a scan not only show the features of the sample surface but also affected by the tip geometry. As illustrated in the above examples, the dimensions of the probe must always be chosen according to the size of the features on the surface being scanned. Most of the time, the size of the tip should be smaller than

the structures on the surface. Otherwise, features on the surface may appear larger or smaller than they really are. In Figure 5.6a , the object will seem broader than it really is because of the side of tip. In Figure 5.6b, since the tip cannot scan the sides of the hole, a rectangular shaped hole will look like a triangle. On the other hand, if the tip gets broken anyhow, one may observe unexpected strange shapes on a sample surface. Moreover, the tip must ideally be perpendicular to the surface. If not, asymmetrical features may be observed.

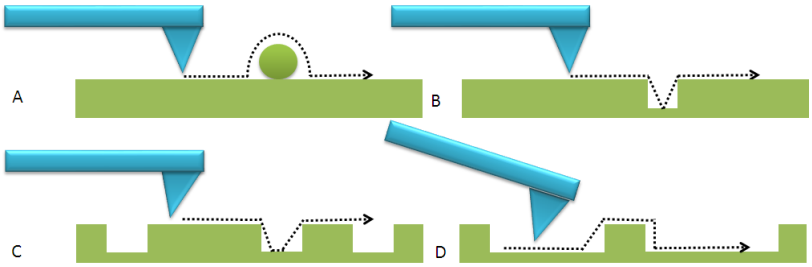


Figure 5.6. Examples of artifacts due to the AFM probe.

5.3.2. Scanner Artifacts

Typically, the probe tip is driven by scanners made of piezoelectric materials. These materials are capable of moving the tip with very small distance by application of small voltages. Even tough they are so sensitive, they may cause image artifacts due to heating, or a nonlinear or hysteretic motion if they are not calibrated properly. The probe scanner must be correctly calibrated in X-Y directions to obtain accurate images. Any error or nonlinearity would cause the features appear with wrong dimensions as illustrated in the figures.

Most of the time, piezoelectric scanners move the tip above the sample and cause bowshaped image due to the curved motion of the tip(Figure 5.8). These kinds of artifacts are very likely to be observed in the images and can easily be fixed with post-processing via a computer-software.

Also, piezoelectric materials are sensitive to temperature changes such that after running the device for a while the piezo may be heated and result in overbending while scanning. This kind of artifact is called thermal drift and can be recognized if some

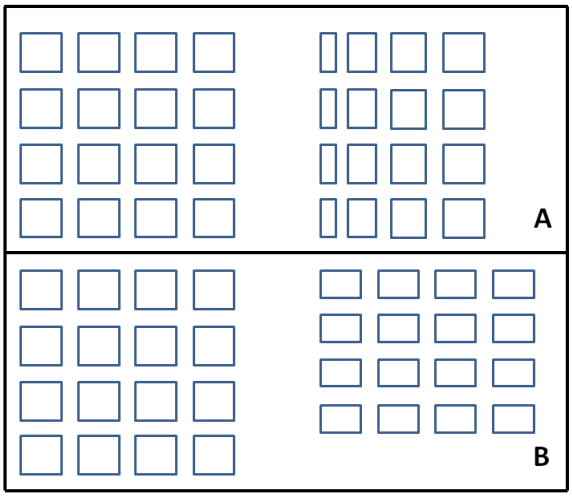


Figure 5.7. Examples of artifacts due to the AFM scanner

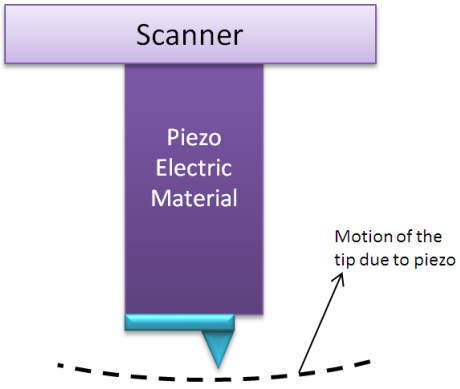


Figure 5.8. Examples of artifacts due to the piezoelectric scanner.

part of the image has inclination more than the rest of the image. To reduce this effect, a scan may be repeated or the piezo may be run until it is thermally stabilized.

5.3.3. Vibrations

Environmental effects such as the vibrations in the floor of the building where AFM is located or the sound waves around the experiment area can cause artifacts in the scan. Since the scan is performed in atomic scale, this kind of small errors influence the signals as noise. AFM device should be placed inside an acoustic isolation box on a vibration isolation table to reduce these noises and obtain clear signals.

5.4. Experiments

Atomic and Magnetic Force Microscopy measurements are done with Bruker Dimension Edge AFM system. The details of the system and the operation procedure can be found in Appendix D.

5.4.1. CoNi/Pd AFM/MFM Measurements

In this section magnetic force microscopy measurements on CoNi/Pd films are reported. In order to examine whether the fabricated CoNi/Pd films are magnetic or not, three different magnetization states are examined. These states are AC demagnetized state, saturated and thermally demagnetized state. It must be reminded that CoNi/Pd films have perpendicular magnetic anisotropy. That's why the film is saturated in perpendicular magnetic field of 0.5 Tesla in an electromagnet. AC demagnetization is done by applying perpendicular magnetic field in opposite directions successively with decreasing amplitude. For MFM measurements, we used Bruker MESP low moment tip. The tip is n doped Si, coated with Co/Cr whereas the front side is magnetic and the back side is reflective. The resonant frequency of the tip is expected to be in between 60-100 kHz.

Figure 5.9 is AC demagnetized state magnetic images of the bow tie-shaped samples. A and B are image of the triangular region, C is along microwire and D is triangular region with nanosized wire. As it can be seen, perpendicular magnetic domains of opposite directions are distributed randomly, forming a demagnetized state as a whole. While taking these images, the oscillating frequency was 72.40 kHz, lift height is 40 nm, amplitude setpoint is 3687.16 mV, resolution is 256×256 in A and 512×512 in B,C,D, scan rate is 1 Hz (only one line is scanned in one second) in A,B,C and 2 Hz in D. The area of the scan and the color scale are given next to each image.

Figure 5.10 is saturated state magnetic image of CoNi/Pd samples. As visualized in the images, the magnetization of the sample are all directed in the same direction that the magnetic tip does not detect any change while scanning. Remember that

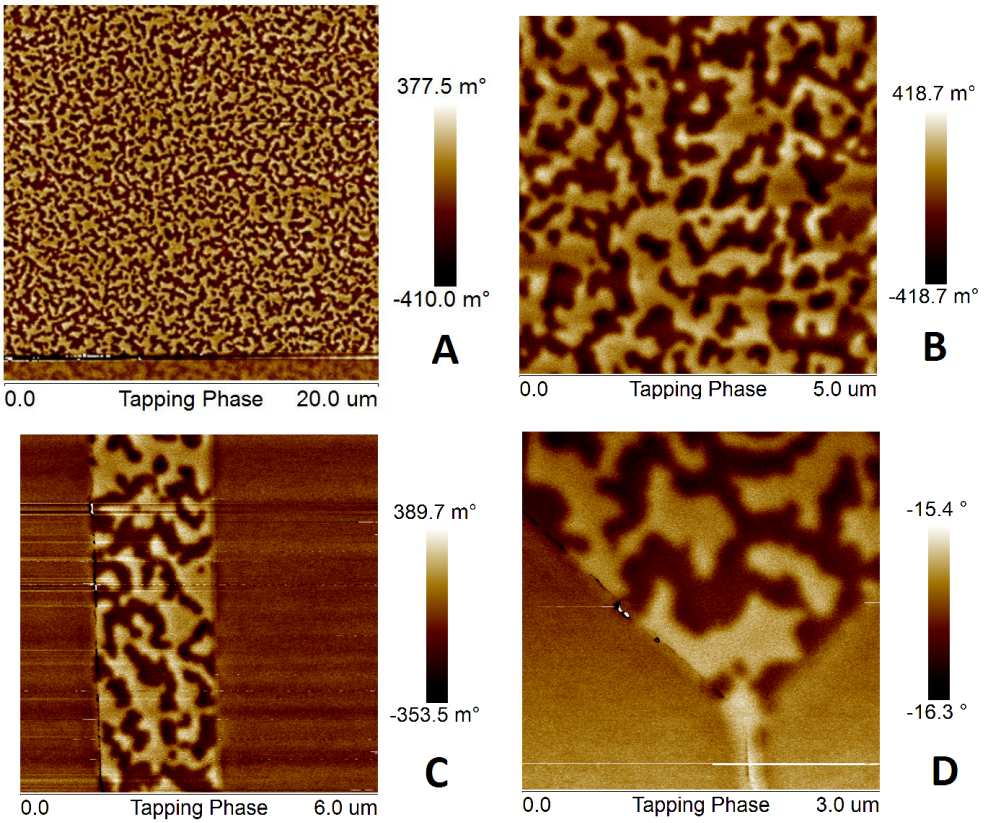


Figure 5.9. MFM image of CoNi/Pd magnetic sample in AC demagnetized state.

the magnetic force microscopy detects force gradient.While taking these images, the oscillating frequency was 69.74 kHz, lift height is 40 nm, amplitude setpoint is 3693.24 mV, resolution is 512×512, scan rate is 0.5 Hz. The area of the scan and the color scale are given next to each image.

Figure 5.11 presents thermally demagnetized state of CoNi/Pd films. When the magnetic sample is heated close to its Curie temperature (175°C), the material demagnetizes, there is no net magnetization. In these MFM images, oscillation frequency is 73.621 kHz, lift height is 40 nm, amplitude setpoint is 3538.33 mV, resolution is 512×512, scan rate is 0.6 Hz in A and 0.3 Hz in B.The area of the scan and the color scale are given next to each image.

It is observed that the domain sizes in AC demagnetized and thermally demagnetized state is different. The domain sizes in AC demagnetized state is directly dictated by how the demagnetization is done with the application of magnetic field. While ap-

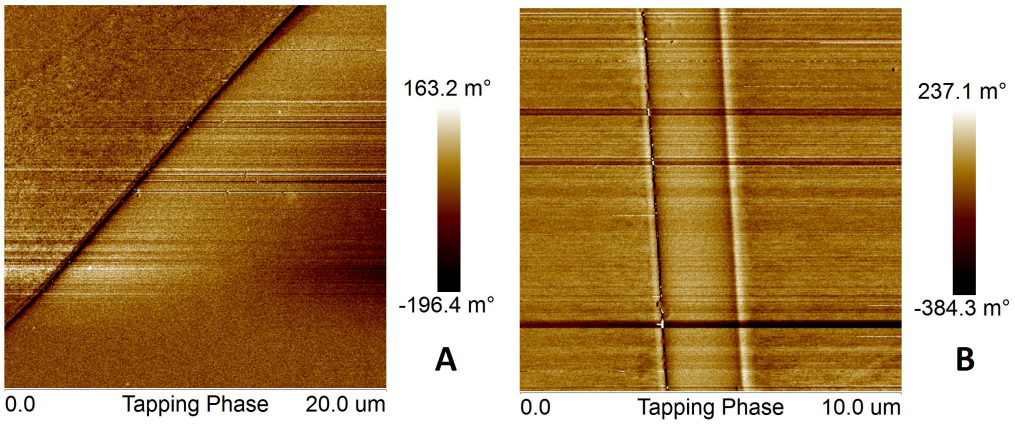


Figure 5.10. MFM image of CoNi/Pd magnetic sample in perpendicularly saturated state.

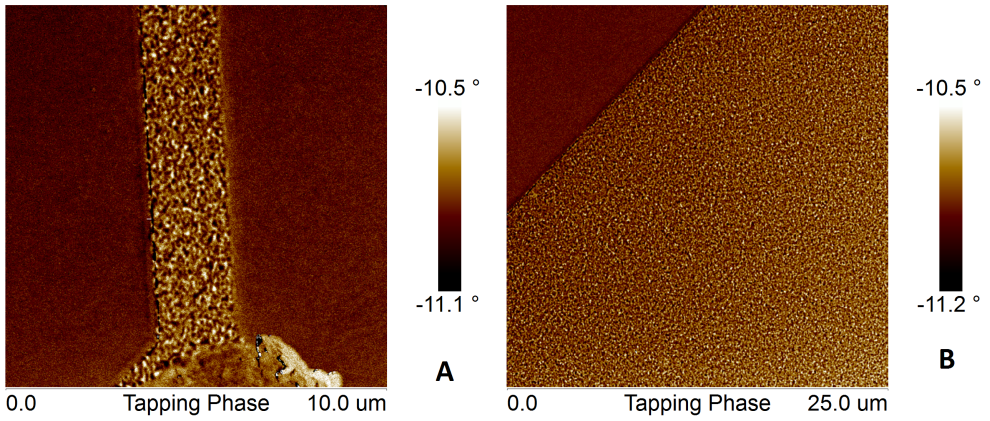


Figure 5.11. MFM image of CoNi/Pd magnetic sample in thermally demagnetized state.

plying magnetic field, at each step of successive applications, the amplitude of the field is decreased. The greater the decrements, the greater the domain walls are formed.On the other hand, since this procedure is done at room temperature, magnetic anisotropy energy is high during domain nucleation. So that magnetic moments are very likely to align themselves in the same direction which in turn forces nucleation of larger domains. Whereas in the thermally demagnetized state, since the material is brought up to its Curie temperature and loses its magnetic anisotropy, the magnetic moments are likely to be randomly aligned. That's why magnetic domain sizes are much less in the latter case compared to the former one. Since the domain sizes are important for magnetic memory application (magnetic domain size defines the bit size), it is important for us to examine domain nucleation and magnetization reversal mechanisms at room tem-

perature and close to Curie temperature. Because our magnetic memory device works at room temperature but magnetization switching occurs at elevated temperatures, the experiments help to define optimum bit size which is stable at room temperature and which allows efficient magnetization reversal at higher temperatures.

In Figure 5.12, topography of the magnetic samples are presented. These AFM images are taken at the same time with AC demagnetized state magnetic images. It is stated above that, in AFM a line on the surface is scanned twice, forward and backward. When working in lift mode, the tip is lifted above the surface during the backward scan. So during a regular scan, magnetic images (phase image) can be obtained at the same with the topography images. In these AFM images the oscillation frequency is 72.40 kHz, amplitude setpoint is 3687.16 mV, resolution is 512×512 in A,B,C and 256×256 in D and scan rate is 1 Hz. In Figure 5.11, A and B show 2D and 3D topography of the microwire, C shows nanowire and triangular region and D is a full can over magnetic surface. The roughness of CoNi/pd surface is calculated from D to be 0.8nm.

5.4.2. Si_3N_4 AFM Measurements

Atomic Force Microscopy measurements have been carried out on fabricated Si_3N_4 thin films to obtain topography images and to calculate surface roughness. Topography image is shown in Figure 5.13. The tip used in this scan is Bruker Tespa n doped Si with Aluminium coating. While taking topography image, the oscillating frequency was 349.275 kHz, amplitude setpoint is 4032.60 mV, resolution is 512×512 and scan rate is 1 Hz. In this sample, root mean square(rms) roughness is calculated to be 0.8 nm.

In our device structure, silicon nitride is an intermediate layer between two magnetic layers where magnetization reversal occurs due to stray fields coming from the adjacent layers. Since this stray field is relatively weak, intermediate silicon nitride layer must not be so thick such that it will allow the field from one magnetic layer to reach the adjacent magnetic layer. At this point a dilemma occurs in the case of the thickness of the spacer layer. If this spacer layer is so thin, the stray fields

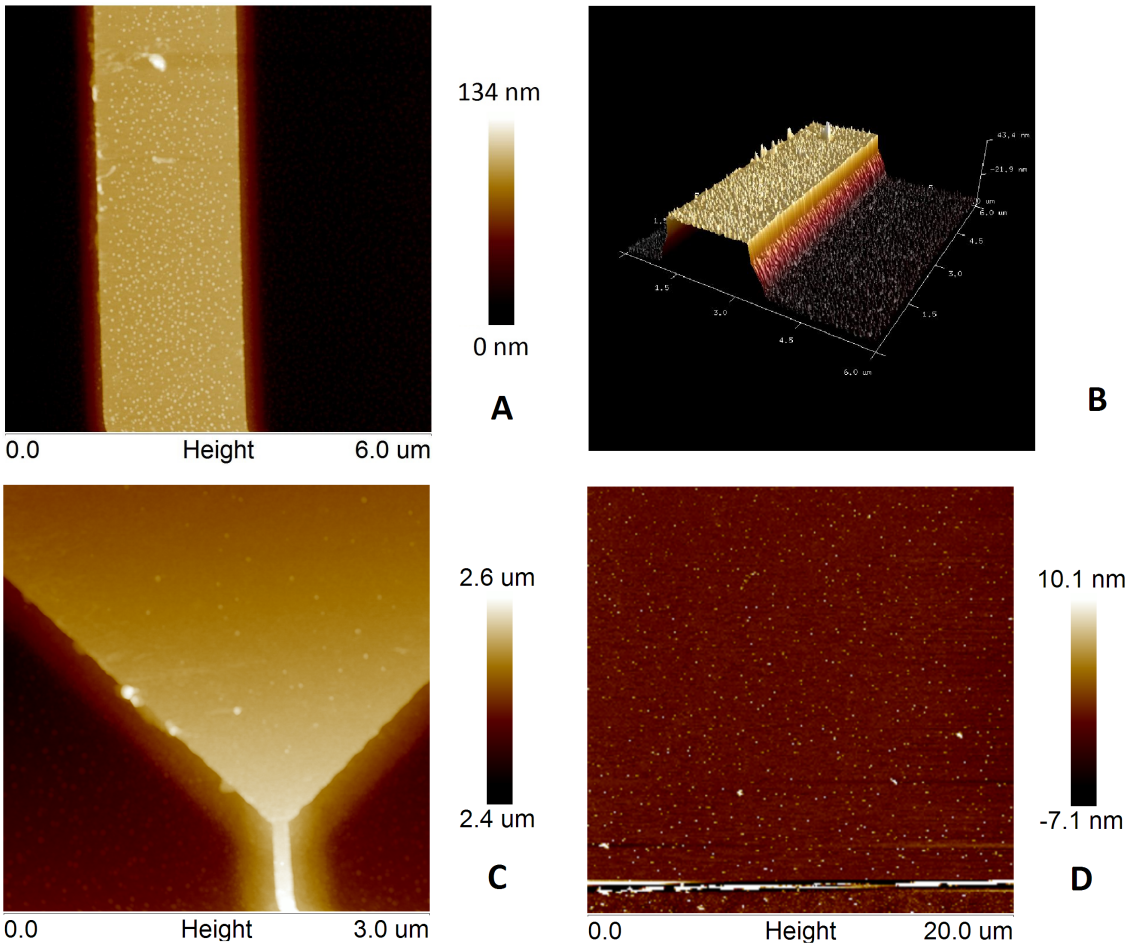


Figure 5.12. Topography images of CoNi/Pd magnetic sample.

of adjacent layers will effect each other and force themselves to align parallel. This will cause loss of information even at room temperatures where the magnetic domains are indeed expected to be stable for relatively long periods of time. That's why the optimum thickness must be figured out for the best efficiency of the device. On the other hand, if the silicon nitride layer, which separates two magnetic layers have high roughness, an unwanted situation, orange-peel coupling may occur [48]. In this phenomena magnetic dipoles are generated at the interfaces, especially at the very rough surfaces with bumps and pits. These dipoles favour parallel alignment independent of the magnetization direction of the whole magnetic layer. This situation would in turn lead to uncontrolled magnetization reversal, malfunction of the device and the loss of information. For those reasons, the roughness of the thin films must be engineered so well that very fine surfaces are needed to be fabricated.

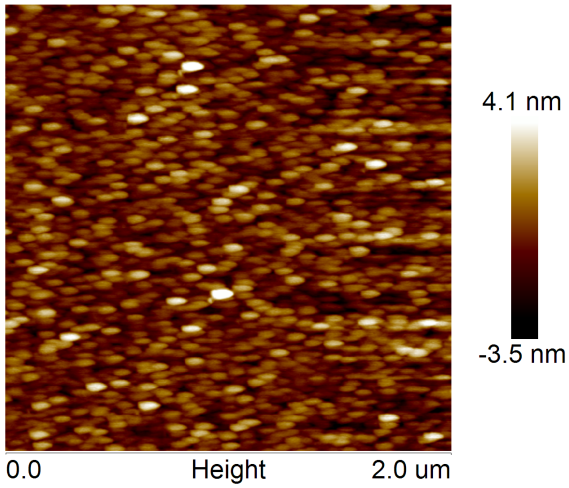


Figure 5.13. Topography image of silicon nitride sample.

6. CONCLUSIONS AND FUTURE WORK

In this thesis, two different spin-based three dimensional memory systems have been introduced. The first system, explained in Chapter 2, was proposed as an idea promising to have capabilities of the third dimension in a magnetic memory. Even though the structure has not been fabricated and tested, all the physical phenomena and methods utilized in this system have been well-documented in literature. The methods such as inverse Faraday Effect [17], spin injection [24], domain wall motion [25, 49] or spin-polarized vertical cavity surface emitting lasers [21] are all well studied theoretically and experimentally. In pursuit of realization of such a device the first step would be to fabricate a prototype including only one VCSEL to exhibit vertical data transfer. This prototype must be engineered to optimize the dimensions of the device and its electrical and magnetic characteristics. The magnetic materials used in this device are significant in different aspects. Since this device operates by applying current, electrical characteristics of the used materials are severely important. The amplitude of the current that must be applied to the system for domain wall motion depends on the material and it is reported that the current densities on the order of $10^7 \mathrm{A/cm}^2$ can trigger domain wall motion on ferromagnetic nanowires [49]. Value of the applied current must be optimized very well such that malfunctioning of the device, such as overheating due to Joule heating, uncontrolled magnetization reversal, erroneous domain wall motion, is prevented. On the other hand the magnetic material should have perpendicular magnetic anisotropy, plus, the energy levels in the material should allow spin-flip under excitation of circularly polarized light. Alloys, multilayers and heterostructures of rare-earth transition metals (such as GdFeCo, TbCo DyCo, Tb/Co, Ho/Co) are shown to exhibit those necessary properties [50]. It has been shown that for optical magnetization reversal femtosecond circularly polarized laser pulses with a wavelength of 800nm is satisfactory [18]. A typical spin-VCSEL with Mn doped GaAs active region and (Al)GaAs mirrors has lasing wavelength around 950nm which makes it a strong candidate to be the light source for optical magnetization reversal but still requires further investigations [21]. The disadvantage of a spin-VCSEL is that for efficient spin-injection, they are operated at around 90K [51, 21]. This

temperature range is unpractical for magnetic recording devices since they work around room temperature. The most promising candidates for operation at room temperature are reported to be diluted magnetic alloys such as Ga-X-N and Zn-X-O (where X is Cr,Mn,Fe,Co, Ni) [52] and half-metallic ferromagnets such as Fe_3Si, Co_2MnGa and Co_2MnSi [53]. Finally, it is a key point for the device to be scalable down to nanometers. In the mentioned literature, most of the experiments are done on few nanometer thin films which guarantee this prototype structure to be a nano sized object. After working on the prototype, a system with many VCSELs and multiple layers can be produced in an array and a truly three dimensional magnetic memory structure can be obtained.

The second part of the thesis concerning magnetic page memory is a three year long project. The first one and a half year of the project included fabrication and characterization of the materials constituting the device. The experiments regarding the fabrication and characterization were explained in Chapters 3, 4 and 5. The materials were fabricated with sputter deposition. To know the thickness of the thin films calibration procedure has been run to calibrate the sputter deposition rate of Al, Cu, Si_3N_4 and CoNi/Pd targets. A photomask was designed and photolithography was done to pattern calibration gratings on Si wafers. The thicknesses of depositions were measured with stylus profiler. After deposition, electrical, magnetic and thermal characterizations of the materials were done. Si_3N_4 thin film was required to have high electrical and thermal resistivity at room temperature and found to possess electrical resistivity on the order of $10^{12}\Omega$cm and thermal conductivity of 3.2 W/mK . For CoNi/Pd magnetic layer, thermal conductivity was found to be 20W/mK and electrical resistivity was 30 $\mu\Omega$cm at room temperature. These characteristics are severely important, since our device is magnetic, works with current application and makes use of heat during operation. It has been concluded that thermal and electric conductivities of fabricated thin films were appropriate for the right operation of the device. Stoichiometric analyses were done to investigate the chemical state of the deposited materials since it affects electrical or thermal properties. The ideal ratio of Si to N is 0.75 for stoichiometric silicon nitride. It turned out that fabricated thin films have Si to N ratio of 0.99. However this did not cause any problem since the thin films met the electrical and thermal resistivity requirements. Atomic force microscopy was used

to examine the surface topography of the materials and the rms surface roughness of the thin films was found to be 0.8nm. This sets the limit for minimum thickness of the nitride spacer layer and further reduction of surface roughness may help reduce potential magnetic coupling between layers [48]. Distribution of magnetic domains in demagnetized and saturated state was visualized with magnetic force microscopy. The nucleation, form and stability of magnetic domains are also significantly important for our study since the magnetic domains define the bit size, the basic unit where the information is recorded. It is concluded that CoNi/Pd multilayers exhibit high perpendicular magnetic anisotropy at room temperature such that relatively large magnetic domains are likely to nucleate. When the magnetic sample was heated up to its Curie temperature(175°C) and cooled down to room temperature, the magnetic moments tended to create a demagnetized state via random alignment with minimum domain size of 40nm, allowing a theoretical areal density of 500Gb per inch square.

After the fabrications of the samples are finished, writing experiments will be carried out during the second half of the project. The aim will be to observe spin-torque induced domain wall motion along a ferromagnetic nanowire by spin-polarized current and vertical data transfer via heat assistance as explained in the first chapter. The first step will be to nucleate a single magnetic domain with the help of a MFM tip. By bringing an High-Moment MFM tip close to (few nanometers distance) magnetic nanowire, the stray field coming from the magnetic tip will orient the magnetic moments in the material during the application of a heating current pulse that lowers the local coercivity. Then the second step will be to apply electrical current along the nanowires reaching current densities above the critical value for domain transfer which is on the order of $10^7 A/cm^2$ and observe that electrons become spin-polarized while they flow through the ferromagnetic wire and apply spin-torque on the domain walls. This would result unpinning the domain wall from one site and moving it to another nucleation site. A third step is to work on a double constriction where the magnetic layers are separated with a spacer layer. By applying current on a wire, the material will be heated close to its Curie temperature, around 100°C and so the stray field coming from the adjacent magnetic layer will nucleate the same magnetic domain. The observations of the magnetic domains will all be visualized with magnetic force microscopy. Moreover,

most of the experiments will be done in a home-made experimental setup which will be implemented in an MFM device. The goal of this project is to demonstrate a three dimensional magnetic memory system which operates properly to save data and allows the flow of data in both horizontal and vertical directions inside a three dimensional volume. The future of the project concerns the experiments which will be done on the samples that were fabricated and characterized in this thesis.

Comparing the two different systems, magnetic page memory is one step ahead in the case of realization of the devices. First of all, the materials that are used are known to be Si_3N_4 and CoNi/Pd for the magnetic page system whereas for the opto-magnetic system materials mentioned in the first paragraph are needed to be tested for device application. The thin films are fabricated, characterized and ready to run experiments on them for magnetic page system. Also, the experiments to demonstrate the operation of magnetic page memory is already set up; the goals, expectations and possible difficulties are identified clearly. We only have rough estimations on these issues in the case of opto-magnetic memory system. It must be underlined that for both systems, it is very difficult to fabricate such complex three dimensional structures especially in the case of fine details, such as the interfaces, hexagonal constrictions etc. For opto-magnetic memory, it is especially difficult to obtain efficient spin-injection from a ferromagnetic metal to a semiconductor as it is well discussed in the literature [21,51-53]. As the number of layers and the number of bits along a nanowire increase, it gets harder for the total structure to be stable and work properly. The major trade-off for both structures is that if a complete device is ever produced, half of the bits in the structure must be buffer. Even though the capacity advantage of third dimension is utilized, half of the bits in the structure is used for functioning of the device and not used for storing information. Both systems are advantageous in the case of speed of reading and writing since they operate by applying current pulses with durations on the order of nanoseconds. As it is reported in [18], optical magnetization reversal can be achieved with femtosecond laser pulses; much faster than most of the conventional methods. However, it is easier and quicker for the opto-magnetic memory system to reach information in the intermediate layers of the multilayer system since there is only one multilayer stack compared to magnetic page memory system which has two separate

stacks for storage and buffer. The former system is power efficient compared to other devices because it is not needed to apply magnetic fields for magnetization reversal and not needed to apply current pulses for heating, indeed heating is undesirable in the system. On the contrary, heat assistance for vertical data flow in magnetic page system makes writing operation simpler than it is in opto-magnetic system but the parameters must be very well defined such that the system must be stable at room temperature, and must allow magnetization reversal at an elevated temperature while preventing thermal demagnetization.

Throughout this thesis, the aims stated in the introduction were achieved. Three dimensional spin-based memory systems were introduced and one system was studied experimentally. Even though the systems were not finalized as complete, functioning structures, preliminary discussions and experiments were carried out in order to define the conditions upon which the systems can be built. A hypothetical idea was introduced and fabrication and characterization experiments were done; significant properties and major difficulties were pointed out. Further experimental study of mentioned systems can be successfully pursued based on the fundamentals highlighted in this thesis leading to an operational device.

APPENDIX A: SPUTTER SYSTEM

A.1. Sputter system

All the thin film deposition experiments are done at Vaksis PVD Handy Sputter System in the house. This system consists of a vacuum chamber produced by Vaksis, Pfeiffer DCU-610 Turbo Vacuum Pump, Kurt J.Lesker 937A Pressure Gauge Controller, Vaksis FC101A Gas Flow Controller, Advanced Energy MDX-1K DC Power Supply, Advanced Energy CESAR RF Power Generator and two magnetron heads.

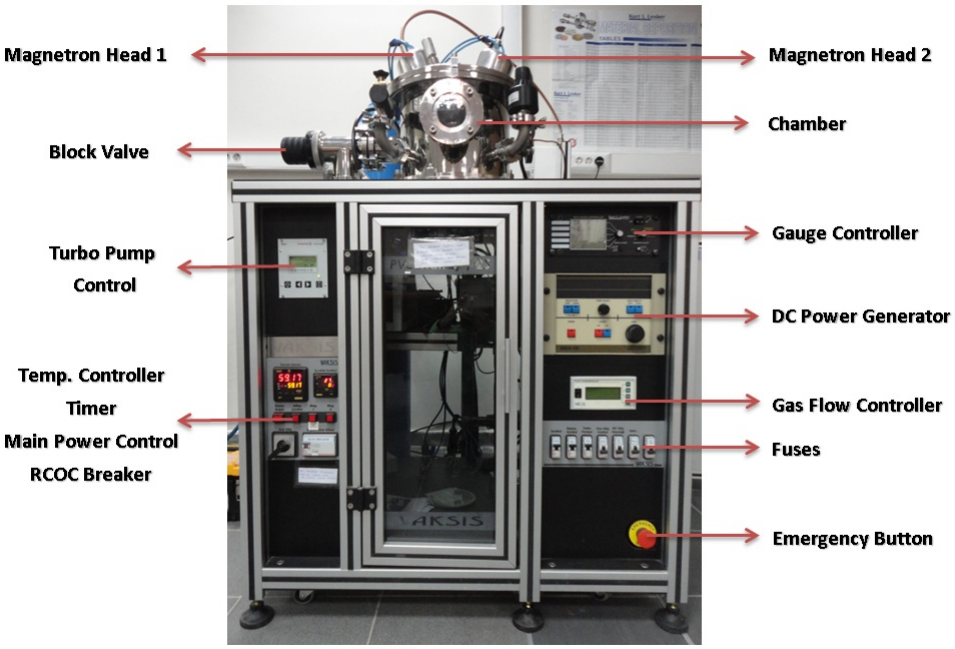


Figure A.1. Vaksis Sputter System in our lab.

A.2. Operation Manual

- If the system is turned off and you want turn on, start with step 1.
- If the system is turned on and vacuum is ready, then jump to step 2 to start sputtering.
- If the sputtering is finished and you want to turn off the system, jump to step 3
- Don't forget to record every operation you do in the sputter system logsheet.

A.2.1. Step 1 turning the system on

- At that moment, the system must be turned off and the necessary target and substrate must be placed in the system beforehand.
- If not, jump to step 3 for placing the target and substrate
- If so, follow on the steps below.
- Be sure that the chamber door is closed and clamps are tightened at 120 degree positions.
- Switch on the main power control and RCOC breaker.
- Switch on the control fuse.
- Switch on the pressure control fuse and the gauge controller.
- At this point, the system (chamber and turbo pump) must be at atmospheric pressure.(around 7×10^2Torr).
- The vent valve must be open.
- The block valve must already be open. If not, open it.
- Switch on the turbo pump fuse. Turbo pump starts to work and initialize for pumping.
- Press the right most button on turbo pump control to start pumping and observe the loud noise that the diaphragm pump gives. After a while diaphragm pump stops and turbo pump starts working quietly.
- If you cant see the actual rotation speed on led display, move through the menu by pressing left and right buttons and go to 309
- Now, you have to wait until the pressure reaches the value needed for sputtering. Conventional value is around 4×10^{-5} Torr, which is OK. But, it is much better to wait until the pressure is on the order of 10^{-6} Torr which may take some time.
- To read the pressure values below 10^{-3} Torr, you have to activate the cold cathode on the gauge controller. Be aware that pressures above 10^{-3} Torr harms the cold cathode, so then it should be turned off.
- After obtaining the vacuum inside the chamber, the system is ready for sputtering. You can move on with step 2.

A.2.2. Step 2 Sputtering Procedure

- At this point, vacuum in the chamber must be ready. The necessary target and substrate must be placed in the system beforehand.
- If not, apply the step 3 to turn off the system and place the target and substrate. If so, follow on.
- Optional: If the substrate is needed to be heated, set the temperature by pressing SET button for two seconds on the heater control. Heating will start when you switch the heater fuse on. It would take some time to heat. (Max temperature is 250°C)
- Turn off the cold cathode on gauge control display(In case, rapid pressure increase harms it).
- Close the block valve and open it a little bit (In case, rapid gas flow into the chamber harms the turbo pump).
- Now, open the valves on Argon tube. Do not expect to see the gas flowing since the flow controller is off.
- Switch on the gas flow control fuse and turn on the flow controller.
- By pressing the F1 button on the flow controller, increase the gas flow rate up to 5sccm.
- Now, Argon starts to enter into the chamber, you must see that the pressure in the chamber increases.
- By turning the block valve, you have to adjust the pressure according to the value at which you want to do sputtering.
- Open the water valve (it is on the wall behind the machine).
- Now, you have to decide whether you use DC or RF which depends on the target.
- Plug in the appropriate power cable (DC or RF) to the gun which you will use.
- For DC sputtering follow on with 2.1, for RF sputtering move to step 2.2.

A.2.2.1. DC Sputtering.

- Switch on the DC power supply fuse and press the power button.

- Regulate the power value on DC Power supply by pressing the SET button.
- Choose which magnetron head to use. (mag1 or mag2 on the main control)
- Start substrate spinner.
- Adjust the duration that you want to do sputtering on the time gauge and start it.
- Now everything is ready for sputtering.
- If the INTERLOK light flashes on the power supply, press the OFF button to stop flashing.
- If it lights continuously, this means everything is OK for sputtering. Now push the ON button to begin sputtering.
- If it still flashes, that means there is a problem that you have to solve before sputtering such as that water cooling is not working, time gauge is not set, magnetron head is not chosen or chamber door is not closed properly.
- Condition your sputter with shutter closed at least for 5 minutes to clean off any potential contamination on the surface of the target.
- Open the shutter. Restart the timer, Now particles start to fall on the substrate.
- Now you have to wait until the time gauge is off. Then the power supply will stop automatically.
- Do not leave the system running by itself since occasionally the plasma would fail on its own and would require your interference. In cases like power failures or emergencies (hearing bad noises from turbo pump, running out of Argon gas, the cooling water fails etc.). Use the red emergency button stop the system immediately.

A.2.2.2. RF Sputtering.

- Switch on the RF Power Supply Fuse, Turn RF Power Generator on.
- Choose which magnetron head to use. (mag1 or mag2 on the main control)
- Start substrate spinner.
- Adjust the duration that you want to do sputtering on the time gauge and start it.

- Now everything is ready for sputtering.
- Regulate W_f value by slowly turning the knob. (In case rapid power increase cracks the target)
- Push the ON button to start sputtering. RF Power supply works loudly to adjust the output capacitance to do impedance matching and to minimize reflected power W_r . This value should be zero at the end of the procedure then the generator works quietly. If not, push the manual button and adjust C_r and C_L until you observe zero reflected power. You can switch back to auto mode.
- Now you must observe the plasma inside the chamber.
- Condition your sputter with shutter closed at least for 5 minutes to clean off any potential contamination on the surface of the target.
- Open the shutter. Restart the timer, now particles start to fall on the substrate.
- Since the system does not stop automatically, you have to stop the RF Power generator manually after enough time has elapsed.
- Do not leave the system running by itself since occasionally the plasma would fail on its own and would require your interference. In cases like power failures or emergencies (hearing bad noises from turbo pump, running out of Argon gas, the cooling water fails etc.). Use the red emergency button stop the system immediately.

A.2.3. Step 3 Turning the system off

A.2.3.1. Venting the system.

- Turn DC (or RF) Power Generator, Cold cathode, substrate spinner off.
- By pressing F2 button on the flow controller, decrease the gas flow rate down to zero.
- off the flow controller and close the valves on Argon tube.
- Open the block valve slowly.
- Stop the turbo pump by pressing the right most button on it.
- Now, you have to wait until the turbo pump automatically stops and vents by itself. You will observe that rotation speed gradually goes down to zero.

- Loosen the clamps of the chamber door because it would be harder after vacuum breaking.
- By this time, we leave the water valve open to cool system. After a while (approximately 5 minutes) you can close it.
- Now you can open the chamber and take your substrate.

A.2.3.2. Opening the chamber.

- First of all, you have to vent the system to atmospheric pressure.
- Be aware that block valve is open completely. (If not, open it slowly)
- Open the vacuum breaking valve slowly (in case rapid pressure increase harms the turbo pump).
- Now you can open the chamber door by using the pendulum system.
- Since inside of the chamber is exposed to outside, it is very likely that oxygen,vapour or dirt can go inside the chamber and stick to walls. For that reason, apply this procedure as quick as possible and do never touch any piece with bare hands. Wear appropriate blue nitrile gloves, bonnet, jacket and safety glasses and use clean equipment.
- Pick up the sample.
- At that point, you may need to clean the system.
- After that place a new wafer and the necessary target that will be needed for the next sputtering.
- At last, use pendulum system again to close the chamber door.
- Depending on the next operation, leave the system turned off or apply the procedures in step1 to turn the system on and leave it in vacuum.

A.2.3.3. Cleaning Procedure.

- First of all, you should never touch any piece inside the chamber with bare hands. All the equipment that you use should be clean.
- Use clean equipment to dismount magnetron heads, substrate spinner and the

inner wall of the chamber.

- You would observe that, those pieces are also sputtered unintentionally. To rub them you need to use sand blaster.
- After that, you have to clean every piece before mounting them.
- Clean means that the pieces must be immersed for 15 minutes in ultrasonic bath (without heating!) first in acetone and then isopropanol.
- Then you can mount them back in the chamber.

A.2.3.4. Target Change.

- First of all, wear appropriate clothings to work inside the chamber.
- Always use clean equipment.
- First, dismount the shutters.
- Dismount the front covers of the magnetron head.
- Dismount the front plate which holds the target.
- Take the target and replace it with the one you need for the next sputtering.
- Cover the used target with aluminium foil and put it in a clean bag.
- There are two different front plates for the magnetron head, a thin one and a thick one.
- If your target is thick, use the thick front plate.
- If your target is thin, use the thin front plate.
- If your target is very thin, use the thin front plate and also you may need to use a back plate.
- Then you can mount front plate and front cover back. At this point, you have to check with a multimeter whether there is short in between the front cover and the target (or front plate). If there is, you have to dismount them and mount them back carefully. The front cover has four screws on the sides, you should tighten them equally.

APPENDIX B: PHOTOLITHOGRAPHY

To fabricate patterns on silicon wafer, photolithography is done in the clean-room facility at Sabancı University Nanotechnology Research and Applicaion Center. Procedure and receipt for our lift-off process is explained as following.

- Enter the (yellow light) photolithography room.
- At first, turn the hot plate on, set the temperature (100°C) for soft-baking.
- Check the gas valves and displays on the wall behind Midas mask aligner. They must work correctly.
- Turn on the Midas Mask Aligner. Turn and release the red knob, then switch on. Turn on the controller(at the bottom). Main switch up. Green button (Push to ignite, push and hold to let it run).
- Turn the computer on (Second windows OS).
- Clean your mask with isopropanol and then with DI water.
- Clean your wafer, first with acetone and then with isopropanol.
- Spinner. Program it for spin rate and duration depending on your PR. First is spreading(500 rpm for few seconds). Second is thickness setting (4000rpm, 30 seconds). Third is to stop spinning(0 rpm).
- Put the plastic cover into spinner.
- Put wafer into spinner stage and turn the vacuum on.
- As you start spinner, drop Photoresist immediately (few drops). (AZ5214E positive photoresist)
- After spinning, soft baking at 100C for 1 minute to remove solvent.
- Exposure to light.
- Open the mask aligner software, log in.
- Initialize.
- Check the white line alignment of wafer holder stage.
- Measure the thickness of your mask (2.21microns).
- Place your mask to mask holder and turn on the vacuum by pressing the green button on midas mask aligner. Parameters are 25mW/cm^2 for intensity. 2 sec is

mostly enough (maybe 2.4sec). Enter mask, sample and resist thickness. Needed to manage contact.

- Fix.
- Alignment/ no alignment, check the box.
- Insert the mask holder to its place upside-down. Lock it from aside. Chrome face must look at you (upper face).
- Place the sample to tray, turn on the sample vacuum on the computer software and push the tray in.
- Expose.
- Turn the mask vacuum off, take the mask.
- Turn the sample vacuum off, take the sample.
- Turn the lamb off (on the controller), wait for it to cool.
- Development. (AG 3276 developer for AZ5214 photoresist)
- Put the sample in the developer bath.
- Depending on photoresist, bath it for like 30 seconds (25sec is optimum).
- After developer, wash it with water immediately and dry with N-gun.
- Now the pattern on the mask must have been on the wafer.
- Check it with optic microscope
- Turn off the computer
- Turn off the midas mask aligner
- Turn off the spinner and hot plate.

APPENDIX C: SURFACE PROFILER

In our lab, we have KLA Tencor AlphaStep d-100 Stylus Profiler. Its specifications are 30 mm scan lengt, 1.2 microns z sensor range and force control from 0.03mg to 10mg. As explained before the stylus profiler is placed on Thor Labs desktop vibration isolation table. Operating procedure of the stylus profiler is given as following.

- Turn on the computer and profiler.
- Start the software Alpha-step D-100
- The software asks to home all motor. Say Yes. This will initialize the optics and motors.
- In the main screen, there is video capture window which shows what the optics see.
- On the right side, there is control panel which you can control illumination, contrast, brightness, zoom and z stage movement control.
- At the bottom of the screen, there are scan parameters.
- Length. The length that the stylus scans. Maximum scan length is 30 mm.
- Speed. The scan speed. The recommended speed is around 0.10 mm/sec.
- Range. This controls the scan length on z axis. The bigger the range, the less resolution.
- Direction. you can scan forward or backward
- Stylus Force. Choose depending on the hardness of the sample. Start with a low force value and gradually increase it until you obtain a good scan data.
- Data point filter. This tells you how many data points you obtain. The slower scan, the more the data points. More data points is better but then you have more noise in the scan. 10k-20k data points are optimum.
- Load the sample.
- Move the head to the upmost point and place the sample on the stage.
- Since the stage does not have vacuum system, drop a few drops of isopropanol on the stage, place the sample on it and twist it a little bit. This will act like a weak vacuum to keep the sample on the stage stable.

- You can move the stage over along x and y directions by the red knobs, rotate the stage manually by hand and you can adjust the tilt of the stage with the bigger black knob.
- Do never move the stage when the stylus is engaged.
- Then press the ENGAGE button. The system automatically engages the stylus onto the sample surface. While attempting to engage the sign is red and when it is engaged it becomes green. Otherwise it is gray.
- After loading the sample and setting the scan parameters, press the SCAN button on the top of the video capture window. The scan is over –Y direction (from back to the front of the device).
- Do not touch the table to prevent vibrations.
- You can see a real time trace of the stylus at the bottom of the screen. At the end of the scan, you will see a graph which shows the 2D topography of the scanned line.
- At this window, there are two cursors. R for reference and M for measurement. You can use these cursors to level the trace and get rid of the tilt. You can also use M cursor to read the step height on the data control panel(Delta Height).
- You can save the scan data either as .xml (excel file) or .dat format by selecting save data file as... in the save menu. When desired a screenshot, showing all the scan parameters, can be taken by pushing Ctrl + Alt + PrntScrn buttons simultaneously. Then you can paste this screenshot in Windows-Paint program and save it as .jpg or .bmp file.
- After you finish your measurements, do not forget to disengage the stylus from surface and raise it as much as possible by clicking UP button in z-stage menu on the right. Then extract your sample, but pay attention not to touch the stylus during extracting. When you are done close the Alpha-step D-100 software and turn the computer and profiler off.

APPENDIX D: ATOMIC FORCE MICROSCOPY

Operation procedure for Bruker Dimension Edge Atomic Force Microscope is as follows.

- When working on AFM, the user should bring bottle of IPA-DI water, gloves, grounding strap, cantilever holder, AFM/MFM tip, tweezer, antistatic Chair and woollen clothes must not be worn.
- Turn on the computer. (Windows : AFM User)
- After The Windows is booted, turn on the AFM controller.
- Open the software Nanodrive. After opening the software, the system initializes. If it notifies any problem, you should stop and fix the problem first.
- At first you have to choose the mod that you are going to use. There are 8 modes in the software. Our system can only work with first 4 modes (upper row). There are three kind of experiments in the software. First one is default edge AFM for any scan in the air. Second is liquid option for scanning in liquid. Third is small Scan Mode for scanning in a small area (5microns) with high resolution and low noise.
- Maximum scan area in our system is 100×100 microns.
- Choose the mode and click load experiment.
- Now you have to place the cantilever on the holder. Which holder and cantilever you have to use depend on the scan mode.
- Be careful while holding the cantilever with tweezers. It is better to place the cantilever right next to an edge for better stability.
- If you are going to take magnetic image, you have magnetize the tip at this point with the magnet which is supplied with the system.
- Mount the cantilever holder to the head. Be careful while holding the head since it is delicate.
- Laser Alignment. Due to the bug in the computer software, go to configuration panel of the camera, turn the camera off and on again to start it.
- The software segment. Tip segment focuses the camera on the cantilever and

surface segment focuses the camera on the surface.

- Match the crosshair on the screen to the tip of the cantilever.
- Now you have to align the laser spot right on the tip of the cantilever by using the white paper method. Dismount the head, clamp it and mount the head back. So the head is up above the stage. Put a white paper under the head. By using the upper knobs, try to align the laser spot. Laser spot size is like 15-20 microns. One of the cantilever arm is about 30-40 microns.
- The light reflected from the back of the cantilever falls on the photo detector. You have to align the laser spot on the detector right in the middle point of it. The vertical and horizontal sums must be close to zero as much as possible whereas the total voltage must be as high as possible. Detector alignment is done by knobs on the upper-left corner of the head.
- Now we have to load the sample. Shift to surface focus on the computer software. Move the sample stage outside, put the sample on the stage and open the vacuum with the switch at the right side of the head.
- Close the cover of the system. Be careful that you have to check if the cover is closed properly. By looking through the window, try to see if any light leaks inside, this means the cover is not closed properly.
- For Tapping Mode, at this stage, you have to tune the cantilever. For this, you have to run the procedure in the software to find the resonant frequency of your cantilever and choose the most appropriate point (frequency) on the graph.
- Engagement. For the camera to focus on the tip or on the surface, the distance between them is set to 1 mm default by the software. So that you have to move the manually in z direction until the distance between them is 1 mm. You can check this by looking at the tip focus and surface focus windows. Both of them must be in focus when the distance is 1mm. After that, the head moves automatically in z direction to engage the tip to the sample surface. If you choose fast option, the tip moves the first 700microns at once and the rest 300microns step by step. If you choose fine option, you can adjust the step size. The tip moves down until the set point is reached. The set point has to be determined by the user beforehand.
- Now, the tip must be brought to the bottom left point of a square region where you want to scan.

- After engagement, you can check whether the tip is close enough to the sample surface or not by point spectroscopy (under real time control menu). If it is not ok, you better try changing the set point.
- While engaging, to halt the process, press the engage the tip button again.
- After engaging, scanning window is automatically opened. In this window, scan parameters such as resolution, scan rate, scan range must be adjusted. If necessary, offset in X and Y direction can be given to move to tip to the desired position. Before starting the scan, the channels (Height, phase, amplitude etc.)must be chosen. If a magnetic image is going to be taken, then the lift mode must be selected.
- When the parameters are set and the tip is engaged in the desired position, surface scan can be started by clicking the start button.
- PID options which affects the quality of a signal can be adjusted during scan. P can be defined as reaction against a feature. If the signal oscillates too much after a feature (like a step), then I value must be increased. D, which stands for derivative should better be kept constant at 0.
- After the scanning is finished, data and images are not saved automatically. They must be saved by the user.
- If the experiment is done, the tip must be disengaged and moved away from the surface far enough. Then the cantilever holder must be demounted, the sample must be moved. The user must be so careful during these manual operations.
- Finally, the software, computer and the electronics can be turned off.

APPENDIX E: ION MILLING ETCH RATE CALIBRATION

In order to learn ion-milling etch rate of XPS machine on silicon nitride thin film, we performed the following experiment.

- Take a photoresist coated Si wafer, patterned for deposition calibration.
- Deposit silicon nitride on that wafer by sputtering. At this point, you should know how thick you deposit silicon nitride.
- After that, bring this sample to XPS and etch different points for different periods.This will etch both PR and silicon nitride.
- Then apply lift-off procedure (3mins of acetone and 3mins of isopropanol in ultrasonic bath). This will remove the Photoresist coated parts and you are left with silicon nitride steps on the wafer
- Finally, measure the thickness of those steps so that you can learn how much you etch.

For silicon nitride with 1000V ion gun energy and 1mm raster size, the results are listed as:

- Etch time : 20sn , low current = 51 nm – 44nm = 7nm Etch Rate : 0.35nm/sn
- Etch time : 40sn , low current = 51 nm – 36.8nm = 14.2nm Etch Rate : 0.35nm/sn
- Etch time : 40sn , high current = 54 nm – 22.6nm = 31.4nm Etch Rate : 0.78nm/sn
- Etch time : 60sn , low current = 52 nm – 32nm = 20nm Etch Rate : 0.33nm/sn
- Etch time : 90sn , low current = 52 nm – 22nm = 30nm Etch Rate : 0.33nm/sn

It can be concluded that average ion-milling rate on silicon nitride is 0.34 nm per second at low current, 1000V ion gun energy and 1 mm raster size.

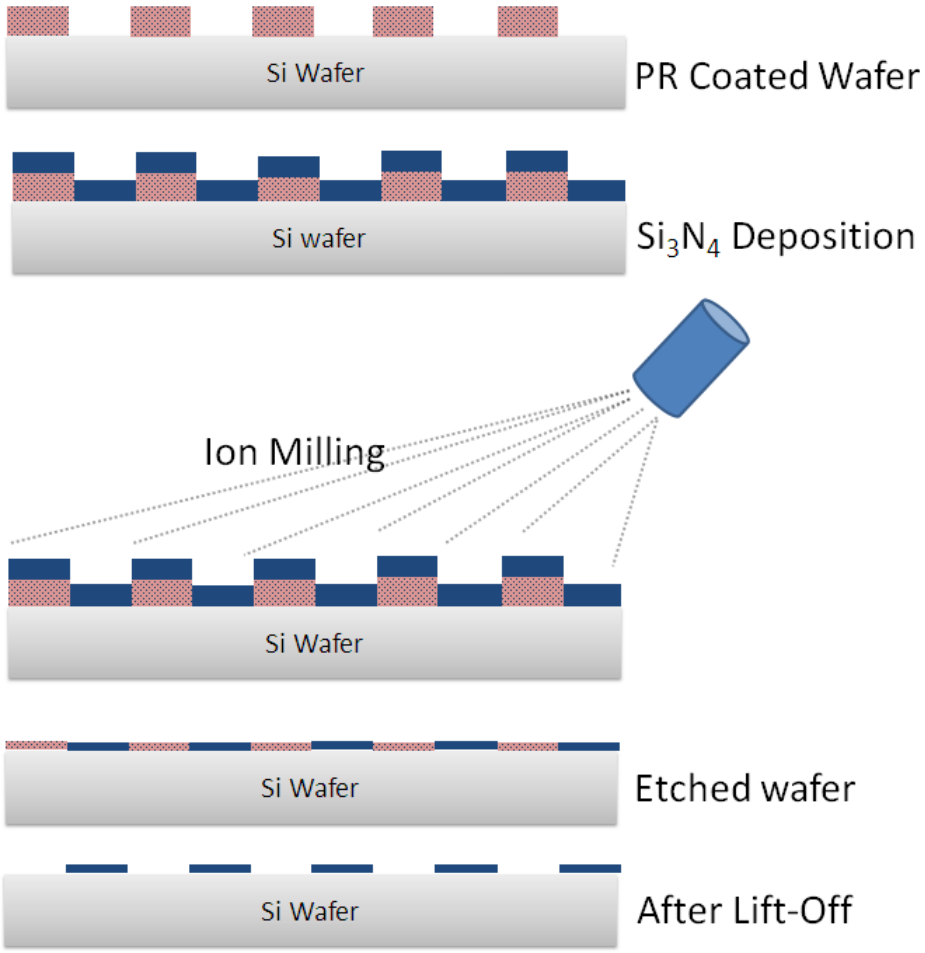


Figure E.1. Ion milling etch rate calibration steps.

REFERENCES

1. Ozatay, O., P. Mather, J. Thiele, T. Hauet and P. Braganca, "Spin-Based Data Storage", D. L. Andrews, G. D. Scholes and G. P. Wiederrecht (Editors), *Comprehensive Nanoscience and Technology*, pp. 561 – 614, Academic Press, Amsterdam, 2011.

2. Piramanayagam, S., "Perpendicular recording media for hard disk drives", *Journal of Applied Physics*, Vol. 102, No. 1, p. 011301, 2007.

3. Zhu, J. G. J. and C. Park, "Magnetic tunnel junctions", *Materials Today*, Vol. 9, No. 11, pp. 36 – 45, 2006.

4. Julliere, M., "Tunneling between ferromagnetic films", *Physics Letters A*, Vol. 54, No. 3, pp. 225 – 226, 1975.

5. Sbiaa, R. and S. N. Piramanayagam, "Patterned media towards nano-bit magnetic recording: Fabrication and challenges", *Recent patents on nanotechnology*, Vol. 1, No. 1, pp. 29 – 40, 2007.

6. Soeno, Y., M. Moriya, K. Ito, K. Hattori, A. Kaizu, T. Aoyama, M. Matsuzaki and H. Sakai, "Feasibility of discrete track perpendicular media for high track density recording", *IEEE Transactions on Magnetics*, Vol. 39, No. 4, pp. 1967–1971, July 2003.

7. Kikitsu, A., "Prospects for bit patterned media for high-density magnetic recording", *Journal of Magnetism and Magnetic Materials*, Vol. 321, No. 6, pp. 526 – 530, 2009.

8. Terris, B. D. and T. Thomson, "Nanofabricated and self-assembled magnetic structures as data storage media", *Journal of Physics D: Applied Physics*, Vol. 38, No. 12, p. R199, 2005.

9. Alex, M., A. Tselikov, T. McDaniel, N. Deeman, T. Valet and D. Chen, "Characteristics of thermally assisted magnetic recording", *IEEE Transactions on Magnetics*, Vol. 37, No. 4, pp. 1244–1249, Jul 2001.

10. Parkin, S., "Unidirectional racetrack memory device", *US Patent 7,551,469*, Jun. 23 2009.

11. Parkin, S. S. P., M. Hayashi and L. Thomas, "Magnetic Domain-Wall Racetrack Memory", *Science*, Vol. 320, No. 5873, pp. 190–194, 2008.

12. Berger, L., "Exchange interaction between ferromagnetic domain wall and electric current in very thin metallic films", *Journal of Applied Physics*, Vol. 55, No. 6, 1984.

13. Ozatay, O. and B. Terris, "Read/write structures for a three dimensional memory", *US Patent 8,164,940*, Apr. 24 2012.

14. Kalyoncu, Y. B. and O. Ozatay, "Bir Üç Boyutlu Opto-Manyetik Veri Depolama Sistemi ve Yöntemi", *TPE Application Number 2012/12865*, 2012.

15. Kalyoncu, Y. B. and O. Ozatay, "Bir Üç Boyutlu Opto-Manyetik Veri Depolama Sistemi ve Yöntemi", *TPE Application Number 2012/15356*, 2012.

16. Kalyoncu, Y. B. and O. Ozatay, "A Three Dimensonal Opto-Magnetic Data Storage System and Method", *PCT Application Number PCT/IB2013/061337*, 2013.

17. Popova, D., A. Bringer and S. Blügel, "Theoretical investigation of the inverse Faraday effect via a stimulated Raman scattering process", *Physical Review B*, Vol. 85, p. 094419, Mar 2012.

18. Stanciu, C. D., F. Hansteen, A. V. Kimel, A. Kirilyuk, A. Tsukamoto, A. Itoh and T. Rasing, "All-Optical Magnetic Recording with Circularly Polarized Light", *Physical Review Letters*, Vol. 99, p. 047601, Jul 2007.

19. Hansen, P., C. Clausen, G. Much, M. Rosenkranz and K. Witter, "Magnetic and magneto optical properties of rare earth transition metal alloys containing Gd, Tb, Fe, Co", *Journal of Applied Physics*, Vol. 66, No. 2, 1989.

20. Siegman, A., *Lasers*, University Science Books, Palo Alto, 1986.

21. Holub, M. and P. Bhattacharya, "Spin-polarized light-emitting diodes and lasers", *Journal of Physics D: Applied Physics*, Vol. 40, No. 11, p. R179, 2007.

22. Hasnain, G., K. Tai, L. Yang, Y. H. Wang, R. J. Fischer, J. Wynn, B. Weir, N. Dutta and A. Y. Cho, "Performance of gain-guided surface emitting lasers with semiconductor distributed Bragg reflectors", *IEEE Journal of Quantum Electronics*, Vol. 27, No. 6, pp. 1377–1385, Jun 1991.

23. Kish, F. and R. Schneider, "Fabrication of transparent substrate vertical cavity surface emitting lasers by semiconductor wafer bonding", *US Patent 5,837,561*, Nov. 17 1998.

24. Ohno, Y., D. Young, B. Beschoten, F. Matsukura, H. Ohno and D. Awschalom, "Electrical spin injection in a ferromagnetic semiconductor heterostructure", *Nature*, Vol. 402, No. 6763, pp. 790–792, 1999.

25. Hayashi, M., L. Thomas, C. Rettner, R. Moriya, Y. B. Bazaliy and S. S. P. Parkin, "Current Driven Domain Wall Velocities Exceeding the Spin Angular Momentum Transfer Rate in Permalloy Nanowires", *Physical Review Letters*, Vol. 98, p. 037204, Jan 2007.

26. Cao, G., *Nanostructures & Nanomaterials: Synthesis, Properties & Applications*, Imperial College Press, London, 2004.

27. Nishi, Y. and R. Doering, *Handbook of Semiconductor Manufacturing Technology, Second Edition*, Taylor & Francis, New York, 2012.

28. Zhao, Y., G. Wang, T. Lu, M. De Graef and T. Lucatorto, *Characterization of*

Amorphous and Crystalline Rough Surface – Principles and Applications, Experimental Methods in the Physical Sciences, Elsevier Science, San Diego, 2000.

29. Whitehouse, D., *Handbook of Surface and Nanometrology, Second Edition*, Taylor & Francis, London, 2012.

30. Foner, S., "Versatile and Sensitive VibratingSample Magnetometer", *Review of Scientific Instruments*, Vol. 30, No. 7, 1959.

31. Cullity, B. and C. Graham, *Introduction to Magnetic Materials*, Wiley, New Jersey, 2009.

32. Smits, F. M., "Measurement of Sheet Resistivities with the Four-Point Probe", *Bell System Technical Journal*, Vol. 37, No. 3, pp. 711–718, 1958.

33. Franz, R. and G. Wiedemann, "Ueber die Wärme-Leitungsfähigkeit der Metalle", *Annalen der Physik*, Vol. 165, No. 8, pp. 497–531, 1853.

34. Ashcroft, N. and N. Mermin, *Solid state physics*, Science: Physics, Brooks/Cole, Belmont, 1976.

35. Goldstein, J., *Scanning Electron Microscopy and X-ray Microanalysis: Third Edition*, Springer US, New York, 2003.

36. Schroder, D., *Semiconductor Material and Device Characterization*, Wiley, New Jersey, 2006.

37. Jenkins, R., R. Manne, R. Robin and C. Sénémaud, "Nomenclature, Symbols, Units and Their Usage in Spectrochemical Analysis VIII Nomenclature System for X-Ray Spectroscopy", *Powder Diffraction*, Vol. 6, pp. 95–101, 6 1991.

38. Moseley, H., "The High Frequency Spectra of the Elements", *Philpsophical Magazine*, p. 1024, 1913.

39. Haug, E. and W. Nakel, *The Elementary Process of Bremsstrahlung*, World Scientific lecture notes in physics, World Scientific, Singapore, 2004.

40. Auger, P., "On the Compound Photoelectric Effect", *Journal de Physique et Radium*, Vol. 6, pp. 205–208, 6 1925.

41. Fadley, C., "X-ray photoelectron spectroscopy: Progress and perspectives", *Journal of Electron Spectroscopy and Related Phenomena*, Vol. 178–179, No. 0, pp. 2 – 32, 2010, trends in X-ray Photoelectron Spectroscopy of solids (theory, techniques and applications).

42. Williams, K. and R. Muller, "Etch rates for micromachining processing", *Journal of Microelectromechanical Systems*, Vol. 5, No. 4, pp. 256–269, Dec 1996.

43. Naumkin, A., A. Kraut-Vass, S. Gaarenstrom and C. Powell, "NIST XPS Photoelectron Spectroscopy Database", , Oct 2012, `http://srdata.nist.gov/xps/`.

44. Repoux, M., "Comparison of background removal methods for XPS", *Surface and Interface Analysis*, Vol. 18, No. 7, pp. 567–570, 1992.

45. Eaton, P. and P. West, *Atomic Force Microscopy*, OUP Oxford, New York, 2010.

46. Martin, Y., C. C. Williams and H. K. Wickramasinghe, "Atomic force microscope–force mapping and profiling on a sub 100Å scale", *Journal of Applied Physics*, Vol. 61, No. 10, 1987.

47. Hartmann, U., "Magnetic Force Microscopy", *Annual Review of Materials Science*, Vol. 29, No. 1, pp. 53–87, 1999.

48. Moritz, J., F. Garcia, J. C. Toussaint, B. Dieny and J. P. Nozières, "Orange peel coupling in multilayers with perpendicular magnetic anisotropy: Application to (Co/Pt)-based exchange-biased spin-valves", *EPL (Europhysics Letters)*, Vol. 65, No. 1, p. 123, 2004.

49. Yamaguchi, A., T. Ono, S. Nasu, K. Miyake, K. Mibu and T. Shinjo, "Real-Space Observation of Current-Driven Domain Wall Motion in Submicron Magnetic Wires", *Physical Review Letters*, Vol. 92, p. 077205, Feb 2004.

50. Mangin, S., M. Gottwald, C. H. Lambert, D. Steil, V. Uhlíř, L. Pang, M. Hehn, S. Alebrand, i. M. Cinchett and G. Malinowski, "Engineered materials for all-optical helicity-dependent magnetic switching", *Nature Materials*, , No. 3, p. 286–292, 2014.

51. Holub, M., J. Shin, D. Saha and P. Bhattacharya, "Electrical Spin Injection and Threshold Reduction in a Semiconductor Laser", *Physical Review Letters*, Vol. 98, p. 146603, Apr 2007.

52. Dietl, T., H. Ohno and F. Matsukura, "Hole-mediated ferromagnetism in tetrahedrally coordinated semiconductors", *Physical Review B*, Vol. 63, p. 195205, Apr 2001.

53. de Groot, R. A., F. M. Mueller, P. G. v. Engen and K. H. J. Buschow, "New Class of Materials: Half-Metallic Ferromagnets", *Physical Review Letters*, Vol. 50, pp. 2024–2027, Jun 1983.